

A Fully Coupled Discontinuous Galerkin Method for Low-Mach Diffusion Flames

Zur Erlangung des akademischen Grades Doktor-Ingenieur (Dr.-Ing.)
Vorgelegte Dissertation von Juan Francisco Gutiérrez Jorquera aus Ñuñoa, Santiago de Chile
Tag der Einreichung: 15. August 2023, Tag der Prüfung: 24. Oktober 2023

1. Gutachten: Prof. Dr.-Ing Martin Oberlack
2. Gutachten: Prof. Dr. rer. nat. Michael Schäfer
Darmstadt



TECHNISCHE
UNIVERSITÄT
DARMSTADT

Fachbereich Maschinenbau
Fachgebiet für
Strömungsdynamik

A Fully Coupled Discontinuous Galerkin Method for Low-Mach Diffusion Flames

Vorgelegte Dissertation von Juan Francisco Gutiérrez Jorquera

Tag der Einreichung: 15. August 2023

Tag der Prüfung: 24. Oktober 2023

Darmstadt

Bitte zitieren Sie dieses Dokument als:

URN: urn:nbn:de:tuda-tuprints-1234

URL: <http://tuprints.ulb.tu-darmstadt.de/12345>

DOI: <https://doi.org/10.25534/tuprints-1234>

Dieses Dokument wird bereitgestellt von tuprints,

E-Publishing-Service der TU Darmstadt

<http://tuprints.ulb.tu-darmstadt.de>

tuprints@ulb.tu-darmstadt.de

Die Veröffentlichung steht unter folgender Creative Commons Lizenz:

Namensnennung 4.0 International

<https://creativecommons.org/licenses/by/4.0/>

This work is licensed under a Creative Commons License:

Attribution 4.0 International

<https://creativecommons.org/licenses/by/4.0/>

Erklärungen laut Promotionsordnung

§ 8 Abs. 1 lit. c PromO

Ich versichere hiermit, dass die elektronische Version meiner Dissertation mit der schriftlichen Version übereinstimmt.

§ 8 Abs. 1 lit. d PromO

Ich versichere hiermit, dass zu einem vorherigen Zeitpunkt noch keine Promotion versucht wurde. In diesem Fall sind nähere Angaben über Zeitpunkt, Hochschule, Dissertationsthema und Ergebnis dieses Versuchs mitzuteilen.

§ 9 Abs. 1 PromO

Ich versichere hiermit, dass die vorliegende Dissertation selbstständig und nur unter Verwendung der angegebenen Quellen verfasst wurde.

§ 9 Abs. 2 PromO

Die Arbeit hat bisher noch nicht zu Prüfungszwecken gedient.

Darmstadt, 15. August 2023

J. Gutiérrez-Jorquera

Abstract

In this work, a high-order fully coupled numerical solver based on the Discontinuous Galerkin (DG) method for simulating reactive flows is presented. The discretized set of equations of continuity, momentum, energy and chemical species are solved in a fully coupled manner using a globalized Newton algorithm. The main objective of the solver is to create a framework for investigating diffusion flames using the DG method. For this, the low-Mach approximation of the Navier–Stokes equations is used, which enables the simulation of non-Boussinesq flows. The chemical reaction is modeled using a one-step combustion model with variable kinetic parameters, which is specifically tailored for hydrocarbon combustion. The temperature and concentration dependence of the density, heat capacity, and transport parameters is considered in the formulation.

A detailed description of the governing equations utilized in this study is presented, along with a comprehensive discussion of their derivation and the assumptions involved. The general procedure involved in the temporal and spatial discretization of the DG method is illustrated using a basic transport equation. Subsequently, the DG discretization of the governing equations for reacting flows is presented, and numerical fluxes are thoroughly described.

The computational methods developed for solving the governing equations are presented in detail. In particular, the strategy for the solution of the nonlinear problem by means of the globalized Dogleg-Newton method is explained, together with an efficient method for calculating the Jacobian matrix. Furthermore, various strategies that improve the convergence properties of the algorithm are presented. These include a fully automatized homotopy continuation method for the solution of highly nonlinear systems, an Adaptive Mesh Refinement strategy used for generating adequate meshes on critical areas of the simulation, and a solver safeguard for avoiding unphysical solutions during the calculation.

For steady reacting flows an additional strategy is applied, which allows to find adequate initial estimates for the simulation of diffusion flames. This approach involves solving a simplified set of equations obtained under the assumption of an infinitely fast chemical reaction and is a robust method for finding the solution of combustion systems.

A thorough validation of the solver using several test cases is shown, which also highlight important advantages of the DG method and the algorithms introduced in this work. The test cases validate the solver against various benchmark solutions obtaining results in very good agreement with the literature. Additionally, the accuracy of the method is assessed in various flow settings, all of them demonstrating the expected high convergence rates of the DG method. However, stability problems are observed in transient simulations of low-Mach flows in which density exhibits large variations.

Zusammenfassung

In dieser Arbeit wird ein vollständig gekoppelter numerischer Löser hoher Ordnung vorgestellt, der auf der Discontinuous Galerkin (DG)-Methode zur Simulation von reaktiven Strömungen basiert. Die diskretisierten Gleichungen der Kontinuität, des Impulses, der Energie und der chemischen Spezies werden auf vollständig gekoppelte Weise unter Verwendung eines globalisierten Newton-Algorithmus gelöst. Das Hauptziel des Lösers ist die Erstellung eines Frameworks für die Untersuchung von Diffusionsflammen mit der DG-Methode. Dazu wird die low-Mach-Approximation der Navier-Stokes-Gleichungen verwendet. Die chemische Reaktion wird mit einem einstufigen Verbrennungsmodell mit variablen kinetischen Parametern modelliert, das speziell auf die Verbrennung von Kohlenwasserstoffen zugeschnitten ist. Die Temperatur- und Konzentrationsabhängigkeit der Dichte-, Wärmekapazitäts- und Transportparameter wird bei der Formulierung berücksichtigt.

Eine detaillierte Darstellung der in dieser Studie verwendeten Gleichungen wird zusammen mit einer umfassenden Diskussion ihrer Herleitung und der damit verbundenen Annahmen präsentiert. Das allgemeine Verfahren für die zeitliche und räumliche Diskretisierung mit der DG-Methode wird anhand einer allgemeinen Transportgleichung erläutert. Anschließend wird die DG-Diskretisierung der Gleichungen für reaktive Strömungen vorgestellt, und die verwendeten numerischen Flüsse werden beschrieben.

Die entwickelten Berechnungsmethoden zur Lösung der herrschenden Gleichungen werden im Detail vorgestellt. Insbesondere wird die Strategie zur Lösung des nichtlinearen Problems mit Hilfe der globalisierten Dogleg-Newton-Methode erläutert, zusammen mit einer effizienten Methode zur Berechnung der Jacobimatrix. Darüber hinaus werden verschiedene Strategien vorgestellt, die die Konvergenzeigenschaften des Algorithmus verbessern. Dazu gehören eine vollautomatisierte Homotopie-Fortsetzungsmethode für die Lösung von stark nichtlinearen Systemen, eine adaptive Netzverfeinerungsstrategie, die für adäquate Netze in kritischen Bereichen der Simulation verwendet wird, und eine Solver-Safeguard zur Vermeidung von unphysikalischen Lösungen während der Berechnung.

Für stationär reaktive Strömungen wird eine zusätzliche Strategie verwendet, die es ermöglicht, geeignete Anfangsschätzungen zu finden, die für die Simulation einer Diffusionsflamme verwendet werden können. Dieser Ansatz erfordert die Lösung eines vereinfachten Satzes von Gleichungen, die unter der Annahme einer unendlich schnellen chemischen Reaktion aufgestellt werden, und ist eine robuste Methode zur Lösung von Verbrennungssystemen.

Eine gründliche Validierung des Lösers anhand mehrerer Testfälle wird gezeigt, wodurch auch zentrale Vorteile der DG-Methode und der in dieser Arbeit vorgestellten Algorithmen hervorgehoben werden können. Die Testfälle ermöglichen es, den Löser gegen verschiedene Benchmark-Lösungen zu validieren, wobei Ergebnisse in sehr guter Übereinstimmung mit der Literatur erhalten werden. Darüber hinaus wird die Genauigkeit der Methode in verschiedenen Strömungssituationen bewertet, wobei für alle die erwarteten hohen Konvergenzraten der DG-Methode erzielt werden. Stabilitätsprobleme werden jedoch bei instationären Simulationen von low-Mach-Strömungen beobachtet, bei denen die Dichte große Schwankungen aufweist.

Acknowledgements

First of all, I would like to thank my supervisor Prof. Oberlack for his support and giving me the opportunity of writing this thesis at the Department of Fluid Dynamics. I would also like to express my gratitude to Florian Kummer, without whom the development of this work would not have been possible.

Furthermore, I would like to thank all colleagues whom I had the privilege of sharing with over the four years I was in the Fluid Mechanics Department, sharing not only knowledge and scientific discussions, but also activities outside the office, nice coffee breaks, and visits to the Biergarten. In particular, I would like to thank (in alphabetical order) my colleagues Lauritz Beck, Anne Kikker, Dario Klingenberg, Matthias Rieckmann, Markus Geisenhofer and Jens Weber for their support in developing this thesis, along with the extensive and fruitful discussions we engaged in over the years.

I would like to extend my gratitude to my dear friends Anastasia, Andres, Francisco, Graziella, Javiera, Juan, Victor and the *Diuquers* for their unconditional help during all these years. I truly believe that their support and company during difficult and joyful times was indispensable for the creation of this work.

Last but not least, I want to express my gratitude to my sisters Catalina and Constanza, and to my parents, Juan Carlos and Margarita, since without them there would be no way for me to be where I am now. Their love and support in every way is something for which I will be eternally grateful.

Contents

List of Figures	xiii
List of Tables	xvii
List of Abbreviations	xix
List of Symbols	xxi
1 Introduction	1
1.1 The DG method for reacting flows	1
1.2 Objectives and motivation	5
1.3 Outline of the thesis	6
1.4 The BoSSS code	7
2 Governing equations	9
2.1 The low-Mach number equations for reactive flows	9
2.1.1 The reactive Navier–Stokes equations	9
2.1.2 The reactive low-Mach Navier-Stokes equations	14
2.1.3 A note on the multiple solutions of the system	17
2.2 The flame sheet approximation	18
2.3 Boundary conditions	21
3 The Discontinuous Galerkin method	23
3.1 The Discontinuous Galerkin method	23
3.1.1 Definitions for the discretization	23
3.1.2 Discretization using the DG Method	24
3.1.3 Temporal discretization	28
3.2 Discontinuous Galerkin discretization of the low-Mach equations	31
3.2.1 Discontinuous Galerkin discretization of the finite reaction rate problem	31
3.2.2 Discontinuous Galerkin discretization of the flame sheet problem	32
3.2.3 Definitions of nonlinear forms	33
4 Computational methodology	37
4.1 State of the art of DG methods for diffusion flame simulations	37
4.2 The XNSEC solver	38
4.3 Solution of the nonlinear problem	39
4.3.1 Newton’s method	40
4.3.2 Calculation of the Jacobian matrix	40
4.3.3 Newton-Dogleg Method	42
4.3.4 Linear solver	44
4.3.5 Termination criterion	44

4.4	Additional convergence supporting strategies	45
4.4.1	Homotopy method	45
4.4.2	Solver safeguard	47
4.4.3	Flame sheet estimates for steady state combustion simulations	47
4.4.4	Adaptive Mesh Refinement	49
5	Numerical results	53
5.1	Single-component isothermal cases	53
5.1.1	Lid-driven cavity flow	53
5.1.2	Backward-facing step	55
5.2	Single-component non-isothermal cases	58
5.2.1	Heated backward-facing step	58
5.2.2	Couette flow with vertical temperature gradient	60
5.2.3	Differentially heated cavity problem	64
5.2.4	Flow over a circular cylinder	73
5.2.5	Rayleigh-Bénard Convection	76
5.3	Multi-component non-isothermal cases	83
5.3.1	Coflow laminar diffusion flame	83
5.3.2	Counterflow diffusion flame	89
5.3.3	Chambered diffusion flame	100
5.3.4	Combustion over a square cylinder	101
5.4	Conclusion	106
6	Conclusion	109
6.1	Future work	110
Bibliography		111

List of Figures

1.1	Runtime comparison of the DG-SIMPLE solver and the XNSEC solver for a typical non-isothermal simulation.	5
1.2	Schematic representation of the structure of the BoSSS solver.	7
2.1	S-shaped bifurcation curve of a combustion process.	17
2.2	Temperature and fuel mass fraction profiles calculated in the center-line of a counter-flow flame configuration using finite chemistry and the flame sheet approximation.	20
3.1	Schematic illustration of two cells. Normals of the cell K_1 are shown.	23
3.2	A-stability regions of the BDF schemes for different order s . The areas shown in grey are unstable regions.	31
4.1	Residual, trust region diameter and homotopy parameter history of the differentially heated cavity test case using the Homotopy strategy.	46
4.2	Smoothing function at $z_{st} = 0.22$ for different smoothing parameters σ	48
4.3	Temperature profile calculated in the center-line of a counter-flow flame configuration for different smoothing parameters σ	50
4.4	Adaptive mesh refinement around the stoichiometric surface in a coflow flame configuration. The iso-contour $z = z_{st}$ of the mixture fraction is shown in red.	51
5.1	Schematic representation of the Lid-Driven cavity flow.	54
5.2	Mesh and streamlines of the lid-driven cavity flow with $Re = 1000$	54
5.3	Calculated velocities along the centerlines of the cavity and reference values. Left plot shows the x-velocity for $x = 0.5$. Right plot shows the y-velocity for $y = 0.5$	55
5.4	Schematic representation of the backward-facing step.	56
5.5	Mesh used for the backward-facing step configuration.	57
5.6	Distribution of x-component of velocity in the backward-facing step configuration for a Reynolds number of 400.	57
5.7	Detachment and reattachment lengths of the primary and secondary recirculation zones after the backward-facing step compared to the reference solution .	58
5.8	Temperature profile and streamlines corresponding to the backward-facing Step configuration for $Re = 400$ and an expansion ratio of two.	59
5.9	Local friction factor and local Nusselt number along the bottom wall of the backward-facing step for $Re = 700$ and an expansion ratio of two.	60
5.10	Schematic representation of the Couette flow with temperature difference test case.	61
5.11	Solution of the Couette flow with vertical temperature gradient using a Power-Law. .	62
5.12	Convergence study of the Couette-flow with temperature difference. A power-law is used for the transport parameters.	63

5.13 Runtime comparison of the DG-SIMPLE solver and the XNSEC solver for the Couette flow with vertical temperature gradient for different polynomial degrees k and number of cells.	64
5.14 Schematic representation of the differentially heated cavity problem.	65
5.15 Streamlines of the heated cavity configuration with $\epsilon = 0.6$ for different Reynold numbers.	67
5.16 Temperature profiles for the differentially heated square cavity along different vertical levels.	67
5.17 Profiles of the x-velocity component for the differentially heated square cavity along the vertical line $x = 0.5$	68
5.18 Profiles of the y-velocity component for the differentially heated square cavity along the horizontal line $y = 0.5$	69
5.19 Convergence study of the differentially heated cavity problem for $\text{Ra} = 10^3$	71
5.20 Nusselt numbers of the differentially heated square cavity at the hot wall (Nu_h) and the cold wall (Nu_c) for different number of cells and polynomial order k	72
5.21 Schematic representation of the heated circular cylinder. Figure adapted from (Miao, 2022)	74
5.22 Temporal evolution of average Nusselt number, lift coefficient and drag coefficient of the heated cylinder	76
5.23 Geometry of the Rayleigh-Bénard convection problem. Convection rolls are sketched.	77
5.24 Maximum x-velocity in the Rayleigh-Bénard convection configuration for different a and r	78
5.25 Stability behavior of the Rayleigh-Bénard convection with $\epsilon = 0.0001$	79
5.26 Temperature field and temperature contours of a Rayleigh-Bénard convection roll	80
5.27 Geometry of the Rayleigh-Bénard convection with pressure outlet boundary conditions.	80
5.28 Temperature and streamlines of the Rayleigh-Bénard flow with pressure outlets.	82
5.29 Geometry of a coflowing flame configuration (not to scale).	84
5.30 Typical convergence history of a diffusion flame in the coflowing flame configuration. Two mesh refinement passes are done. The second pass starts at iteration 21.	85
5.31 Temperature and reaction rate fields of the coflow configuration.	86
5.32 Mass fraction field of H_2O over the line $y = 10$	87
5.33 Nondimensional temperature and reaction rate fields of the coflow configuration considering gravity effects.	88
5.34 Schematic representation (not to scale) of the counterflow diffusion flame configuration.	89
5.35 Nondimensional solution and derived fields of the counterflow flame configuration for case (a).	93
5.35 Nondimensional solution and derived fields of the counterflow flame configuration for case (a) (continued).	94
5.36 Velocity profiles of the counterflow diffusion flame for parabolic and plug inlet boundary conditions.	95
5.37 Comparison of the axial velocity calculated with the XNSEC solver and the one-dimensional approximation.	96

5.38 Comparison of temperature and mass fraction fields obtained with the XNSEC solver and the one-dimensional approximation.	97
5.39 Fuel and oxidizer mass fraction profiles using constant kinetic parameters and variable kinetic parameters	98
5.40 Maximum centerline temperature of a counterflow flame for different strains.	99
5.41 Convergence study of the maximum value of the temperature for the counterflow diffusion flame configuration.	99
5.42 Schematic representation of the chambered diffusion flame configuration.	100
5.43 Convergence study for the chambered diffusion flame configuration.	101
5.44 Temperature field and mesh of the unsteady combustion over a square cylinder.	102
5.45 Recirculation lengths for different Reynolds numbers for the non-reactive case.	102
5.46 Temperature field and mesh calculated with the Burke-Schumann solution at different times, assuming a constant density.	104
5.47 Temperature field calculated with the Burke-Schumann solution at different times.	105

List of Tables

2.1	Base parameters used in the one-step combustion model by Fernandez-Tarrazo et al. (2006)	13
2.2	Boundary conditions of reactants mass fractions, temperature and mixture fraction.	19
3.1	Coefficients of the BDF schemes.	30
5.1	Extrema of velocity components through the centerlines of the lid-driven cavity for $Re = 1000$. Reference values obtained from Botella and Peyret (1998)	55
5.2	Differentially heated cavity: Results of Nusselt number and Thermodynamic pressure	70
5.3	Thermodynamic pressure and cold-side Nusselt number for different penalty safety factors in a heated cavity with $Ra = 10^3$	73
5.4	Maximum inlet velocity, strain and temperatures used for the counterflow diffusion flame calculations.	91



List of Abbreviations

PARDISO	Parallel Sparse Direct and Multi-Recursive Iterative Linear Solvers
AMR	Adaptive Mesh Refinement
BDF	backward differentiation formula
BoSSS	Bounded Support Spectral Solver
CFD	computational fluid dynamics
DG	Discontinuous Galerkin
DOF	degree of freedom
ENO	Essentially Non-Oscillatory methods
WENO	Weighted Essentially Non-Oscillatory methods
FDM	Finite Difference Method
FEM	Finite Element Method
FVM	Finite Volume Method
MPI	message-passing interface
ODE	ordinary differential equation
PDE	partial differential equation
SIMPLE	Semi-Implicit Method for Pressure Linked Equation
SIP	symmetric interior penalty
TVM	Total Variation diminishing Method
XDG	eXtended Discontinuous Galerkin
XNSEC	eXtended Navier-Stokes Equations solver for Combustion

List of Symbols

B	Pre-exponential factor
\mathcal{B}^1	Boundary condition form of the continuity equation.
\mathcal{B}^2	Boundary condition forms of the momentum equations.
\mathcal{B}^3	Boundary condition form of the temperature equation.
\mathcal{B}^4	Boundary condition forms of the mass fraction equations.
c_p	Specific heat capacity of the mixture
$c_{p,k}$	Specific heat capacity of species k
D	Diffusion coefficient
ρ	Density
D	Diffusion coefficient
ER	Expansion ratio the backward-facing step
\hat{f}	Numerical flux
f	Flux vector
Fr	Froude number
Γ	Edge
g	Gravity vector
h	Channel height of the backward-facing step
\hat{h}	Convective heat transfer coefficient
h	Numerical mesh size
h_k^0	Formation enthalpy of k species.
h_k	Sensible enthalpy of k species.
h_k	Specific enthalpy of k species.
\Im	Interface
\mathbf{j}_k	Molecular mass flux vector of species k .
k	Total degree of the polynomial space
K	Numerical cell
\mathfrak{K}_h	Numerical mesh
λ	Heat conductivity

M	Mass matrix
μ	Dynamic viscosity
N_k	Number of local DOF
N	Number of total DOF
N	Total number of species in the mixture
\mathbf{n}_Γ	Edge normal field
\mathbf{n}_γ	Interface normal vector
\mathbf{n}	Normal vector
Nu	Nusselt number
ν_k	Stoichiometric coefficient of species k
ν	Kinematic viscosity
ν	Stoichiometric coefficient
Nu_{loc}	Nusselt number, local
Ω	Domain of interest, computational domain
ω_T	Net heat release from chemical reaction
ω_k	Net rate of production of species k
Op	Operator matrix
\mathbb{P}_k	Broken polynomial space
ϕ	Basis function
Pr	Prandtl number
p	Pressure
q	Local heat flux.
Q_j	Rate of progress of reaction j
R	Universal gas constant
R	Residual from DG approximation
r	Error of the DG discretization
Re	Reynolds number
S	Step height of the backward-facing step
S	Sutherland constant.
T	Temperature
T_a	Activation temperature
τ	Viscous tensor
ϑ	General test function
t	Time
u	General variable of the DG method
u	Velocity vector
U	Diffusion velocity vector
W	Mean molecular weight of the mixture

W_k Molecular weight of species k

Y_k Mass fraction of species k

1 Introduction

The simulation of combustion processes poses a significant computational challenge, mainly due to the intricate interaction between chemical reactions and fluid dynamics. The complexity arises from the inherent nature of combustion processes, which often involve multiple simultaneous chemical reactions. These reactions release energy in the form of heat, leading to the formation and propagation of flames. At the same time, fluid dynamics largely drives the transport of heat, mass and momentum, which in turn influences the behavior of the flames. To accurately capture these phenomena, computational models must consider thermodynamic aspects, and properly represent the chemical reactions, species transport and fluid flow involved. These processes are highly nonlinear, rendering their numerical representation difficult.

Of particular interest for many practical applications is the simulation of diffusion flames, which is the result of the combustion of initially separated oxidizer and fuel. The use of numerical methods to simulate diffusion flames can offer crucial insights into flame structures and combustion efficiency. Recently Discontinuous Galerkin (DG) methods have demonstrated high accuracy and efficiency for simulating combustion processes. In this thesis, a fully coupled DG method for simulating diffusion flames will be developed. To explore the method's suitability various simulations will be analysed.

1.1 The DG method for reacting flows

The field of Computational fluid dynamics (CFD) has become a crucial tool for understanding and predicting complex fluid flows. Through the use of numerical methods and specialized algorithms, CFD allows researchers to simulate fluid dynamics problems and gain detailed insights into the behavior of fluids in motion. Detailed information about flow physics that is often difficult or impossible to obtain through experiments can be provided by these methods, leading to deeper insights into the mechanisms governing fluid flow.

In addition to their scientific value, numerical methods for solving the governing equations of fluid dynamics have numerous practical applications. For example, the use of computational tools has become an essential step in the development of new products. They are widely used in fields such as the automotive, chemical and aerospace sectors, to name a few. They are also crucial for assessing the safety and reliability of systems such as chemical and nuclear reactors.

Historically speaking, the methods used in the early days of CFD were low-order numerical methods, such as Finite Volume Method (FVM) or Finite Element Method (FEM). These kind of methods use lower order polynomial functions to approximate the solution of the governing partial differential equations (PDEs). Although they are widely used and very well established, they can suffer from low accuracy or difficulty in representing complex geometries. On the other hand, the so called high order methods use higher order polynomial functions to approximate the solution, allowing them to capture sharp gradients and complex flow structures with greater fidelity. While high-order methods are often more computationally expensive than

low-order methods, they offer advantages when high accuracy is required. The FVM and FEM have also been extended to obtain higher order convergence.

High-order methods have been used since the early days of numerical simulation, but their use was limited due to their comparatively high computational cost. With the advent of modern high-performance computing systems and algorithms, the use of high-order methods has become more widespread and accessible. Today, high-order methods are widely used in many areas of computational fluid dynamics, including aerospace (Mavriplis et al., 2009), automotive (Colombo et al., 2021), and biomedical engineering (Fehn et al., 2019), among others. One of the most prominent methods is the so-called DG method, which is the subject of this thesis.

The DG method

The DG method is a numerical method to solve differential equations. It was initially developed for solving hyperbolic conservation equations, and has recently gained increased attention in the CFD community. The key feature of the method is the use of a piecewise polynomial approximation of the solution field on each element of a computational mesh. This allows for high accuracy and flexibility, with the order of the polynomial being an adjustable parameter. The DG method combines the locality of low-order schemes with the accuracy per degree of freedom (DOF) of spectral schemes. This feature allows for achieving the same level of accuracy as a low-order scheme with fewer DOFs, leading to more efficient and computationally feasible solutions. Another advantage of the DG method is that it is well suited to parallel computing. Within the DG method any given cell of the grid only requires information from its immediate neighbors, allowing an efficient parallelization with minimal communication overhead.

Additionally, in the DG method, the solution is allowed to be discontinuous across element boundaries, enabling the handling of complex geometries and solution discontinuities in a natural way. The conservation of a physical quantity (such as mass, momentum, or energy) is ensured by construction in the DG method. This is achieved through the use of numerical fluxes, which approximate the flux of the conserved quantity at each element boundary. The numerical fluxes must meet certain stability and accuracy criteria to ensure the overall stability and accuracy of the method.

Compared to more popular methods such as the FEM and FVM, the DG method offers several advantages. First, The DG method provides an arbitrary order of error convergence through the local polynomial approximation of the solution field. Specifically, a polynomial approximation of degree p can achieve a numerical discretization error of order $\mathcal{O}(h^{p+1})$ for smooth solutions, where h is a characteristic grid length. This stands in strong contrast with other well established schemes, which are restricted to an accuracy of $\mathcal{O}(h^N)$, with $N \leq 2$ for unstructured grids. Second, the discontinuous approximation of the solution in the DG method allows for a robust treatment of discontinuities in the solution, which can be challenging for the classical FEM. However, the DG method has the disadvantage that usually memory requirements and overall computational costs are higher than in a finite element method.

Diffusion flame modeling and the DG method

Diffusion flames, also known as non-premixed flames, present a significant challenge for simulation due to their complex nature. These flames involve the mixing of two or more reactants before combustion can occur, resulting in a complex interplay of fluid dynamics, heat transfer, and chemical reactions. Moreover, diffusion flames are characterized by steep

gradients in temperature, density, and species concentration, necessitating a high spatial mesh resolution for accurate simulation. In a diffusion flame, the reactants are initially separated, and their mixing is essential for combustion to take place. High-order methods, such as the DG method, offer a solution to alleviate the computational burden associated with the demanding numerical resolution required for accurate simulations.

A proper computational representation of a diffusion flame requires a suitable description of the combustion processes. Representing the involved chemical reactions in an accurate and efficient way poses a significant challenge. Although a detailed description of the chemistry is preferred, it can be computationally intensive and impractical due to the high number of chemical species and chemical reactions taking place. To overcome this issue, simplified kinetic models have been developed, such as the one step kinetic model presented by Fernandez-Tarrazo et al. (2006) for hydrocarbon combustion with air, and is the model used in the present work. This model correlates kinetic parameters with the equivalence ratio, allowing for better representation of the characteristic flame properties of premixed and non-premixed flames. By using a single chemical equation, this model enables the study of complex combustion phenomena while substantially reducing the computational cost. Furthermore, it offers a straightforward and flexible approach to simulate phenomena that would otherwise require a more complex chemical model, such as the calculation of flame temperatures, or the simulation of reactant leakage and near-extinction diffusion flames.

The flow regime is also an important point to be addressed. Many practical applications of diffusion flames involve deflagration flames, which are combustion systems defined by a small characteristic flow velocity compared to the speed of sound (Poinsot and Veynante, 2011). To accurately model this type of system, the low-Mach approximation of the Navier-Stokes equations is often used. This approximation allows for the calculation of non-constant density flows while also neglecting acoustic effects, which also reduces the required temporal resolution. Explicit time marching algorithms are commonly used for simulations of deflagration flames using the low-Mach approximation, which enables a larger time step size and reduces computational time. However, implicit schemes can also be useful for simulating diffusion flames (Müller, 1998), enlarging even more the allowed time-steps for obtaining an accurate simulation.

Solution of the governing system of equations

Various solution strategies are available for solving the governing differential equations of fluid flow problems, which can be categorized into segregated and coupled methods.

In a segregated approach, the equations for each variable are solved sequentially and iteratively. The Semi-Implicit Method for Pressure Linked Equation (SIMPLE) algorithm is a popular segregated strategy for solving the discretized system of equations arising in CFD. Originally developed by Patankar (Patankar, 1980) using the Finite Difference Method (FDM), the SIMPLE algorithm has proven to be effective in solving a wide range of fluid flow problems. The SIMPLE algorithm was extended to work with other discretization methods as other numerical methods gained popularity. For instance, Ferziger and Perić (Ferziger and Perić, 2002) extended the SIMPLE algorithm to work with the FVM, while Haroutunian et al. (Haroutunian et al., 1993) extended it to work with the FEM. These extensions have allowed the SIMPLE algorithm to remain a popular choice for solving fluid flow problems, regardless of the numerical method used. In the context of high order methods, an extension of the SIMPLE algorithm for the DG method has been developed in the department of Fluid Dynamics at the

TU-Darmstadt, which is presented in the work from Klein (2015).

Another possibility is to utilize a coupled approach for solving the system of governing equations, where the system of equations is solved together, avoiding the need for decomposition into smaller, independent problems. In the fully coupled approach, each equation in the system can depend on the other equations. Fully coupled methods tend to be more robust than segregated methods, as they are less prone to convergence problems or oscillations, especially for problems with complex or nonlinear physics. However, they present the disadvantage that usually they are more computationally expensive. Nevertheless, it is expected from a fully coupled strategy that although the computational requirements are higher, the coupled solution of the system will require less iterations to find a convergent solution, leading to shorter calculation times and a more robust solution method. The solution of such coupled problems is often difficult, and specialized algorithms are required.

A point regarding the conservation of physical variables for segregated and coupled approaches is important to mention. In a segregated approach, the conservation of relevant physical variables, such as mass or momentum, is not guaranteed. In Knikker (2011) different strategies for solution of the low-Mach equations using segregated and coupled approaches are presented. None of the segregated strategies featured a fully conservative solution, as each of them needed to *sacrifice* the conservation of one of the solved equations. However, in case of the fully coupled algorithm the conservation is guaranteed provided that the solution of the fully coupled system is completely converged.

Generally speaking, the coupled solution of the Navier–Stokes equations require methods for handling the nonlinear systems of equations characteristic of fluid flow problems. For this purpose, methods such as Picard iteration and Newton’s method are often used. While both methods are iterative and designed for solving nonlinear systems, they differ in their approach to updating the solution at each iteration, as well as their computational cost and convergence properties.

Picard iteration is an iterative method used to solve nonlinear equations by generating a sequence of improved approximated solutions. In this method, the nonlinear equation is replaced with a linear equation that approximates the solution around a known solution. This known solution is usually an initial guess or an approximation from a previous iteration. The linearized equation is then solved for the new solution, which is used in the next iteration as the known solution. The Picard iteration solving strategy is widely used, as it is relatively simple to implement. It suffers however from stability problems, and relaxation factors are required to successfully bring the solution to convergence.

On the other hand, Newton methods are more complex and computationally expensive than Picard iteration methods, but they typically converge more reliably. Newton methods involve using the first derivative (Jacobian) of the equations to update the solution in each iteration, which is not always available. Furthermore, the classical Newton method relies on the assumption that the solution is near the initial guess, and may converge slowly or fail to converge if the initial guess is far from the true solution. Globalized Newton methods address this limitation by using globalization strategies that helps the method to converge to the true solution even if the initial guess is far from it. A clear advantage of this method over the Picard iterations is that no extra parameters (such as under-relaxation factors) have to be selected in order to bring the algorithm to convergence.

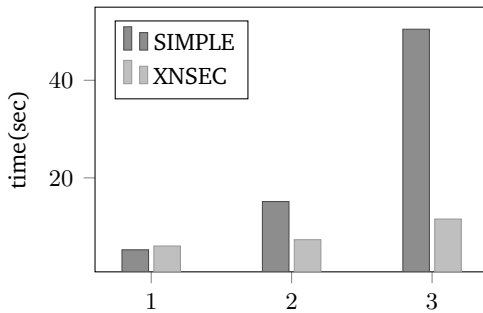


Figure 1.1: Runtime comparison of the DG-SIMPLE solver and the XNSEC solver for a typical non-isothermal simulation.

1.2 Objectives and motivation

The objective of this work is to present a solver for the fully-coupled simulation of low-Mach non-reactive and reactive flows using the DG method. Details about the discretization and solution process of the equations, various convergence supporting algorithms, and a exhaustive validation of the solver are presented. To the best of the author's knowledge, this is the first time that a fully coupled solver is used together with the DG method for solving the low-Mach equations using a globalized Newton method. While the current study focuses on two-dimensional configurations, the presented concepts could potentially be extended to three-dimensional systems. The solver presented in this thesis is embedded in the Bounded Support Spectral Solver (BoSSS) code, which is under active development at the chair of fluid dynamics of the Technical University of Darmstadt *. The presented solver received the name eXtended Navier-Stokes Equations solver for Combustion (XNSEC), where the term *extended* refers to the framework on which the solver is built, which focuses on applications for multi-phase flows using a sharp interface approach using a level-set method.

The present study employs the one-step combustion model proposed by Fernandez-Tarrazo et al. (2006) to describe the chemical reactions. While the present work only considers methane combustion, the one-step model could be applied to other hydrocarbons as well. The discrete system of equations is solved using a globalized Newton method with the Dogleg approach. Additionally, the study presents a homotopy strategy that has proven effective in obtaining solutions for highly nonlinear problems in steady-state calculations.

In order to find appropriate initial values for Newton's method in combustion applications, the concept of flame sheet estimates (i.e. the solution for infinitely fast chemistry) is used. Several benchmark cases are presented and used to validate the implementation of the solver, and also to highlight some of the benefits of the DG method and the strategies developed to support the convergence of the solver.

The main motivation for the development of a fully coupled solver comes from the necessity of a fast and robust algorithm for the solution of the low-Mach equations. In earlier investigations performed at the chair of fluid dynamics, a SIMPLE based algorithm for the solution of the low-Mach equations was implemented in the BoSSS framework (Klein et al., 2013; Klein et al., 2015; Klein et al., 2016). Although the SIMPLE based solver was capable of solving various variable density test-configurations, it was observed that the computation times were under

*The BoSSS code is open-source and is available under <https://github.com/FDYdarmstadt/BoSSS>

certain conditions very long. This is largely attributed to the difficulty of finding adequate under-relaxation factors for the solution algorithm of the nonlinear system. The strategy proposed in the present work proposes a fully coupled solution of the system of equations, where the nonlinear system is solved using a globalized Newton algorithm, which employs advanced heuristics to eliminate the necessity of user-defined parameters such as under-relaxation factors.

In Figure 1.1 a comparison of the computation times for simulation of a low-Mach number flow configuration using the fully coupled XNSEC solver and the SIMPLE algorithm based solver is shown. Although both algorithms allow the simulation of low-Mach number flows, clearly the SIMPLE algorithm requires much more time for almost all cases presented. The experiments demonstrate that choosing adequate under-relaxation factors is even more important for high order solutions. This highlights a fundamental advantage of the presented Newton method, where no extra parameters are needed.

1.3 Outline of the thesis

The thesis is structured as follows: In Chapter 2 the low-Mach number Navier-Stokes set of equations is presented. The general form of the governing equations is shown, and the main elements for the derivation of the low-Mach equations are concisely presented, emphasizing the assumptions made to arrive at them, as well as the models for the different physical parameters involved in the simulation. Later, the chemical model chosen for the combustion simulation is presented. Finally, the concept of the flame-sheet and the Burke-Schumann limit is shown, which are used within the solution algorithm for the solution of diffusion flame systems.

In Chapter 3 the numerical method used in this work is presented. First, a brief introduction to the DG method is given using a simple transport equation which allows demonstrating the procedure used for the spatial and temporal discretization of the governing equations. Later, a description of each of the discretized terms of the governing equations is shown, with special emphasis on the numerical fluxes involved.

The methods for solving the system of discretized equations are presented in Chapter 4. The chapter starts with a description of the solver structure. Later, the globalized Newton method used to solve the fully-coupled nonlinear system is shown. Particular emphasis is placed on the core algorithms of the method, as well as on crucial computational aspects that allow for a higher efficiency. Finally, additional strategies are presented that improve the convergence properties of the method for cases where the Newton algorithm is not able to obtain solutions, such as the use of the flame-sheet estimates for combustion simulations and homotopy methods for highly nonlinear problems.

In Chapter 5 a comprehensive validation of the solver using a variety of test cases is presented. These test cases are compared with benchmark results, but are also used for highlighting the algorithms introduced in this work. The test cases presented are subdivided in three sections, presented in increasing level of complexity. First, in Section 5.1 the solver is used to calculate typical incompressible benchmark cases, such as lid-driven cavity flow or a backward-facing step, and the results are compared with benchmark solutions. Then in Section 5.2 the tests are extended to low-Mach number flows, and several typical configurations are calculated for such systems, in particular problems for temperature dependant flow problems, such as the heated square cavity configuration, and the Rayleigh-Bénard Convection problem. Finally in Section 5.3 the fully coupled system of equations for reactive low-Mach flows is used for calculating some typical diffusion flame configurations. First a coflow flame configuration

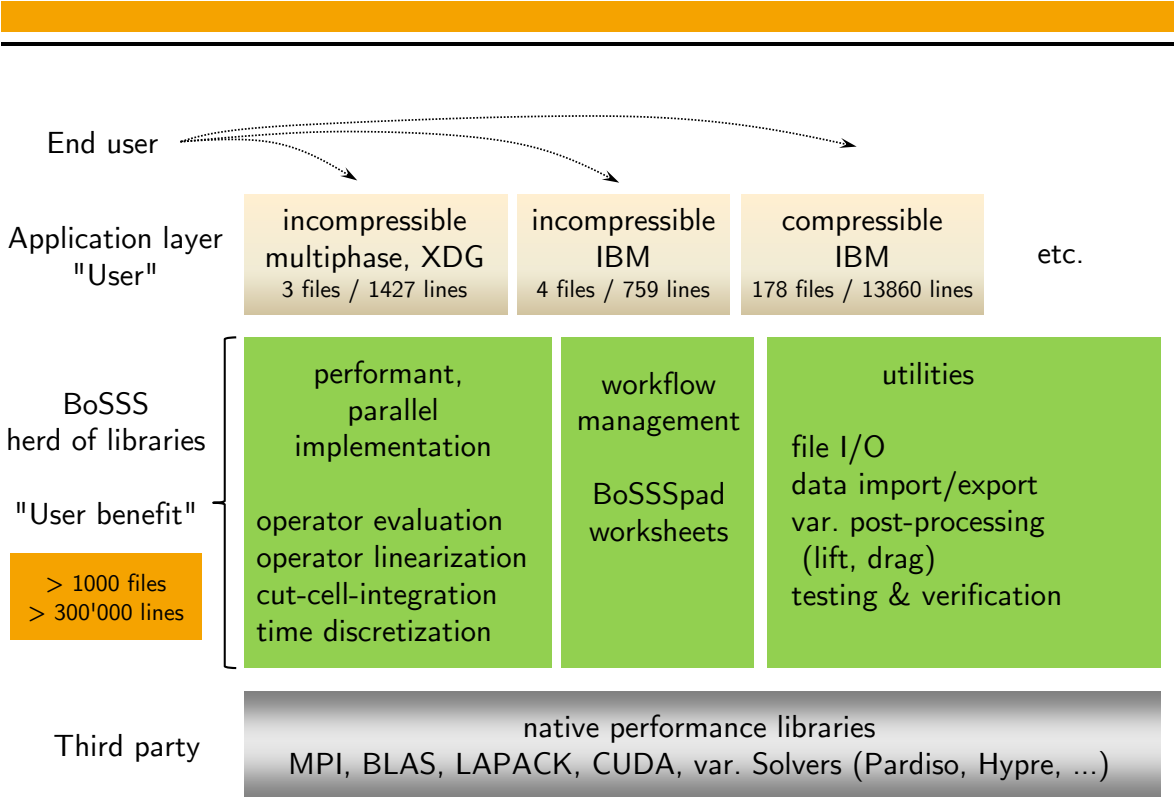


Figure 1.2: Schematic representation of the structure of the BoSSS solver. Extracted from the BoSSS handbook (Kummer et al., 2020).

is simulated. Later, a planar counterflow flame configuration is calculated, and the results are compared with simulations of the well known one-dimensional self similar solution of the flame. Finally Chapter 6 concludes the work and finishes with a short discussion.

Some results of the present thesis have been published by the author of this work (Gutiérrez-Jorquera and Kummer, 2022b).

1.4 The BoSSS code

BoSSS is a general framework for the discretization of conservation laws using the DG method and uses a modal DG approach with orthonormal Legendre polynomials as basis functions. The BoSSS code features a variety of applications in the context of CFD, such as a solver for multiphase flows with a sharp interface approach (Kummer, 2017), an incompressible Immersed Boundary Method solver for particle laden flows (Krause and Kummer, 2017), a solver for viscoelastic fluid flows (Kikker et al., 2020), and a solver for compressible flows (Geisenhofer et al., 2019), among others.

The structure of the BoSSS framework is shown in a schematic way in Figure 1.2. BoSSS allows the end user to develop sophisticated solvers at a very low coding effort. The implementation makes extensive use of several message-passing interface (MPI)-parallel, performance-optimized operations, among which the evaluation of the DG operator can be highlighted, as well as a solution using parallelized algorithms for the resolution of linear systems arising from the discretization. In addition, the user has at his disposal a large number of tools that optimize the workflow, such as the use of Jupyter-notebooks, as well as various post-processing tools.

2 Governing equations

The purpose of this chapter is to present the governing equations employed in this work, including a discussion of their derivation and the assumptions made.

In Section 2.1.1, the governing equations that enable the characterization of reactive fluids, in addition to other thermodynamic relationships, expressions for the transport parameters, and the one-step chemical model, are introduced. This is followed by the presentation of the process of nondimensionalizing the equations and the low-Mach limit of the governing equations in Section 2.1.2. As a part of the algorithm used to solve diffusion flame problems, a simplified form of the equations in which the reaction rate is assumed to be infinitely fast is used. The governing equations for such a system are presented in Section 2.2.

2.1 The low-Mach number equations for reactive flows

Combustion processes can be modeled by a system of nonlinear partial differential equations, namely the balance equations for the total mass, momentum, energy and mass of individual species (usually expressed in terms of mass fractions). This system needs to be solved together with an equation of state and expressions for the transport properties as well as for the chemical reaction rates.

The derivation of the governing equations for a reacting flow system can be found in the literature. For more information see for example the works from Kee et al. (2003) and Poinsot and Veynante (2011). In the following pages, the main ideas regarding the derivation of equations are presented. For a more detailed explanation, the interested reader is referred to the cited works and the references therein.

2.1.1 The reactive Navier–Stokes equations

Throughout this work, variables with a hat sign, for example \hat{p} , represent dimensional variables, while those without it are nondimensional. The derivation of the low-Mach number equations starts with the Navier–Stokes equations, the energy equation (written in its temperature form), and the species transport equations. Consider a reacting fluid mixture composed of N species. Let $\hat{\mathbf{x}} = (\hat{x}, \hat{y}, \hat{z})$ and \hat{t} be the spatial vector and time. The primitive variables are the velocity field $\hat{\mathbf{u}} = (\hat{u}, \hat{v}, \hat{w})$, the pressure \hat{p} , the temperature \hat{T} , and the mass fractions Y_k of the N total

species. The set of governing equations to be solved is

$$\frac{\partial \hat{\rho}}{\partial \hat{t}} + \hat{\nabla} \cdot (\hat{\rho} \hat{\mathbf{u}}) = 0, \quad (2.1a)$$

$$\frac{\partial \hat{\rho} \hat{\mathbf{u}}}{\partial \hat{t}} + \hat{\nabla} \cdot (\hat{\rho} \hat{\mathbf{u}} \otimes \hat{\mathbf{u}}) = -\hat{\nabla} \hat{p} - \hat{\nabla} \cdot \hat{\boldsymbol{\tau}} - \hat{\rho} \hat{\mathbf{g}}, \quad (2.1b)$$

$$\hat{\rho} \hat{c}_p \frac{\partial \hat{T}}{\partial \hat{t}} + \hat{\rho} \hat{c}_p \hat{\mathbf{u}} \cdot \hat{\nabla} \hat{T} = \frac{D\hat{p}}{Dt} - \hat{\nabla} \cdot \hat{\mathbf{q}} - \left(\hat{\rho} \sum_{k=1}^N \hat{c}_{p,k} Y_k \hat{\mathbf{U}}_k \right) \cdot \hat{\nabla} \hat{T} + \hat{\boldsymbol{\tau}} : \hat{\nabla} \hat{\mathbf{u}} + \hat{\omega}_T, \quad (2.1c)$$

$$\frac{\partial \hat{\rho} Y_k}{\partial \hat{t}} + \hat{\nabla} \cdot (\hat{\rho} \hat{\mathbf{u}} Y_k) = -\hat{\nabla} \cdot \hat{\mathbf{j}}_k + \hat{\omega}_k \quad (k = 1, \dots, N). \quad (2.1d)$$

In the general case this results in $N + 5$ differential equations to be solved. In these equations, $\hat{\rho}$ is the density of the mixture and $\hat{\mathbf{g}}$ is the acceleration of gravity. $\hat{\boldsymbol{\tau}}$, $\hat{\mathbf{q}}$ and $\hat{\mathbf{j}}_k$ are the viscous tensor, the heat flux vector and the molecular mass flux vector of species k , respectively. Additionally, $\hat{\omega}_T$ is the heat release from combustion and $\hat{\omega}_k$ is the reaction rate of species k . To close the system, expressions must be defined to link these variables with the primitive variables. They will be briefly shown and commented upon in the following paragraphs.

Equation of state

Assuming that the fluid behaves ideally, the density can be calculated as

$$\hat{\rho} = \frac{\hat{p} \hat{W}_{\text{avg}}}{\hat{R} \hat{T}}. \quad (2.2)$$

Here, \hat{R} is the universal gas constant of gases, and \hat{W}_{avg} is the average molecular weight of the fluid, defined as

$$\hat{W}_{\text{avg}} = \left(\sum_{k=1}^N \frac{Y_k}{\hat{W}_k} \right)^{-1}, \quad (2.3)$$

with \hat{W}_k being the molecular weight of species k . For an ideal mixture, the specific heat capacity can be calculated as a weighted average of the specific heats of the species

$$\hat{c}_p = \sum_{k=1}^N Y_k \hat{c}_{p,k}, \quad (2.4)$$

where $\hat{c}_{p,k}$ corresponds to the specific heat capacity of the component k . The temperature dependence of $\hat{c}_{p,k}$ can be accounted for by using NASA polynomials (Mcbride et al., 1993)

$$\hat{c}_{p,k} = \left(\hat{a}_1 + \hat{a}_2 \hat{T} + \hat{a}_3 \hat{T}^2 + \hat{a}_4 \hat{T}^3 + \hat{a}_5 \hat{T}^4 \right) \frac{\hat{R}}{\hat{W}_k}, \quad (2.5)$$

where $\hat{a}_1, \hat{a}_2, \hat{a}_3, \hat{a}_4$ and \hat{a}_5 are numerical coefficients supplied by the NASA database.

Transport models

The viscous tensor $\hat{\boldsymbol{\tau}}$ is defined for a Newtonian fluid as

$$\hat{\boldsymbol{\tau}} = -\hat{\mu} \left(\hat{\nabla} \hat{\mathbf{u}} + (\hat{\nabla} \hat{\mathbf{u}})^T \right) + \left(\frac{2}{3} \hat{\mu} - \hat{\kappa} \right) (\hat{\nabla} \cdot \hat{\mathbf{u}}) \mathbf{I}. \quad (2.6)$$

Here, $\hat{\mu}$ is the dynamic viscosity of the fluid, which is generally specific to the fluids and depends on its temperature and pressure. Furthermore, $\hat{\kappa}$ corresponds to the bulk viscosity, which is usually negligible for fluids at low pressures (Bird et al., 1960). In the rest of this work $\hat{\kappa}$ will be taken to be equal to zero.

The heat flux vector $\hat{\mathbf{q}}$ is given by Fourier's law of heat conduction,

$$\hat{\mathbf{q}} = \hat{\lambda} \hat{\nabla} \hat{T}. \quad (2.7)$$

Here, $\hat{\lambda}$ corresponds to the thermal conductivity, which, similar to viscosity, depends on the particular fluid under study as well as its temperature and pressure. Soret and Dufour effects are not considered in the present work.

The molecular mass flux vector $\hat{\mathbf{j}}_k$ of species k is defined as $\hat{\mathbf{j}}_k = \hat{\rho} \hat{\mathbf{U}}_k$, where $\hat{\mathbf{U}}_k$ is the diffusion velocity of the component k . In general, $\hat{\mathbf{U}}_k$ can be obtained by solving the Maxwell-Stefan equations

$$\nabla X_p = \sum_{k=1}^N \frac{X_p X_k}{D_{pk}} (\mathbf{U}_k - \mathbf{U}_p), \quad p = 1, \dots, N. \quad (2.8)$$

Here $D_{pk} = D_{kp}$ is the binary mass diffusion coefficient of species p into species k . X_p is the mole fraction of species k and is related to the mass fraction of k as $X_k = Y_k \hat{W}/\hat{W}_k$. The solution of Equations (2.8) is often a difficult and costly task (Williams, 2000; Poinsot and Veynante, 2011), and often simplifications are made. It can be shown that for binary mixtures ($N = 2$), and for mixtures containing multiple species ($N > 2$) with equal diffusion coefficients, Equations (2.8) reduce exactly to the well-known Fick's law

$$\hat{\mathbf{j}}_k = -\rho \hat{D}_k \nabla Y_k. \quad (2.9)$$

This expression is exact only in the cases mentioned above. The variable \hat{D}_k corresponds in this case to the diffusion coefficient of species k in the mixture. An issue related to global mass conservation can be noted here. Recall that by definition, the sum of the mass fractions must always be one, namely $\sum_{k=1}^N Y_k = 1$. However, this is only true for the solution of Equations (2.1) if exact expressions for diffusion velocities are used (Poinsot and Veynante, 2011). However, if some inexact expression is used (as for example Fick's law), the constraint for the sum of the mass fractions will not be fulfilled. This problem can be circumvented by solving the global mass conservation equation and the equations for the first $N - 1$ species. By doing so, all inconsistencies originating from not using an exact species diffusion model are absorbed by Y_N . As pointed out in Poinsot and Veynante (2011), this simplification should only be used if all $N - 1$ species are strongly diluted in species N , such as the case of a flame in air, where the mass fraction of nitrogen is large. This approach reduces the number of differential equations needed to be solved by one, slightly alleviating computational requirements.

The temperature dependence of viscosity is modeled by Sutherland's law (Sutherland, 1893)

$$\hat{\mu}(\hat{T}) = \hat{\mu}_{\text{suth}} \left(\frac{\hat{T}}{\hat{T}_{\text{suth}}} \right)^{1.5} \frac{\hat{T}_{\text{suth}} + \hat{S}}{\hat{T} + \hat{S}}. \quad (2.10)$$

Here $\hat{\mu}_{\text{suth}}$ is the viscosity evaluated at a reference temperature \hat{T}_{suth} , and \hat{S} is a material-dependent parameter. In all calculations in this work, the value of \hat{S} for air is used, i.e. $\hat{S} = 110.5$ K. Expressions for determining the thermal conductivity and diffusion coefficients as a function of temperature can be obtained using similar expressions, as shown later in Section 2.1.2.

The enthalpy transport term due to diffusive fluxes (third term on the right hand side of Equation (2.1c)) usually has only a small influence on the solution (Smoke and Giovangigli (1991), Goey et al. (1995), and Paxion et al. (2001)), and it is actually exactly equal to zero for systems where all species heat capacities are equal. In the present formulation this term is neglected from the energy equation.

Chemical model

As mentioned in the introduction, the task of choosing and implementing a suitable chemical model to accurately and efficiently represent the combustion process presents a considerable challenge. While normally a detailed depiction of the chemistry is preferable, it can become computationally intensive and impractical. For example, in the work of Stauch et al. (2006) a numerical investigation of methanol combustion using detailed chemistry is carried out, and involves the analysis of 23 chemical species and 166 elementary reactions. Because of their high complexity, solvers using detailed chemistry are often restricted to simple one- or two-dimensional configurations, and to a small number of grid elements. If one is interested in more complex geometries or more complicated flow systems, the use of detailed kinetics can be prohibitive. To address this challenge, researchers often use specialized methods and model reduction techniques to handle species transport efficiently. Some common approaches include the use of look-up tables or the use of global schemes (Poinsot and Veynante, 2011). Another popular approach involves employing reduced chemical reaction models, specially formulated to optimize computational efficiency while maintaining fidelity to the underlying physical processes.

Regarding the last point mentioned, in the work of Westbrook and Dryer (1981) a one-step kinetic model is presented, where combustion is expressed as a single chemical reaction with a reaction rate given by an Arrhenius-type expression with constant parameters. Multi-step chemical reaction models have also been developed, such as the four-step mechanism for methane combustion by Peters (1985) or the three-step mechanism by Peters and Williams (1987). In the present work, the chemical model proposed by Fernandez-Tarrazo et al. (2006) for hydrocarbon combustion with air is used. It will be introduced in the next pages.

Consider a system composed of N species where M chemical reactions take place. Chemical reactions can be written in generalized form as

$$\sum_{k=1}^N \nu'_{kj} \mathcal{M}_k \rightleftharpoons \sum_{k=1}^N \nu''_{kj} \mathcal{M}_k \quad \text{for } j = 1, \dots, M, \quad (2.11)$$

where ν'_{jk} and ν''_{jk} are the molar stoichiometric coefficients of species k in the chemical reaction j , and \mathcal{M}_k represents the chemical component k .

The reaction rate of species k is $\hat{\omega}_k$, which accounts for the net change in the total amount of species k due to M chemical reactions. Its given by

$$\hat{\omega}_k = \hat{W}_k \sum_{j=1}^M \nu_{jk} \hat{Q}_j. \quad (2.12)$$

Here $\nu_{kj} = \nu''_{kj} - \nu'_{kj}$, and \hat{Q}_j is the rate of progress of the reaction j , which is usually modeled using Arrhenius-type expressions.

\hat{B} (cm ³ /(mol s))	\hat{T}_{a0} (K)	\hat{Q}_0 (MJ kmol ⁻¹)	a	b
6.9×10^{14}	15 900	802.4	1	1

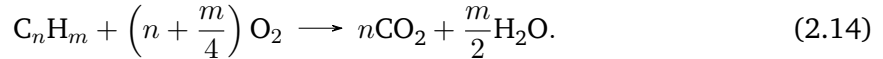
Table 2.1: Base parameters used in the one-step combustion model by Fernandez-Tarrazo et al. (2006)

The heat release $\hat{\omega}_T$ that appears in the energy equation is related to the reaction rates according to

$$\hat{\omega}_T = - \sum_{k=1}^N \hat{h}_k \hat{\omega}_k = - \sum_{k=1}^N \Delta \hat{h}_k^0 \hat{\omega}_k - \sum_{k=1}^N \hat{h}_{ks} \hat{\omega}_k. \quad (2.13)$$

Here, the specific enthalpy of k -th species \hat{h}_k is written in terms of its formation enthalpy \hat{h}_k^0 and a sensible enthalpy $\hat{h}_{ks} = \int_0^{\hat{T}} \hat{c}_{p,k} d\hat{T}$. The second term on the right-hand side of Equation (2.13) is usually small and is exactly zero for a mixture in which all the heat capacities of each component are equal (Poinsot and Veynante, 2011). It will be neglected in the rest of the analysis.

In this work, the one-step kinetic model for the combustion of hydrocarbons presented in Fernandez-Tarrazo et al. (2006) is used. The chemical reaction is represented by a single ($M = 1$) exothermic global irreversible expression as



with n and m denoting the number of carbon and hydrogen atoms composing a molecule of fuel. The rate of progress of the global reaction is modeled by an Arrhenius-type expression

$$\hat{Q} = \hat{B} e^{-\hat{T}_a/\hat{T}} \left(\frac{\hat{\rho} Y_F}{\hat{W}_F}\right)^a \left(\frac{\hat{\rho} Y_O}{\hat{W}_O}\right)^b. \quad (2.15)$$

Here, the subscripts F and O refer to fuel and oxidizer, respectively. The parameter \hat{B} corresponds to the pre-exponential factor, \hat{T}_a is the activation temperature, and a and b are reaction orders. For a one-step reaction model, the reaction rate of the k -th component in Equation (2.12) is

$$\hat{\omega}_k = \nu_k \hat{W}_k \hat{Q}. \quad (2.16)$$

With this definition, the heat release $\hat{\omega}_T$ in Equation (2.13) yields

$$\hat{\omega}_T = -\hat{W}_F \hat{\omega}_F \hat{Q}^m = -\hat{\omega}_F \hat{Q}. \quad (2.17)$$

Here \hat{Q}^m is the molar heat of reaction of the one-step reaction and \hat{Q} is the mass heat of reaction. \hat{W}_F and $\hat{\omega}_F$ are the molar mass of the fuel species and the reaction rate of the fuel species respectively.

Within the model proposed by Fernandez-Tarrazo et al. (2006), several parameters are adjusted to represent characteristic features of premixed flames and diffusion flames. In particular, the parameters \hat{T}_a and \hat{Q} are defined as functions of the local equivalence ratio ϕ , which is, in turn, is defined in terms of the local mass fractions of fuel Y_F and oxidizer Y_O as

$$\phi = \frac{s Y_F^0}{Y_O^0} \frac{s Y_F - Y_O + Y_O^0}{s(Y_F^0 - Y_F) + Y_O}, \quad (2.18)$$

where Y_F^0 and Y_O^0 are the mass fractions of the fuel and oxidizer flows in their corresponding feed streams, and s is the mass stoichiometric ratio, defined as $s = \nu_O \hat{W}_O / \nu_F \hat{W}_F$. The activation energy depends on ϕ as

$$\hat{T}_a(\phi) = \begin{cases} (1 + 8.250(\phi - 0.64)^2)\hat{T}_{a0} & \text{if } \phi \leq 0.64, \\ \hat{T}_{a0} & \text{if } 0.64 \leq \phi \leq 1.07, \\ (1 + 4.443(\phi - 1.07)^2)\hat{T}_{a0} & \text{if } \phi \geq 1.07, \end{cases} \quad (2.19)$$

and the molar heat release according to

$$\hat{Q}(\phi) = \begin{cases} \hat{Q}_0 & \text{if } \phi \leq 1, \\ (1 - \alpha(\phi - 1))\hat{Q}_0 & \text{if } \phi > 1. \end{cases} \quad (2.20)$$

The parameter α is a constant that depends on the hydrocarbon being considered, in particular $\alpha = 0.21$ for methane combustion.

It should be noted that Equation (2.20) yields nonphysical values of \hat{Q} for large values of ϕ . This problem can be avoided by setting an upper boundary value for ϕ in Equation (2.20). However, in practice, this should not have a significant effect because the non-physical values of \hat{Q} appear in zones where the reaction rate $\hat{\omega}$ is very close to zero, making the factor $\hat{Q}\hat{\omega}$ in the temperature equation negligible. However, setting an upper bound for ϕ is helpful for avoiding possible numerical instabilities.

2.1.2 The reactive low-Mach Navier-Stokes equations

In the present work, the low-Mach number approximation of the governing equations is used. They were first derived by Rehm and Baum (1978). A rigorous extension to combustion problems was done by Majda and Sethian (1985). The interested user is referred to these references for a detailed explanation of how the set of equations is derived, as well as the work from Müller (1998). In what follows, only the main consequences of the low-Mach limit will be shown and discussed.

Recall the definition of the Mach number, $\text{Ma} = \hat{u}_{\text{ref}}/\hat{c}$, where \hat{u}_{ref} is a characteristic flow velocity and \hat{c} the speed of sound. The low-Mach number limit approximation of the governing equations is used for flows where the Mach number is small, which is usually the case in typical laminar combustion systems (Dobbins and Smooke, 2010). The low-Mach equations are obtained by using standard asymptotic methods. One of the main results of the analysis is that for flows with a small Mach number, the pressure can be decomposed as

$$\hat{p}(\hat{\mathbf{x}}, \hat{t}) = \underbrace{\hat{p}_0(\hat{t})}_{\mathcal{O}(1)} + \underbrace{\hat{p}_2(\hat{\mathbf{x}}, \hat{t})}_{\mathcal{O}(\text{Ma}^2)}. \quad (2.21)$$

The spatially uniform term $\hat{p}_0(\hat{t})$ is called thermodynamic pressure and only influences the system through the equation of state. It is constant in space but can change in time. For an open system, the thermodynamic pressure is also constant in time and equal to the ambient pressure, while for a closed system (e.g. a system completely bounded by walls) it changes, ensuring mass conservation.

On the other hand, the perturbational term $\hat{p}_2(\hat{\mathbf{x}}, \hat{t})$ appears only in the momentum equations and plays a role similar to that of the pressure in the classical incompressible formulation. This

perturbational term satisfies $\hat{p}_2/\hat{p} \sim \mathcal{O}(\text{Ma})^2$ (Dobbins and Smooke, 2010; Nonaka et al., 2018) showing that the equation of state is satisfied only to $\mathcal{O}(\text{Ma}^2)$.

Effectively, the low-Mach limit of the Navier-Stokes equations allows the calculation of systems where large density variations due to temperature differences are present, thus the formulation is not restricted to approximations such as the Boussinesq approximation for buoyancy-driven flow. In addition, this approximation truncates the mechanism of pressure wave propagation, which is a natural feature of the compressible Navier-Stokes equations, but is negligible for low velocity flows. By doing this the necessity of small time-steps for resolving the wave phenomenon is completely removed and the maximum allowed time-step is greatly increased.

In this work a nondimensional formulation of the governing equations is used. Following nondimensional quantities are defined

$$\begin{aligned}\rho &= \frac{\hat{\rho}}{\hat{\rho}_{\text{ref}}}, & p &= \frac{\hat{p}}{\hat{p}_{\text{ref}}}, & \mathbf{u} &= \frac{\hat{\mathbf{u}}}{\hat{u}_{\text{ref}}}, & T &= \frac{\hat{T}}{\hat{T}_{\text{ref}}}, & c_p &= \frac{\hat{c}_p}{\hat{c}_{p,\text{ref}}}, & W_k &= \frac{\hat{W}_k}{\hat{W}_{\text{ref}}}, \\ \mu &= \frac{\hat{\mu}}{\hat{\mu}_{\text{ref}}}, & D_k &= \frac{\hat{D}_k}{\hat{D}_{k,\text{ref}}}, & k &= \frac{\hat{k}}{\hat{k}_{\text{ref}}}, & \nabla &= \frac{\hat{\nabla}}{\hat{L}_{\text{ref}}}, & t &= \frac{\hat{t}}{\hat{t}_{\text{ref}}}, & \mathbf{g} &= \frac{\hat{\mathbf{g}}}{\hat{g}_{\text{ref}}}, & Q &= \frac{\hat{Q}}{\hat{Q}_0}.\end{aligned}$$

Here \hat{u}_{ref} , \hat{L}_{ref} , \hat{p}_{ref} , \hat{t}_{ref} , and \hat{T}_{ref} are the reference velocity, length, pressure, time, and temperature, respectively, and are equal to some characteristic value for the particular studied configuration. Furthermore, \hat{g}_{ref} is the magnitude of the gravitational acceleration and \hat{W}_{ref} is the reference molecular weight. The reference transport properties $\hat{\mu}_{\text{ref}}$, \hat{k}_{ref} , $\hat{D}_{k,\text{ref}}$ and the reference heat capacity of the mixture $\hat{c}_{p,\text{ref}}$ are evaluated at the reference temperature \hat{T}_{ref} . Similarly, the reference density must satisfy the equation of state, thus $\hat{\rho}_{\text{ref}} = \hat{p}_{\text{ref}}\hat{W}_{\text{ref}}/(\hat{\mathcal{R}}\hat{T}_{\text{ref}})$. By introducing these definitions into the governing Equations (2.1a) to (2.1d), together with the transport coefficients and equations for the source terms ω_T and ω_k given by the one-step model, the nondimensional low-Mach number set of equations is obtained

$$\frac{\partial \rho}{\partial t} + \nabla \cdot (\rho \mathbf{u}) = 0, \quad (2.22a)$$

$$\frac{\partial \rho \mathbf{u}}{\partial t} + \nabla \cdot (\rho \mathbf{u} \otimes \mathbf{u}) = -\nabla p + \frac{1}{\text{Re}} \nabla \cdot \mu \left(\nabla \mathbf{u} + \nabla \mathbf{u}^T - \frac{2}{3} (\nabla \cdot \mathbf{u}) \mathbf{I} \right) - \frac{1}{\text{Fr}^2} \rho \mathbf{g}, \quad (2.22b)$$

$$\frac{1}{\gamma} \frac{\partial \rho T}{\partial t} + \nabla \cdot (\rho \mathbf{u} T) = \frac{1}{\text{Re} \text{Pr}} \nabla \cdot \left(\frac{k}{c_p} \nabla T \right) + \text{H Da} \frac{Q \mathcal{Q}}{c_p}, \quad (2.22c)$$

$$\frac{\partial \rho Y_k}{\partial t} + \nabla \cdot (\rho \mathbf{u} Y_k) = \frac{1}{\text{Re} \text{Pr} \text{Le}_k} \nabla \cdot (\rho D \nabla Y_k) + \text{Da} \nu_k W_k \mathcal{Q}, \quad k = 1, \dots, N-1. \quad (2.22d)$$

This system is solved for the primitive variables velocity $\mathbf{u} = (u_x, u_y)$, pressure p , temperature T and mass fractions $\mathbf{Y}' = (Y_1, \dots, Y_{N-1})$. An advantage of using the temperature as a primitive variable is that in doing so, the temperature dependant transport parameters and equation of state can be readily calculated, and no intermediate calculation needs to be done. Note that it is assumed that the spatial gradients of the mixture heat capacity are small, which allows to introduce c_p in the derivative of the diffusive term of Equation (2.22c). Furthermore, considering the fact that the sum of the mass fractions must always be one, the mass fraction of the last species N can be calculated with

$$Y_N = 1 - \sum_{k=1}^{N-1} Y_k. \quad (2.23)$$

Note that the form of the low-Mach equations is very similar to the Navier-Stokes equations. The major difference is in the decomposition of the pressure. This similarity is beneficial as it allows the use of similar techniques to solve the PDE system to those used for the completely incompressible case (Keshtiban et al., 2003). From now on, the sub-index of the hydrodynamic pressure \hat{p}_2 will be dropped and it will be called simply \hat{p} , further emphasizing the similarity in its role to the pressure of the incompressible equations.

Six nondimensional factors arise from the nondimensionalization process:

$$\begin{aligned} \text{Re} &= \frac{\hat{\rho}_{\text{ref}} \hat{u}_{\text{ref}} \hat{L}_{\text{ref}}}{\hat{\mu}_{\text{ref}}}, & \text{Fr} &= \frac{\hat{u}_{\text{ref}}}{\sqrt{\hat{g}_{\text{ref}} \hat{L}_{\text{ref}}}}, & \text{Pr} &= \frac{\hat{c}_{p,\text{ref}} \hat{\mu}_{\text{ref}}}{\hat{k}_{\text{ref}}}, \\ \text{Le}_k &= \frac{\hat{k}_{\text{ref}}}{\hat{\rho}_{\text{ref}} \hat{D}_{k,\text{ref}} \hat{c}_{p,\text{ref}}}, & \text{Da} &= \frac{\hat{B} \hat{L}_{\text{ref}} \hat{\rho}_{\text{ref}}}{\hat{M}_{\text{ref}} \hat{u}_{\text{ref}}}, & \text{H} &= \frac{\hat{Q}_0}{\hat{c}_{p,\text{ref}} \hat{T}_{\text{ref}}}. \end{aligned}$$

The first three equations define the Reynolds, Froude and Prandtl number, respectively. Le_k is the Lewis number of species k . Finally, Da and H are the Damköhler number and the nondimensional heat release, respectively. The nondimensional progress of the global reaction reads as follows

$$\mathcal{Q}(T, \mathbf{Y}) = \exp \left(\frac{-T_a}{T} \right) \left[\left(\frac{\rho Y_F}{M_F} \right) \left(\frac{\rho Y_O}{M_O} \right) \right], \quad (2.24)$$

where $T_a = \hat{T}_a / \hat{T}_{\text{ref}}$. Furthermore, the nondimensional heat release is

$$Q(\phi) = \begin{cases} 1 & \text{if } \phi \leq 1, \\ (1 - \alpha(\phi - 1)) & \text{if } \phi > 1. \end{cases} \quad (2.25)$$

with ϕ evaluated according to Equation (2.18). In the low-Mach limit, the ideal gas equation depends on the thermodynamic pressure, temperature and mass fractions. It reads in its nondimensional form

$$\rho(p_0, T, \mathbf{Y}) = \frac{p_0}{T \sum_{k=1}^N \frac{Y_k}{W_k}}. \quad (2.26)$$

As mentioned previously, in a closed system, the thermodynamic pressure must be determined to ensure mass conservation. Conversely, in an open system, the pressure is equal to the atmospheric pressure. By integrating Equation (2.26) into the entire domain Ω , the expression

$$p_0(T, \mathbf{Y}) = \frac{m_0}{\int_{\Omega} \left(T \sum_{k=1}^N \frac{Y_k}{W_k} \right)^{-1} dV} \quad (2.27)$$

can be derived. Here, $m_0 = \int_{\Omega} \rho dV$ is the mass of the fluid in the closed system. Since in a closed system the total mass is constant, it can be determined using initial conditions. Similarly, the nondimensional specific heat capacity of the mixture c_p is calculated as

$$c_p(T, \mathbf{Y}) = \sum_{k=1}^N Y_k c_{p,\alpha}, \quad (2.28)$$

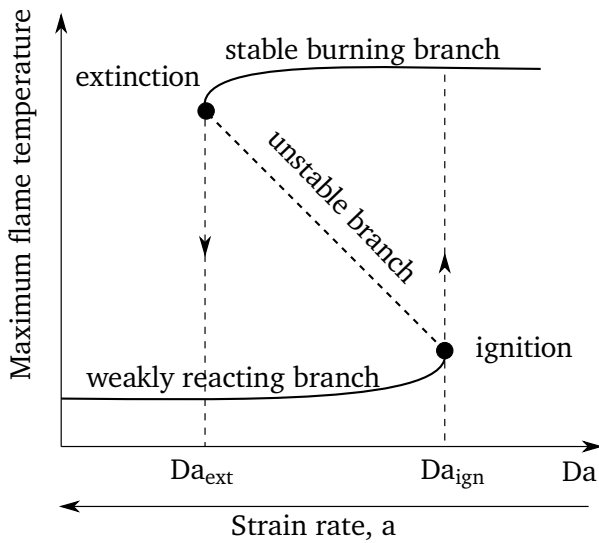


Figure 2.1: S-shaped bifurcation curve of a combustion process.

and the nondimensional viscosity as

$$\mu(T) = T^{\frac{3}{2}} \frac{1 + \hat{S}}{\hat{T}_{\text{ref}} T + \hat{S}}. \quad (2.29)$$

The model for the transport parameters can be simplified by assuming constant values for the Prandtl and Lewis numbers (Smoke and Giovangigli, 1991). The nondimensional transport parameters are related in that case with

$$\mu = k/c_p = \rho D. \quad (2.30)$$

2.1.3 A note on the multiple solutions of the system

The system of equations shown in this section has the particularity that its solution presents branching phenomena, which means that there are several solutions to the problem. The presence of branching solutions often arises in nonlinear or complex systems, where multiple stable or unstable states can exist, leading to various possible solutions for the given set of equations, depending on the initial conditions considered for the solution.

In context of the reactive equations presented above, one solution is evidently that of pure mixing (also called frozen chemistry), in which combustion does not occur and the equations are simply describing a mixing process. Another solution is that of a system under combustion, where the reaction takes place in a thin but finite reaction zone, in which the reactants can overlap. This phenomenon is usually represented by a bifurcation curve of the combustion process, as shown in Figure 2.1 in which the maximum temperature of the system is plotted for different Dahmköhler numbers.

The graph also shows the ignition and extinction points. If a system is in the stable combustion branch, and the Dahmköhler number begins to decrease there is a point where the chemical reaction is not sustainable, and the extinction phenomenon occurs. An example of this is the case of extinguishing a candle by blowing it out. The ignition phenomenon can be interpreted analogously. For a system where there is no chemical reaction (but mixing of the reactants),

the increase of the Dahmköhler number eventually leads to ignition of the system, obtaining a flame that is in the stable combustion branch. An example of this would be when a lighter produces a flame as a result of a spark.

Several strategies can be recognized to obtain a solution for a steady-state diffusion flame. Clearly, one sensible way would be to numerically represent the ignition process by including a high temperature zone in the initial conditions of the system and advance it in time using a marching algorithm. From a numerical point of view this posses several challenges. For instance, in a diffusion flame, it is not clear in advance the exact location of the high reaction zones, and positioning the high temperature patch in a distant zone does not guarantee ignition of the system. Furthermore, the temperature has to be large enough to cause ignition of the system, and the large spatial gradients associated make necessary an adequate meshing strategy to obtain converged solutions. If one is only interested in the steady state solution, an implicit time stepping method with a large time-step could be used. This requires, however, a very good initial estimate to obtain a convergent solution. In the next section a strategy is presented that allows to obtain systems of steady state combustion, which does not require the simulation of the ignition process.

2.2 The flame sheet approximation

The reactive low-Mach equations exhibit a high nonlinear nature, displaying a remarkably strong interplay between fluid dynamics and thermochemistry. The numerical solution of the fully coupled discretized equations can be realized in different ways, one of them being the use of Newton algorithm to find the solution in an iterative manner. This requires however the use of adequate initial estimates which make possible the algorithm to find a converged solution. Not using an adequate estimate could lead to a very slow convergence, or even to divergence of the algorithm. As previously mentioned, the initial estimate should also be carefully selected to ensure that the nonlinear solver delivers the ignited solution. In this part a strategy for obtaining an adequate initial estimate is presented.

The rate of reaction in a diffusion flame is determined by the rate at which the fuel and oxidizer are brought together. If one considers the limit of infinitely fast chemical reaction, the reactants are separated by a thin exothermic layer. The highest temperature is located at the point where reactants meet in stoichiometric proportions maximizing the production of combustion products. The use of such a infinitely fast reaction model provides a good initial estimate that can be used to find a solution for the steady state systems with a finite reaction rate, and has been used in various works, such as the work from Keyes and Smooke (1987) where the idea is used in a counterflow configuration, and in the work of Smooke et al. (1986a) for an axisymmetric coflow configuration, also in Smooke and Giovangigli (1992) for a Tsuji-counterflow configuration and in the work by Dobbins and Smooke (2010) for an axisymmetric laminar jet diffusion flame with time dependent boundary conditions.

A set of governing equations for systems with infinite reaction rates can be written. This requires assuming that all species have the same heat capacity $c_{p,k} = c_p$ and mass diffusion coefficient $D_k = D$, that the Lewis number is unity for all species, and that combustion can be described by a single step chemical reaction. By taking a linear combination of the energy Equation (2.22c) and mass fractions Equation (2.22d), an equation for a passive scalar can be written. Thus, the system can be simplified to solving the low-Mach Navier-Stokes equations

Variable	Fuel value	Oxidizer value
Fuel mass fraction, Y_F	Y_F^0	0
Oxidizer mass fraction, Y_O	0	Y_O^0
Temperature, T	T_F^0	T_O^0
Mixture Fraction, z	1	0

Table 2.2: Boundary conditions of reactants mass fractions, temperature and mixture fraction. Adapted from Poinsot and Veynante (2011).

and an equation for a scalar z :

$$\frac{\partial \rho}{\partial t} + \nabla \cdot (\rho \mathbf{u}) = 0, \quad (2.31a)$$

$$\frac{\partial \rho \mathbf{u}}{\partial t} + \nabla \cdot (\rho \mathbf{u} \otimes \mathbf{u}) = -\nabla p + \frac{1}{Re} \nabla \cdot \mu \left(\nabla \mathbf{u} + \nabla \mathbf{u}^T - \frac{2}{3} (\nabla \cdot \mathbf{u}) \mathbf{I} \right) - \frac{1}{Fr^2} \rho \mathbf{g}, \quad (2.31b)$$

$$\frac{\partial \rho z}{\partial t} + \nabla \cdot (\rho \mathbf{u} z) = \frac{1}{Re Pr} \nabla \cdot (\rho D \nabla z). \quad (2.31c)$$

Here z is the mixture fraction, which is a scalar that measures the local fuel/oxidizer ratio (Poinsot and Veynante, 2011). Note that Equation (2.31c) is simply a diffusion-convection equation. It is however still coupled to the flame structure via the velocity fields and through the density (and indirectly to the temperature and mass fractions fields, as will be shown later), requiring an iterative procedure for the solution of the coupled system. In Table 2.2 the boundary conditions for a non-premixed systems are indicated. There Y_F and Y_O represent the fuel and oxidizer mass fractions, respectively. The variables Y_F^0 and Y_O^0 indicate the fuel and oxidizer mass fraction at their respective inlet zone. Furthermore the variable z is per definition equal to unity in the fuel feed stream and equal to zero in the oxidizer feed stream.

Note that the system of governing equations is not closed, because ρ , μ and ρD are still functions of the temperature and mass fractions. These fields can be related to the mixture fraction using the flame structure concept presented in the seminal publication from Burke and Schumann (1928).

The procedure described before for obtaining the equation for the mixture fraction z leads to expressions that relate z to the temperature T , mass fraction of the fuel Y_F and the mass fraction of the oxidizer Y_O as

$$z = \frac{sY_F - Y_O + Y_O^0}{sY_F^0 + Y_O^0} = \frac{\frac{c_p}{Q}(T - T_O^0) + Y_F}{\frac{c_p}{Q}(T_F^0 - T_O^0) + Y_F^0} = \frac{\frac{sc_p}{Q}(T - T_O^0) + Y_O - Y_O^0}{\frac{sc_p}{Q}(T_F^0 - T_O^0) + Y_O^0}. \quad (2.32)$$

In the case of an infinitely fast chemical reaction, fuel and oxidizer cannot coexist. On one side of this sheet only oxidizer is found, and on the other side only fuel. The exact position of the flame sheet can be determined using Equation (2.32) by the location of the points where the reactant mass fractions Y_F and Y_O are zero, that is, the points where the mixture fraction $z = z_{st}$, with

$$z_{st} = \frac{Y_O^0}{Y_O^0 + sY_F^0}. \quad (2.33)$$

The Burke-Schumann flame structure provides analytical expressions for temperature and mass fraction fields on either side of the flame sheet as a function of the mixture fraction z . For a

2.2. Flame Sheet Approximation

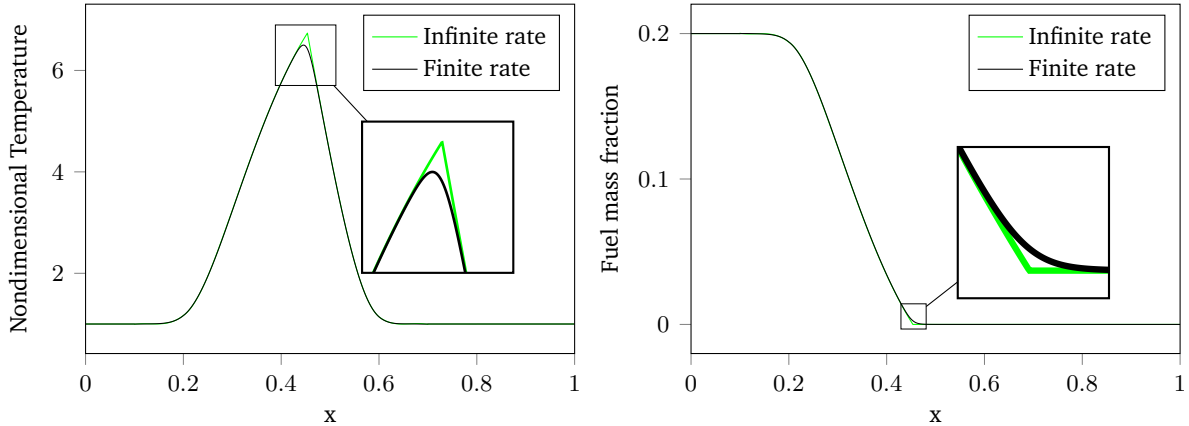


Figure 2.2: Temperature and fuel mass fraction profiles calculated in the center-line of a counter-flow flame configuration using finite chemistry (black) and the flame sheet approximation (green).

more detailed derivation see for example the textbook from Poinsot and Veynante (2011) or the work from Keyes and Smooke (1987). The temperature is related to the mixture fraction as

$$T(z) = \begin{cases} zT_F^0 + (1-z)T_O^0 + \frac{QY_F^0}{c_p}z_{st}\frac{1-z}{1-z_{st}} & \text{if } z \geq z_{st}, \\ zT_F^0 + (1-z)T_O^0 + \frac{QY_F^0}{c_p}z & \text{if } z < z_{st}. \end{cases} \quad (2.34)$$

The mass fraction field of fuel and oxidizer species at either side of the flame is given by:

$$Y_F(z) = \begin{cases} Y_F^0\frac{z - z_{st}}{1 - z_{st}} & \text{if } z \geq z_{st}, \\ 0 & \text{if } z < z_{st}, \end{cases} \quad (2.35)$$

$$Y_O(z) = \begin{cases} 0 & \text{if } z \geq z_{st}, \\ Y_O^0\left(1 - \frac{z}{z_{st}}\right) & \text{if } z < z_{st}. \end{cases} \quad (2.36)$$

Finally, the mass fraction field of product species P is:

$$Y_P(z) = \begin{cases} Y_O^0\frac{W_P\nu_P}{W_O\nu_O}(1-z) & \text{if } z \geq z_{st}, \\ Y_F^0\frac{W_P\nu_P}{W_F\nu_F}z & \text{if } z < z_{st}. \end{cases} \quad (2.37)$$

Once the mixture fraction field z is obtained, the temperature and mass fraction fields are uniquely defined by Equations (2.34) to (2.37), which are used to evaluate the density and the transport properties. This allows to use an iterative scheme for the solution of the coupled equations.

Note that the expressions shown above (and by extension the density and transport properties) are not differentiable at the stoichiometric point $z = z_{st}$. This poses a challenge for numerical algorithms (Rauwoens et al., 2009), and some form of smoothing could be helpful for finding solutions. Later in Section 4.4.3 this point will be treated.

It is worth noting that the assumption of infinite reaction rate can be interpreted as an infinite Dahmköhler number, where the chemical time scales are much shorter than the flow scales. It is expected that the initial estimate using the flame-sheet is a good approximation for finite reaction rate systems where the Dahmköhler number is very large, or expressed differently, for conditions far away from the extinction point (see Figure 2.1).

Under certain conditions, the the flame-sheet approximation is indeed a very good initial guess. In Figure 2.2, temperature and fuel mass fraction fields obtained with infinite and finite reaction rate across the center-line of a counterflow flame configuration are shown. Clearly, both solutions are very similar, differing only in the area immediately near the flame. However, this similarity is only valid under the assumptions made to derive Equation (2.31c). In the case that the Lewis number is not equal to one, or that the heat capacities are not equal for each species, the finite-rate solution will differ slightly from that obtained for the flame sheet. Note that the assumption of unity Lewis number of the flame sheet formulation is not mandatory (Liñán et al., 1994).

The use of the flame-sheet solution provides a logical and natural initial guess for a steady state simulation of a diffusion flame with finite reaction rates. Furthermore, for the case of a transient simulation, the flame sheet could also provide a means of initializing the solution of the system, circumventing the need of simulating ignition phenomena.

2.3 Boundary conditions

The following boundary conditions are imposed for the resolution of the finite reaction rate system (Equations (2.22a) to (2.22d)) and for the flame sheet problem (Equations (2.31a) to (2.31c)),

$$\Gamma_D : \mathbf{u} = \mathbf{u}_D, \quad T = T_D, \quad Y_k = Y_{k,D}, \quad z = z_D, \quad (2.38a)$$

$$\Gamma_{DW} : \mathbf{u} = \mathbf{u}_D, \quad \nabla T \cdot \mathbf{n}_{\partial\Omega} = 0, \quad \nabla Y_k \cdot \mathbf{n}_{\partial\Omega} = 0, \quad \nabla z \cdot \mathbf{n}_{\partial\Omega} = 0, \quad (2.38b)$$

$$\begin{aligned} \Gamma_N : & \left(-p\mathbf{I} + \left(\frac{\mu}{Re} (\nabla \mathbf{u} + (\nabla \mathbf{u})^T) - \frac{2}{3}\mu(\nabla \cdot \mathbf{u})\mathbf{I} \right) \right) \cdot \mathbf{n}_{\partial\Omega} = 0, \\ & \nabla T \cdot \mathbf{n}_{\partial\Omega} = 0, \quad \nabla Y_k \cdot \mathbf{n}_{\partial\Omega} = 0, \quad \nabla z \cdot \mathbf{n}_{\partial\Omega} = 0, \end{aligned} \quad (2.38c)$$

$$\Gamma_{ND} : \left(-p\mathbf{I} + \left(\frac{\mu}{Re} (\nabla \mathbf{u} + (\nabla \mathbf{u})^T) - \frac{2}{3}\mu(\nabla \cdot \mathbf{u})\mathbf{I} \right) \right) \cdot \mathbf{n}_{\partial\Omega} = 0, \quad (2.38d)$$

$$T = T_D, \quad Y_k = Y_{k,D}, \quad z = z_D \quad (2.38d)$$

$$\Gamma_P : \mathbf{u}(\mathbf{x}) = \mathbf{u}(\mathbf{x}'), \quad T(\mathbf{x}) = T(\mathbf{x}'), \quad Y_k(\mathbf{x}) = Y_k(\mathbf{x}'), \quad z(\mathbf{x}) = z(\mathbf{x}'), \quad (2.38e)$$

where $k = (1, \dots, N - 1)$ denotes the index of mass fractions. The boundary Γ_D represents conditions for inlets and walls, with the velocity, temperature, mass fractions and mixture fraction defined as Dirichlet boundary conditions. Boundaries Γ_{DW} are used to represent adiabatic walls, where the velocity is given as a Dirichlet boundary condition again, but with the gradients perpendicular to the wall of the transported scalars are set to zero. The boundary Γ_N represent an outflow of the domain with homogeneous Neumann condition for all scalars. The boundary Γ_{ND} also represents an outlet boundary condition, but with Dirichlet boundary conditions for the scalars. Finally, the boundaries Γ_P are periodic, where \mathbf{x} and \mathbf{x}' are periodic pairs in the domain.



3 The Discontinuous Galerkin method

This chapter aims to give an overview of the DG method, as well as to present the spatial and temporal discretization of the equations presented earlier. Parts of this chapter are based on the works presented by Kummer (2017), Kikker et al. (2020), and Smuda (2021).

3.1 The Discontinuous Galerkin method

The spatial and temporal discretization of a scalar transport equation using the DG method is demonstrated in this section. Initially, basic definitions are provided, followed by the presentation of the general procedure for obtaining a DG discretization. The works of Cockburn et al. (2000), Hesthaven and Warburton (2008), and Di Pietro and Ern (2012) are referred to for a more in-depth description of the DG method.

3.1.1 Definitions for the discretization

First some standard definitions and notation are introduced in the context of DG methods.

Let $\Omega \subset \mathbb{R}^2$ be a computational domain with a polygonal and simply connected boundary $\partial\Omega$. The numerical grid is then formed by the set of non-overlapping elements $\mathcal{K}_h = \{K_1, \dots, K_J\}$ with a characteristic mesh size h , so that Ω is the union of all J elements, i.e. $\Omega = \bigcup_{i=1}^J K_i$.

Define $\Gamma = \bigcup_j \partial K_j$ as the union of all edges (internal edges and boundary edges) and $\Gamma_I = \Gamma \setminus \partial\Omega$ as the union of all interior edges. For each edge of Γ a normal field \mathbf{n}_Γ is defined. Particularly on $\partial\Omega$ the normal field is defined as an outer normal and $\mathbf{n}_\Gamma = \mathbf{n}_{\partial\Omega}$.

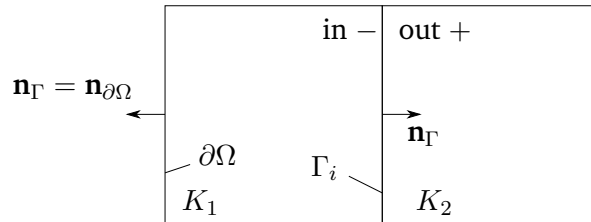


Figure 3.1: Schematic illustration of two cells. Normals of the cell K_1 are shown.

For each field $u \in C^0(\Omega \setminus \Gamma_I)$, u^- and u^+ is defined, which describe the values of the variables on the interior and exterior sides of the cell:

$$u^- = \lim_{\xi \searrow 0} u(\mathbf{x} - \xi \mathbf{n}_\Gamma) \quad \text{for } \mathbf{x} \in \Gamma \quad (3.1)$$

$$u^+ = \lim_{\xi \searrow 0} u(\mathbf{x} + \xi \mathbf{n}_\Gamma) \quad \text{for } \mathbf{x} \in \Gamma_I \quad (3.2)$$

The jump and mean values of u on the inner edges Γ_I are defined as

$$[\![u]\!] = u^+ - u^-, \quad (3.3)$$

$$\{u\} = \frac{1}{2} (u^- + u^+). \quad (3.4)$$

while the jump and mean values on the boundary edges $\partial\Omega$ are given by

$$[\![u]\!] = u^-, \quad (3.5)$$

$$\{u\} = u^-. \quad (3.6)$$

Furthermore, the broken polynomial space of a total degree k is defined as

$$\mathbb{P}_k(\mathfrak{K}_h) = \{f \in L^2(\Omega); \forall K \in \mathfrak{K}_h : f|_K \text{ is polynomial and } \deg(f|_K) \leq k\}. \quad (3.7)$$

Additionally, for $u \in \mathcal{C}^1(\Omega \setminus \Gamma)$ the broken gradient $\nabla_h u$ is defined as:

$$\nabla_h u = \begin{cases} 0 & \text{on } \Gamma \\ \nabla u & \text{elsewhere} \end{cases} \quad (3.8)$$

The broken divergence $\nabla_h \cdot u$ is defined analogously. Furthermore, the function space for test and trial functions for D_v dependent variables is defined as

$$\mathbb{V}_{\mathbf{k}} = \prod_{i=1}^{D_v} \mathbb{P}_{k_i}(\mathfrak{K}_h) \quad (3.9)$$

where $\mathbf{k} = (k_1, \dots, k_{D_v})$ is the degree vector. Additionally, for a cell K a local inner product and a local L^2 -norm is defined for $u_K, v_K \in \mathbb{V}_{\mathbf{k}}$ as

$$(u_K, v_K)_K := \int_K u_K v_K \, dx, \quad \|u_K\|_K^2 := (u_K, u_K)_K \quad (3.10)$$

Similarly, for $u_h, v_h \in \mathbb{V}_{\mathbf{k}}$ a global inner product and global broken norm are defined as

$$(u_h, v_h)_{\Omega_h} := \sum_{i=1}^N (u_h, v_h)_K, \quad \|u_h\|_{\Omega_h}^2 := (u_h, u_h)_{\Omega_h} \quad (3.11)$$

3.1.2 Discretization using the DG Method

In this subsection the DG discretization of a simple problem will be shown in order to demonstrate the method and some of its specific characteristics. For this purpose, the discretization of a general conservation law for a scalar quantity $u = u(\mathbf{x}, t)$ governed by a nonlinear flux function $\mathbf{f}(u)$ will be considered. In addition, suitable Dirichlet boundary conditions on $\partial\Omega = \partial\Omega_D$ and initial conditions u_0 are defined. The problem reads

$$\frac{\partial u}{\partial t} + \nabla \cdot \mathbf{f}(u) = 0, \quad \mathbf{x} \in \Omega, \quad (3.12a)$$

$$u = u_D, \quad \mathbf{x} \in \partial\Omega_D, \quad (3.12b)$$

$$u(\mathbf{x}, 0) = u_0(\mathbf{x}), \quad \mathbf{x} \in \Omega. \quad (3.12c)$$

The DG method allows finding an approximate solution $u_h = u_h(\mathbf{x}, t)$ for the problem defined by Equation (3.12) by forming a linear combination of polynomial functions in each cell. The discretization procedure starts by the approximation of the domain Ω with a numerical grid \mathfrak{K}_h . In each cell K_j of the numerical grid a set of polynomial basis $\phi_j = (\phi_{j,l})_{l=1,\dots,N_k} \in \mathbb{P}_k(\mathcal{K}_h)$ with a local cell support $\text{supp}(\phi_j) = \bar{K}_j$ is defined. This allows to represent the local solution for each cell K_j as

$$u_j(\mathbf{x}, t) = \sum_{l=1}^{N_k} \tilde{u}_{j,l}(t) \phi_{j,l}(\mathbf{x}) = \tilde{\mathbf{u}}_j(t) \cdot \boldsymbol{\phi}_j(\mathbf{x}) \quad (3.13)$$

The coefficients $\tilde{\mathbf{u}}_j = (\tilde{u}_{j,l})_{l=1,\dots,N_k}$ are the DOF of the local solution in the cell K_j , which are the unknowns of the problem. Note the time dependence of the coefficients $\tilde{\mathbf{u}}_j$, as well as the spatial dependence of the basis functions ϕ_j on the vector \mathbf{x} .

This approximate solution sought is the best approximation of $u \in L^2(\Omega)$, which gives a minimum global error in the approximation space $u \in \mathbb{P}_k(\Omega)$.

$$\int_{\Omega} \underbrace{(u_h(x) - u(x))^2}_{=:r(x)} dV = \|u_h - u\|_2^2 \rightarrow \min \quad (3.14)$$

Here r is the error of the discretization. Minimization is equivalent to the requirement

$$(r(x), \phi_m) = (u_h - u, \phi_m) \stackrel{!}{=} 0 \quad \forall \phi_m. \quad (3.15)$$

This means that the error is orthogonal to every polynomial function ϕ_m in the approximation space. This requirement, together with the ansatz Equation (3.13) define the projection operator π_p as

$$L^2(\Omega) \ni u \mapsto \pi_p(u) = u_h \in \mathbb{P}_p(\mathfrak{K}_h) \quad (3.16)$$

One of the major motivations for the use of high order methods stems from the so called Bramble-Hilbert lemma (Bramble and Hilbert, 1970), which states that for a p -times differentiable variable u ,

$$\|u(x) - \pi_p(u(x))\|_{L^2(\Omega)} \leq C \cdot h^{p+1} \quad (3.17)$$

where h is a characteristic cell length and C is a constant that depends on u but not on h . This means, that for a sufficiently smooth u , the approximation error is of the order $\mathcal{O}(h^{p+1})$. Note that the differentiability assumption is essential: for non smooth u the well known Gibbs phenomenon occurs. In this work a modal polynomial representation is used, using in particular Legendre polynomials. The basis functions are chosen such that they are orthogonal to each other

$$\int_{K_j} \phi_{j,m} \phi_{j,n} dV = \delta_{mn}, \quad (3.18)$$

where δ_{mn} is the Kronecker delta. This property implies that the mass matrix (to be defined later) equals the identity matrix, at least for constant density systems. This is advantageous particularly for incompressible flows, where the calculation of the mass matrix is dramatically simplified using this property.

The local formulation

By inserting the approximate solution defined by Equation (3.13) in the conservation Equation (3.12a), a local residual R_j can be defined

$$R_j(\mathbf{x}, t) = \frac{\partial u_j}{\partial t} + \nabla \cdot \mathbf{f}(u_j), \quad \mathbf{x} \in K_j \quad (3.19)$$

Minimization of this local residual is done by multiplying Equation (3.19) by the so called test functions $\vartheta_{j,l}$. In the Galerkin approach, these test functions are required to be from the same space as the trial functions, i.e. $\vartheta_{j,l} = \phi_{j,l}$. Thus, by multiplying Equation (3.19) by a trial function and integrating over the cell K_j , one obtains

$$\int_{K_j} R_j \phi_{j,l} \, dV = \int_{K_j} \underbrace{\frac{\partial u_j}{\partial t} \phi_{j,l}}_{\text{Temporal}} + \underbrace{\nabla \cdot \mathbf{f}(u_j) \phi_{j,l}}_{\text{Spatial}} \, dV \stackrel{!}{=} 0, \quad \forall \phi_{j,l}. \quad (3.20)$$

Where the minimization comes from requiring the equality to zero. Note that until this point only a cell-local discretization has been addressed. The next step for obtaining a global DG formulation is to use integration by parts for rewriting the spatial term in Equation (3.20). This is done to make the boundary edge integrals explicitly appear in the formulation, which are used to couple cell K_j with neighbouring cells. The partial integration process results in

$$\int_{K_j} \frac{\partial u_j}{\partial t} \phi_{j,l} \, dV + \oint_{\partial K_j} (\mathbf{f}(u_j) \cdot \mathbf{n}_j) \phi_{j,l} \, dS - \int_{K_j} \mathbf{f}(u_j) \cdot \nabla_h \phi_{j,l} \, dV = 0, \quad \forall \phi_{j,l}, \quad (3.21)$$

Note that inserting the ansatz Equation (3.13) into Equation (3.21) is problematic, since ∂K_j is shared by other cells, and in the DG method, continuity of a variable is not enforced across cell boundaries. This means that in general the inner value u_j^- and the outer value u_j^+ are not equal. This problem is solved by introducing the concept of a numerical flux function, denoted here with \hat{f} , which follows

$$\hat{f}(u_j^+, u_j^-, \mathbf{n}_\Gamma) \approx \mathbf{f}(u_j) \cdot \mathbf{n}_j. \quad (3.22)$$

This expression defines an unique value for the flux of a given cell boundary, enforcing flux continuity. The numerical flux \hat{f} couples the DOFs of neighbouring cells, and should satisfy certain mathematical and physical properties which will be discussed later. Many different numerical fluxes have been developed, and it is an active area of investigation. They differ mainly in computational cost, stability and dissipation of the scheme.

Finally by introducing the numerical flux in Equation (3.21) the problem now reads

$$\int_{K_j} \frac{\partial u_j}{\partial t} \phi_{j,l} \, dV + \oint_{\partial K_j} \left(\hat{f}(u_j^+, u_j^-, \mathbf{n}_\Gamma) \right) \phi_{j,l} \, dS - \int_{K_j} \mathbf{f}(u_j) \cdot \nabla_h \phi_{j,l} \, dV = 0, \quad \forall \phi_{j,l}, \quad (3.23)$$

The global formulation

Note that Equation (3.23) is still a local formulation. A global solution $u(\mathbf{x}, t)$ can be defined by a piecewise polynomial approximation according to

$$u(\mathbf{x}, t) \approx u_h(\mathbf{x}, t) = \bigoplus_{j=1}^J u_j(\mathbf{x}, t) = \sum_{j=1}^J \sum_{l=1}^{N_k} \tilde{u}_{j,l}(t) \phi_{j,l}(\mathbf{x}) \in \mathbb{P}_k(\mathfrak{K}_h) \quad (3.24)$$

which corresponds to the direct sum of the J local solutions u_j . A vector $\tilde{\mathbf{u}} = \tilde{u}_{1,1}, \tilde{u}_{1,2}, \dots, \tilde{u}_{j,l}, \dots, \tilde{u}_{J,N_k}$ which comprises all the DOFs of the global approximation u_h is defined, and is of length $N = J \cdot N_k$.

Finally, the global formulation is obtained by inserting the ansatz (Equation (3.13)) into Equation (3.23), summing over all cells K_j and making use of Equation (3.24). The problem reads: Find $u_h \in \mathbb{P}_k(\mathfrak{K}_h)$, such that $\forall \phi \in \mathbb{P}_k(\mathfrak{K}_h)$

$$\int_{\Omega} \frac{\partial u_h}{\partial t} \phi \, dV + \oint_{\Gamma} \hat{f}(u_h^+, u_h^-, \mathbf{n}_{\Gamma}) [\phi] \, dS - \int_{\Omega} \mathbf{f}(u_h) \cdot \nabla_h \phi \, dV = 0, \quad (3.25)$$

The solution of this system requires finding the DOFs $\tilde{\mathbf{u}}$ of the global approximation u_h . Dirichlet boundary conditions are included in the formulation by defining at Γ_D the outer value $u_h^- = u_D$.

Note that Equation (3.25) is semi-discrete, meaning that the system of equations has been discretized in space, but not in time. Time discretization will be treated in Section 3.1.3.

Finally, after selecting suitable numerical fluxes for the various terms of the governing equations, a system is obtained that in general has the form

$$\mathbf{M} \frac{d\tilde{\mathbf{u}}}{dt} + \mathbf{Op}(\tilde{\mathbf{u}}) = \mathbf{b}, \quad (3.26)$$

Where \mathbf{M} is the mass matrix, and \mathbf{Op} is the operator matrix. The vector \mathbf{b} contains the Dirichlet boundary condition. The operator matrix is defined locally by

$$(\mathbf{Op}_j)_{m,n} = \oint_{\partial K_j} \hat{f}(\tilde{u}_{j,n}, \tilde{u}_{j^*,n}, \mathbf{n}_{\mathfrak{J}}) \phi_{j,m} \, dS - \int_{K_j} \mathbf{f}(\tilde{u}_{j,n} \phi_{j,n}) \cdot \nabla_h \phi_{j,m} \, dV, \quad (3.27)$$

with j^* denoting the index of a neighbour cell. The matrix \mathbf{Op} has block-diagonal structure, but also including extra diagonals which relate the DOFs of the cell with the neighbouring cells.

The global mass matrix is

$$\mathbf{M} = \begin{bmatrix} \mathbf{M}_1 & 0 & \cdots & 0 \\ 0 & \mathbf{M}_2 & \cdots & 0 \\ \vdots & \vdots & \ddots & \vdots \\ 0 & 0 & \cdots & \mathbf{M}_J \end{bmatrix}, \quad (3.28)$$

which is block-diagonal, since \mathbf{M}_j does not depend on neighbouring cells.

$$(\mathbf{M}_j)_{m,n} = \int_{K_j} \phi_{j,m} \phi_{j,n} \, dV \quad (3.29)$$

The mass matrix of a cell $\mathbf{M}_j := \underline{\underline{\mathbf{M}}}_{(j,-)(j,-)}$ only depends in this case on the cell-local basis functions. Note also that for an orthonormal basis, $\mathbf{M} = \mathbf{I}$, i.e. the identity matrix.

It is interesting to note regarding the DG discretization, that a FVM-type discretization can be recovered if the basis functions in this formulation are restricted to zero-degree polynomials. Similarly, a discretization similar to a FEM formulation would be obtained if the allowance of discontinuities in the formulation of the DG method would have been ignored.

Note on the numerical fluxes

As mentioned before, the numerical fluxes \hat{f} have to fulfil certain physical and mathematical properties for obtaining a stable and convergent method. A proof for the stability of the numerical flux is given in Di Pietro and Ern (2012). One of the requirement for proving the stability is the Lipschitz continuity, meaning

$$\exists C_a \in \mathbb{R} : \left| \hat{f}(a_1, b, \mathbf{n}) - \hat{f}(a_2, b, \mathbf{n}) \right| \leq C_a |a_1 - a_2| \quad \forall a_1, a_2 \in \mathbb{R} \quad (3.30)$$

and

$$\exists C_b \in \mathbb{R} : \left| \hat{f}(a, b_1, \mathbf{n}) - \hat{f}(a, b_2, \mathbf{n}) \right| \leq C_b |b_1 - b_2| \quad \forall b_1, b_2 \in \mathbb{R} \quad (3.31)$$

Additionally, the proof of the stability requires is the monotonicity of the flux:

$$\frac{\partial \hat{f}(a, b, \mathbf{n})}{\partial a} \geq 0 \quad \wedge \quad \frac{\partial \hat{f}(a, b, \mathbf{n})}{\partial b} \leq 0 \quad \forall a, b, \mathbf{n} \quad (3.32)$$

Two more requirements are needed for the numerical flux. The first is its consistency, which can be written as

$$\hat{f}(a, a, \mathbf{n}) = \mathbf{f}(a) \cdot \mathbf{n}, \quad \forall a \in \mathbb{R}. \quad (3.33)$$

imposing that a numerical flux function should deliver the same approximate solution as the original flux function in case of a continuous variable across the interface. A direct consequence of the consistency of the numerical flux is that the weak formulation Equation (3.25) is automatically fulfilled by $u_h = u$.

Finally the last requirement is that the numerical flux should be conservative, which means that the total amount of u can only change due to fluxes across the domain boundary. This can be written as

$$\hat{f}(a, b, \mathbf{n}) = -\hat{f}(b, a, -\mathbf{n}), \quad \forall a, b \in \mathbb{R}. \quad (3.34)$$

All numerical fluxes used in this work for the spatial discretization of equations (2.22) fulfil these requirements.

3.1.3 Temporal discretization

This section gives a brief introduction to the most used time-stepping techniques and then show the time-stepping method used in this work. It is mainly based on LeVeque (2002) and Ferziger and Perić (2002).

In the previous section the spatial discretization of a transport equation using a DG method was shown, resulting in the semi-discrete formulation given by Equation (3.25). The time discretization of this semi-discrete system leads to the so called method of lines, which is the name for a method first discretized in space, and later in time.

An alternative to the method of lines is the so called Rothe's method, where time is first discretized then the space. This can be advantageous in some cases, such as problems with a moving domain. Another alternative is the space-time approach, where basically the temporal coordinate is treated as another spatial dimension. Again, the method can be very attractive for some cases. However, the discretized schemes lead often to prohibitively large systems. These approaches are ignored in the present work, and the method of lines is adopted.

First the time discretization for a system with a constant mass matrix will be discussed. The process of discretization results often in a system of ordinary differential equation (ODE) of the form

$$\mathbf{M} \frac{d\mathbf{u}}{dt} = -\mathbf{F}(t, \mathbf{u}(t)) \quad \text{for } t \in (0, T). \quad (3.35)$$

with a initial condition given by $\mathbf{u}(t = 0) = \mathbf{u}^0$. The main idea of a time-stepping algorithm is to discretize the time coordinate, and advance gradually the solution $\mathbf{u}(t^n)$ in time using the information at previous time levels $\mathbf{u}(t^{n-1}), \mathbf{u}(t^{n-2}), \dots$, until a certain final time $t = T$ is reached. By integrating Equation (3.35) in time, one obtains

$$\mathbf{M}(\mathbf{u}(t^{n+1}) - \mathbf{u}(t^n)) = - \int_{t^n}^{t^{n+1}} \mathbf{F}(t, \mathbf{u}(t)) dt \quad (3.36)$$

This equation is the starting point for different class of time stepping techniques. Two kind of methods can be distinguished, depending on how the integral in Equation (3.36) is evaluated: explicit methods and implicit methods. Explicit methods are obtained when the approximation of the integral is done only by using information from old time steps, while for implicit methods the information from the actual timestep is also considered, necessitating to solve a system of equations.

The simplest example of an explicit time-stepping method is the Explicit Euler Method:

$$\mathbf{M}\mathbf{u}(t^{n+1}) = \mathbf{M}\mathbf{u}(t^n) - \Delta t \mathbf{F}(t^n, \mathbf{u}(t^n)), \quad (3.37)$$

which is first order accurate in time. Other explicit methods exists with better properties than the Explicit Euler Method, typically using information from multiple known time levels or a interpolation of them. Adams-Bashforth methods are an example of them.

Due to the local nature of the approach, explicit methods present themselves specially attractive for DG methods, particularly for hyperbolic equations. Explicit methods are relatively easy to implement, and need considerably less storage compared to implicit methods. However, explicit methods experience the disadvantage that the stability of the algorithm is heavily limited by a maximal timestep size Δt . The timestep typically scales with the grid size h and polynomial degree k by $\Delta \sim h/k$ for hyperbolic and $\Delta \sim (h/k)^2$ for parabolic problems (Gassner et al., 2007). For many problems of interest, particularly stiff systems, this limitation is highly restrictive, since very little timesteps need to be chosen in order to obtain a stable method.

Implicit methods on the other hand are specially well suited for stiff problems, as they don't suffer from the restrictive timestep limitation of explicit methods, even not being restricted at all under certain conditions. This allows using considerably bigger timesteps, potentially reducing drastically calculation times. Implicit methods present however the inconvenience that they require the solution of a system of equations, which for large problems is not a trivial task and specialized methods are needed. The use of implicit methods is justified, particularly for stiff problems, as the extra computational overhead originating from solving of the system of equations is usually smaller than the time it would take to solve the same problem using explicit schemes with very small timesteps.

The simplest implicit method is the Implicit Euler Method,

$$\mathbf{M}\mathbf{u}(t^{n+1}) + \Delta t \mathbf{F}(t^{n+1}, \mathbf{u}(t^{n+1})) = \mathbf{M}\mathbf{u}(t^n). \quad (3.38)$$

Note that this is a nonlinear system of algebraic equations that has to be solved for $\mathbf{u}(t^{n+1})$. The Implicit Euler Methods is the first method of a family of backward differentiation formula

(BDF) methods, and under some conditions presents the property of being unconditionally stable, meaning that the algorithm allows an arbitrarily large timestep. This property allows the calculation of steady state solutions just by choosing a very large Δt value. However, not all BDF schemes are unconditionally stable, as it will be shown next.

Backward Differentiation Formula

s	γ	β_0	β_1	β_2	β_3	β_4
Implicit Euler (BDF1)	1	1	-1			
BDF2	2	3	-4	1		
BDF3	6	11	-18	9	-2	
BDF4	12	25	-48	36	-16	3

Table 3.1: Coefficients of the BDF schemes.

In the present work BDF methods are used. The main characteristic of this family of methods is that they are linear multistep methods, which means that they use information available from previous timesteps, increasing the accuracy of the scheme. In case of a non-constant mass matrix \mathbf{M} , they have a general formula given by

$$\frac{\beta_0}{\gamma \Delta t} \mathbf{M}(\mathbf{u}(t^n)) \mathbf{u}(t^n) - \mathbf{F}(\mathbf{u}(t^n)) = - \sum_{i=1}^s \frac{\beta_i}{\gamma \Delta t} \mathbf{M}(\mathbf{u}(t^{n-i})) \mathbf{u}(t^{n-i}). \quad (3.39)$$

where s is the order of the BDF-scheme. The coefficients of each schema are shown in Table 3.1. The main advantage of BDF methods is their large stability regions, which make them suitable for solving stiff problems. In Figure 3.2 the stability regions for the first four BDF schemes are shown. It is possible to observe that only the BDF-1 (implicit Euler) and BDF-2 schemes exhibit the property that they are A-stable, which means that the stability region contains the entire left complex plane (Dahlquist, 1963). On the other hand, BDF schemes of order $s > 2$ are not A-stable. In this work however, BDF schemes up to order three have been used, as the unstable eigenvalues for $s = 3$ are comparatively small (Smuda, 2021).

Temporal discretization of the low-Mach equations

Performing the same procedure as explained in the previous section for the low-Mach equations (Equations (2.22a) to (2.22d)), a semi-discrete formulation of the form

$$\frac{\partial}{\partial t} \left(\underbrace{\begin{bmatrix} \rho(T, \mathbf{Y}) & 0 & 0 & 0 \\ 0 & 0 & 0 & 0 \\ 0 & 0 & \rho(T, \mathbf{Y}) & 0 \\ 0 & 0 & 0 & \rho(T, \mathbf{Y}) \end{bmatrix}}_{\mathbf{M}(\mathbf{U})} \begin{bmatrix} \mathbf{u} \\ p \\ T \\ \mathbf{Y}' \end{bmatrix} \right) + \underbrace{\left[\mathbf{Op} \begin{pmatrix} \mathbf{u} \\ p \\ T \\ \mathbf{Y}' \end{pmatrix} + \begin{pmatrix} 0 \\ \partial_t \rho(T, \mathbf{Y}) \\ 0 \\ 0 \end{pmatrix} \right]}_{\mathbf{F}(\mathbf{U})} = 0 \quad (3.40)$$

is obtained. Here the spatial operator is denoted as \mathbf{Op} . Equation (3.40) has exactly the form that can be solved with a BDF formula as expressed by Equation (3.39). Note that the time derivative $\partial \rho / \partial t$ from the continuity equation is written as an additional source term, since the

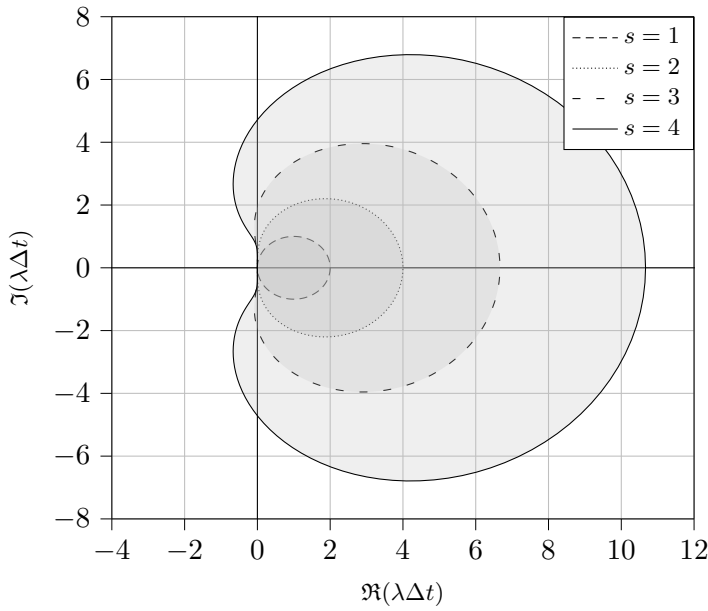


Figure 3.2: A-stability regions of the BDF schemes for different s . The areas shown in grey are unstable regions. Figure taken and adapted from (Kikker, 2020)

density is not a primitive variable. A second-order approximation of the density time derivative is used for its discretization

$$\left(\frac{\partial \rho}{\partial t} \right)^n = \frac{1}{2\Delta t} (3\rho^n - 2\rho^{n-1} + \rho^{n-2}) \quad (3.41)$$

While this type of discretization works for a wide range of applications, as it will be seen later, it can lead to instabilities in systems where density variations are large.

3.2 Discontinuous Galerkin discretization of the low-Mach equations

The discretization methodology shown in last section is used for finding a discrete formulation of the governing equations for low-Mach reactive flows. In the next sections the discretization for the fully coupled problem with finite reaction rate, and for the flame sheet problem are shown. The chosen numerical fluxes are also shown, and some of their particularities are discussed.

Special care has to be taken to avoid spurious oscillations on the pressure field. This is done in the present work by using a mixed order formulation, where polynomials of order k for velocity, temperature, mass fractions and mixture fractions, and of degree $k' = k - 1$ for pressure are used. This is a required compatibility condition for obtaining a well posed problem and is used to ensure the validity of the Ladyzenskaja-Babuška-Brezzi (or inf-sup) condition (Babuška, 1973).

3.2.1 Discontinuous Galerkin discretization of the finite reaction rate problem

Here the DG discretization of the finite reaction system defined by Equations (2.22a) to (2.22d) is presented. First, the vector $\mathbf{Y}' = (Y_1, \dots, Y_{N-1})$ is defined as the vector containing the first

$(N - 1)$ mass fractions and $\mathbf{s} = (s_1, \dots, s_{N-1})$ as the vector containing the test functions for the first $(N - 1)$ mass fraction equations.

The discretized form of Equations (2.22a) to (2.22d) is obtained in a similar fashion to the methodology shown in Section 3.1.2. This means, (1) each equation is multiplied by a test function, (2) integrated over an element K_j , (3) applied integration by parts, (4) introduced an adequate numerical flux for each term and (5) summing over all cells in order to obtain a global formulation.

The discretized equations of the transient problem can be written as: find the numerical solution $(p_h^{n+1}, \mathbf{u}_h^{n+1}, T_h^{n+1}, \mathbf{Y}_h^{n+1}) \in \mathbb{V}_k$ such that for all test functions $(q_h, \mathbf{v}_h, r_h, \mathbf{s}_h) \in \mathbb{V}_k$, following equations are fulfilled:

Continuity equation

$$\mathcal{B}^1(q_h) = \mathcal{C}(\mathbf{u}_h^{n+1}, q_h, \rho(T_h^{n+1}, \mathbf{Y}_h^{n+1})) + \mathcal{T}(\partial_t \rho|_{t^{n+1}}, q_h), \quad (3.42a)$$

Momentum equations

$$\begin{aligned} \mathcal{B}^2(\mathbf{v}_h) = & \mathcal{U}^C(\mathbf{u}_h^{n+1}, \mathbf{u}_h^{n+1}, \mathbf{v}_h, \rho(T_h^{n+1}, \mathbf{Y}_h^{n+1})) + \mathcal{U}^P(p_h^{n+1}, \mathbf{v}_h) + \mathcal{U}^D(\mathbf{u}_h^{n+1}, \mathbf{v}_h, \mu(T_h^{n+1})) \\ & + \mathcal{U}^S(\rho(T_h^{n+1}, \mathbf{Y}_h^{n+1}), \mathbf{v}_h) + \mathcal{E}(\partial_t(\rho \mathbf{u})|_{t^{n+1}}, \mathbf{v}_h), \end{aligned} \quad (3.42b)$$

Energy equation

$$\begin{aligned} \mathcal{B}^3(r_h) = & \mathcal{S}^C(\mathbf{u}_h^{n+1}, T_h^{n+1}, r_h, \rho(T_h^{n+1}, \mathbf{Y}_h^{n+1})) + \mathcal{S}^{D,E}(T_h^{n+1}, r_h, k/c_p(T_h^{n+1})) \\ & + \mathcal{S}^S(r_h, Q(T_h^{n+1}, \mathbf{Y}_h^{n+1}), \omega(T_h^{n+1}, \mathbf{Y}_h^{n+1}), c_p(T_h^{n+1}, \mathbf{Y}_h^{n+1})) \\ & + \mathcal{T}(\partial_t(\rho T)|_{t^{n+1}}, r_h), \end{aligned} \quad (3.42c)$$

Mass fraction of species α equation

$$\begin{aligned} \mathcal{B}^4(s_{\alpha h}) = & \mathcal{S}^C(\mathbf{u}_h^{n+1}, Y_{\alpha h}^{n+1}, s_{\alpha h}, \rho(T_h^{n+1}, \mathbf{Y}_h^{n+1})) + \mathcal{S}^{D,M}(Y_{\alpha h}^{n+1}, s_{\alpha h}, \rho D_\alpha(T_h^{n+1})) \\ & + \mathcal{M}_\alpha^S(s_{\alpha h}, \omega(T_h^{n+1}, \mathbf{Y}_h^{n+1})) + \mathcal{T}(\partial_t(\rho Y_{\alpha,h})|_{t^{n+1}}, s_h). \end{aligned} \quad (3.42d)$$

where the index α of the mass fraction equations takes values $\alpha = 1, \dots, (N - 1)$. Here \mathcal{C} is the discretized divergence form of the continuity equation. Furthermore \mathcal{U}^C is the discretized convective form of the momentum equation and \mathcal{S}^C is the discretized convective form of the temperature and mass fraction equations. \mathcal{U}^P is the discretized gradient form. Additionally, \mathcal{U}^D , $\mathcal{S}^{D,E}$ and $\mathcal{S}^{D,M}$ are the discretized diffusive form of the momentum, temperature and mass fractions equations, respectively. Furthermore \mathcal{U}^S , \mathcal{S}^S and \mathcal{M}^S are the discretized source terms of the momentum, temperature and mass fraction equations. Finally \mathcal{T} and \mathcal{E} are the contributions of the temporal derivatives, and \mathcal{B}^1 , \mathcal{B}^2 , \mathcal{B}^3 and \mathcal{B}^4 contain the information of the Dirichlet boundary conditions for the continuity, momentum, energy and mass fraction equations, respectively.

Note that the convective and diffusive terms of the temperature scalars T , mass fraction Y_α and mixture fraction z have the same form, so they share the same expression in their discretized form. Each one of the forms introduced here are defined later in Section 3.2.3.

3.2.2 Discontinuous Galerkin discretization of the flame sheet problem

The discretization the flame sheet problem given by Equations (2.31a) to (2.31c) proceeds in a analogous way.

The resulting problem reads: find the numerical solution $(p_h^{n+1}, \mathbf{u}_h^{n+1}, z_h^{n+1}) \in \mathbb{V}_k$ such that

for all test functions $(q_h, \mathbf{v}_h, r_h) \in \mathbb{V}_k$ following equations are fulfilled:

Continuity equation

$$\mathcal{B}^1(q_h) = \mathcal{C}(\mathbf{u}_h^{n+1}, q_h, \rho(z_h^{n+1})) + \mathcal{T}(\partial_t \rho|_{t^{n+1}}, q_h), \quad (3.43a)$$

Momentum equations

$$\begin{aligned} \mathcal{B}^2(\mathbf{v}_h) = & \mathcal{U}^C(\mathbf{u}_h^{n+1}, \mathbf{u}_h^{n+1}, \mathbf{v}_h, \rho(z_h^{n+1})) + \mathcal{U}^P(p_h^{n+1}, \mathbf{v}_h) + \mathcal{U}^D(\mathbf{u}_h^{n+1}, \mathbf{v}_h, \mu(z_h^{n+1})) \\ & + \mathcal{U}^S(\rho(z_h^{n+1}), \mathbf{v}_h) + \mathcal{E}(\partial_t(\rho \mathbf{u})|_{t^{n+1}}, \mathbf{v}_h), \end{aligned} \quad (3.43b)$$

Mixture fraction equation

$$\mathcal{B}^3(r_h) = \mathcal{S}^C(\mathbf{u}_h^{n+1}, z_h^{n+1}, r_h, \rho(z_h^{n+1})) + \mathcal{S}^{D,E}(z_h^{n+1}, r_h, \rho D(z_h^{n+1})) \mathcal{T}(\partial_t(\rho z)|_{t^{n+1}}, r_h). \quad (3.43c)$$

Note that density and transport parameters depend on the mixture fraction z , which indirectly modifies the temperature and mass fraction fields.

3.2.3 Definitions of nonlinear forms

In the following the nonlinear forms used in this work are shown. Regarding the choice of fluxes, the "best practices" known in literature for the incompressible Navier-Stokes equation are followed. These fluxes proved to be well suited for all the problems discussed in this thesis, providing stability to the algorithm, while maintaining the accuracy of the solver.

It is well known that central difference fluxes for the pressure gradient and velocity divergence, combined with a coercive form for the viscous terms, e.g. symmetric interior penalty, gives a stable discretization for the Stokes equation (Pietro and Ern, 2012; Girault et al., 2004). Furthermore, it is known that for all kinds of convective terms, a numerical flux which transports information in characteristic direction, e.g. Upwind, Lax-Friedrichs or Local-Lax-Friedrichs, must be used. The last one was opted for in the present implementation, as it provides a good compromise between accuracy and stability.

Continuity equation

A central difference flux for the discretization of the continuity equation is used:

$$\mathcal{C}(\mathbf{u}, q, \rho) = \oint_{\Gamma_I \cup \Gamma_N \cup \Gamma_{ND} \cup \Gamma_P} \{\rho \mathbf{u}\} \cdot \mathbf{n}_\Gamma \llbracket q \rrbracket \, dS - \int_{\Omega} \rho \mathbf{u} \cdot \nabla_h q \, dV. \quad (3.44)$$

The density in Equation (3.44) is evaluated as a function of the temperature and mass fractions using the equation of state (Equation (2.26)). The term \mathcal{B}^1 on the left hand sides of Equation (3.42a) and Equation (3.43a) contains the Dirichlet boundary conditions:

$$\mathcal{B}^1(q) = - \oint_{\Gamma_D \cup \Gamma_{DW}} q (\rho_D \mathbf{u}_D \cdot \mathbf{n}_\Gamma) \cdot dS \quad (3.45)$$

The density at the boundary ρ_D is evaluated with Equation (2.26) using the corresponding Dirichlet values of temperature and mass fractions, i.e. $\rho_D = \rho(T_D, \mathbf{Y}_D)$. Finally the temporal contribution is

$$\mathcal{T}(u, v) = \int_{\Omega} uv \, dV. \quad (3.46)$$

Note that in case of the temporal term of the continuity equation $\partial_t \rho$, it is discretized as mentioned in Equation (3.41)

Momentum equations

The convective term of the momentum equations is discretized using a Lax-Friedrichs flux

$$\mathcal{U}^C(\mathbf{w}, \mathbf{u}, \mathbf{v}, \rho) = \oint_{\Gamma} \left(\{\rho \mathbf{u} \otimes \mathbf{w}\} \mathbf{n}_{\Gamma} + \frac{\gamma_1}{2} [\![\mathbf{u}]\!] \right) \cdot [\![\mathbf{v}]\!] \, dS - \int_{\Omega} (\rho \mathbf{u} \otimes \mathbf{w}) : \nabla_h \mathbf{v} \, dV. \quad (3.47)$$

The Lax-Friedrichs parameter γ_1 is calculated as Klein et al. (2016)

$$\gamma_1 = \max \left\{ 2\overline{\rho^+} |\overline{\mathbf{u}^+} \cdot \mathbf{n}^+|, 2\overline{\rho^-} |\overline{\mathbf{u}^-} \cdot \mathbf{n}^-| \right\}, \quad (3.48)$$

where $\overline{\rho^{\pm}}$ and $\overline{\mathbf{u}^{\pm}}$ are the mean values of ρ^{\pm} and \mathbf{u}^{\pm} in K^{\pm} , respectively. The pressure term is discretized by using a central difference flux

$$\mathcal{U}^P(p, \mathbf{v}) = \oint_{\Gamma \setminus \Gamma_N \setminus \Gamma_{ND}} \{p\} ([\![\mathbf{v}]\!] \cdot \mathbf{n}_{\Gamma}) \, dS - \int_{\Omega} p \nabla_h \cdot \mathbf{v} \, dV. \quad (3.49)$$

The diffusive term of the momentum equations is discretized using a symmetric interior penalty (SIP) formulation (Shahbazi, 2005)

$$\begin{aligned} \tilde{\mathcal{U}}^D(\mathbf{u}, \mathbf{v}, \mu) &= \int_{\Omega} \left(\mu \left((\nabla_h \mathbf{u}) + (\nabla_h \mathbf{u})^T - \frac{2}{3} (\nabla_h \cdot \mathbf{u}) \mathbf{I} \right) \right) : \nabla_h \mathbf{v} \, dV \\ &\quad - \oint_{\Gamma \setminus \Gamma_N \setminus \Gamma_{ND}} \left(\left\{ \mu (\nabla_h \mathbf{u} + \nabla_h \mathbf{u}^T - \frac{2}{3} (\nabla_h \cdot \mathbf{u}) \mathbf{I}) \right\} \mathbf{n}_{\Gamma} \right) \cdot [\![\mathbf{v}]\!] \, dS \\ &\quad - \oint_{\Gamma \setminus \Gamma_N \setminus \Gamma_{ND}} \left(\left\{ \mu (\nabla_h \mathbf{v} + \nabla_h \mathbf{v}^T - \frac{2}{3} (\nabla_h \cdot \mathbf{v}) \mathbf{I}) \right\} \mathbf{n}_{\Gamma} \right) \cdot [\![\mathbf{u}]\!] \, dS \\ &\quad + \oint_{\Gamma \setminus \Gamma_N \setminus \Gamma_{ND}} \eta \mu_{\max} [\![\mathbf{u}]\!] [\![\mathbf{v}]\!] \, dS. \end{aligned} \quad (3.50)$$

The viscosity μ is evaluated as a function of temperature according to Equation (2.29) and $\mu_{\max} = \max(\mu^+, \mu^-)$. Additionally η is the penalty term of the SIP formulation, which has to be chosen big enough to ensure coercivity of the form, but also as small as possible in order to not increase the condition number of the problem. The estimation of the penalty term is based on an expression of the form

$$\eta = \eta_0 \frac{A(\partial K)}{V(K)}, \quad (3.51)$$

where for a two-dimensional problem A is the perimeter and V the area of the element. The parameter η_0 is a safety factor. If not stated otherwise, the value $\eta_0 = 4$ is set in all calculations. Further information on the determination of the penalty term of the SIP formulation η and the penalty term of the Lax-Friedrichs flux γ_1 can be found in the works from Hesthaven and Warburton (2008) and Hillewaert (2013).

Note that the diffusive term of the momentum equations is scaled by the Reynolds number, obtaining finally

$$\mathcal{U}^D(\mathbf{u}, \mathbf{v}, \mu) = \frac{1}{Re} \tilde{\mathcal{U}}^D(\mathbf{u}, \mathbf{v}, \mu) \quad (3.52)$$

The source term arising due to body forces is:

$$\mathcal{U}^S(\rho, \mathbf{v}) = \frac{1}{Fr^2} \int_{\Omega} \rho \frac{\mathbf{g}}{\|\mathbf{g}\|} \cdot \mathbf{v} \, dV. \quad (3.53)$$

Finally, the left hand sides of Equation (3.42b) and Equation (3.43b) contain the information from Dirichlet boundary conditions:

$$\mathcal{B}^2(\mathbf{v}) = - \oint_{\Gamma_D} \left((\rho \mathbf{u}_D \otimes \mathbf{u}_D) \mathbf{n}_\Gamma + \frac{\gamma_1}{2} \mathbf{u}_D \right) \cdot \mathbf{v} dS + \oint_{\Gamma_D} \mu_D \mathbf{u}_D \cdot (\nabla_h \mathbf{v} \mathbf{n}_\Gamma + \nabla_h \mathbf{v}^T \mathbf{n}_\Gamma - \eta \mathbf{v}) dS. \quad (3.54)$$

The Dirichlet viscosity value μ_D is calculated from Equation (2.29) using the Dirichlet values of the temperature at the boundary. Finally the temporal derivative of the momentum equation in its discretized form corresponds to

$$\mathcal{E}(\mathbf{u}, \mathbf{v}) = \int_{\Omega} \mathbf{u} \cdot \mathbf{v} dV. \quad (3.55)$$

Scalar equations

Since the convective and diffusive terms for the temperature, mass fractions and mixture fraction share a similar form, here their discretized expressions are summarized in terms of an arbitrary scalar X (corresponding to T in the energy equation, Y_α in the equation for species α and z for the mixture fraction equation) and transport parameter ξ (i.e. k/c_p in the energy equation, and (ρD) for the mass fraction and mixture fraction equations). The convective term of the scalars is discretized using a Lax-Friedrichs flux

$$\mathcal{S}^C(\mathbf{u}, X, r, \rho) = \oint_{\Gamma} \left(\{\rho \mathbf{u} X\} \cdot \mathbf{n} + \frac{\gamma_2}{2} [X] \right) [r] dS - \int_{\Omega} (\rho \mathbf{u} X \cdot \nabla_h r) dV. \quad (3.56)$$

The Lax-Friedrichs parameter γ_2 is calculated as

$$\gamma_2 = \max \left\{ \overline{\rho^+} |\overline{\mathbf{u}^+} \cdot \mathbf{n}^+|, \overline{\rho^-} |\overline{\mathbf{u}^-} \cdot \mathbf{n}^-| \right\}. \quad (3.57)$$

The diffusion term of scalars is discretized again with a SIP formulation:

$$\begin{aligned} \mathcal{S}^D(X, r, \xi) &= \int_{\Omega} (\xi \nabla_h X \cdot \nabla_h r) dV \\ &- \oint_{\Gamma \setminus \Gamma_N \setminus \Gamma_{ND}} (\{\xi \nabla_h X\} \cdot \mathbf{n} [r] + \{\xi \nabla_h r\} \cdot \mathbf{n} [X] - \eta \xi_{\max} [X] [r]) dS. \end{aligned} \quad (3.58)$$

The transport parameter ξ is calculated as a function of temperature using Equation (2.29) and $\xi_{\max} = \max(\xi^+, \xi^-)$. The diffusive term for the temperature equation and mixture fraction equation is scaled by the Reynolds and Prandtl number as

$$\mathcal{S}^{D,E}(T, r, k/c_p) = \frac{1}{\text{Re} \text{Pr}} \mathcal{S}^D(T, r, k/c_p) \quad (3.59)$$

Similarly the diffusive term for the mass fraction equations is

$$\mathcal{S}^{D,M}(Y_{\alpha h}^{n+1}, s_{\alpha h}, \rho D_\alpha) = \frac{1}{\text{Re} \text{Pr} \text{Le}_\alpha} \mathcal{S}^D(Y_{\alpha h}^{n+1}, s_{\alpha h}, \rho D_\alpha) \quad (3.60)$$

The boundary condition term of the corresponding scalar equation is:

$$\mathcal{B}^3(r) = - \oint_{\Gamma_D \cup \Gamma_{ND}} \left((\rho_D \mathbf{u}_D X_D) \cdot \mathbf{n}_\Gamma + \frac{\gamma_2}{2} X_D \right) r dS + \oint_{\Gamma_D \cup \Gamma_{ND}} \xi_D X_D (\nabla_h r \cdot \mathbf{n}_\Gamma - \eta r) dS. \quad (3.61)$$

Here, X_D is the Dirichlet value of the scalar X on boundaries and ξ_D is the corresponding transport parameter, which is calculated with Equation (2.29) using the Dirichlet values of the temperature at the boundary. Finally, the volumetric source terms of the energy and mass fraction equations are defined as follows:

$$\mathcal{S}^S(r, Q, \omega, c_p) = H Da \int_{\Omega} \frac{Q\omega}{c_p} r dV, \quad (3.62)$$

$$\mathcal{M}_{\alpha}^S(s_{\alpha}, \omega) = Da \int_{\Omega} \nu_{\alpha} M_{\alpha} \omega s_{\alpha} dV. \quad (3.63)$$

The heat release Q is calculated with Equation (2.25), the reaction rate ω is evaluated using Equation (2.24) and the mixture heat capacity with Equation (2.28).

4 Computational methodology

This chapter addresses the computational methods developed for solving the system of governing equations presented in the preceding chapters. The chapter starts in Section 4.1 with a concise literature review concerning the methods employed in this study. Subsequently, in Section 4.2 a comprehensive description of the methods employed by the XSEC solver is provided. Then in Section 4.3 the implementation and uses of both nonlinear and linear solvers are presented. Finally, in Section 4.4 various convergence-enhancing strategies employed for solving highly nonlinear problems are presented, such as the use of a homotopy strategy for highly non-linear problems, or the use of solver safeguards to avoid nonphysical results.

4.1 State of the art of DG methods for diffusion flame simulations

There are numerous works in which the DG method has been used in the context of CFD. Extensive attention has been paid to algorithms for solving incompressible flows, such as in the works from Shahbazi et al. (2007), Kummer (2012), and Klein et al. (2013). However, not much attention has been put into extending the methods to be able to handle variable density flows. In the work by Klein et al. (2016) an extension is presented of the method for solving the low-Mach equations in a DG Framework making use of a SIMPLE type scheme. As mentioned in the introduction, while the strategy proved useful for simulating various flow problems, for many of these problems the computation time proved to be prohibitive. Similarly, in the work of Hennink et al. (2021) a pressure-based solver for low-Mach flows is presented. They solve the system of equations in a segregated way, and solve for the mass flux instead of the velocity as the primitive variable. They employ an equal order formulation for the coupling of pressure and velocity; however, this approach results in significant computational expenses, especially when dealing with high Reynolds numbers. They solve the enthalpy form of the energy equations, which is shown to be a source of instabilities if special care is not taken.

In the context of CFD, the coupling between velocity fields and pressure within the Navier-Stokes equations has been a topic of considerable research and interest. It's a well known fact that in the case of incompressible flows, the absence of a time derivative in the continuity equation poses challenges for advancing the system in time using conventional methods. Traditionally this type of coupling has been solved by means of segregated methods, such as projection methods (Chorin, 1967), or by using methods such as SIMPLE (Patankar, 1980). Such algorithms offer the benefit of low memory usage and have undergone extensive investigation and application especially within the context of approaches like FVM. However, as mentioned earlier, the use of segregated methods doesn't guarantee conservativity of the relevant physical quantities, and special care has to be taken in that regard. Since for low-Mach number flows the flow field is coupled to the temperature and therefore to the density, it is not possible to solve the equations in a completely conservative way in a non-iterative segregated framework.

The investigations mentioned above deal exclusively with segregated approaches, which as mentioned, are not necessarily conservative. An alternative approach involves solving the complete system of equations in a fully coupled manner. This approach guarantees the conservation of relevant physical variables, provided careful attention is paid to the convergence criteria. While this strategy may appear to be the most straightforward, it is not free of complications. Special care must be taken in the algorithms for solving the usually nonlinear problem, as this can easily lead to problems with convergence. Memory resources can also be prohibitive, as solving the equations in a coupled manner usually requires dealing with very big matrices.

The DG method has also been used for simulations of combustion, mainly within a compressible framework. In the work from Johnson and Kercher (2020) the compressible Navier–Stokes equations are solved using a nodal DG scheme for combustion with complex chemistry and transport parameters. An hp-adaptive method is also presented. Similarly in the work from Lv and Ihme (2017) a DG solver for multi-component chemically reacting flows, which solves the fully compressible Navier-Stokes equation, is presented. A hybrid-flux formulation is used, where a conservative Riemann solver is used for shock treatment, and a double-flux formulation is used in smooth regions. They show its applicability for non-reacting and reacting flows, particularly for systems characterized by high-Mach numbers. To the best of the authors' knowledge, there are no publications that address low-Mach number reactive flows using a fully coupled solver, as done in the present work.

The system of equations obtained from the discretization of highly nonlinear systems can be very difficult to solve. Fixed-point iteration schemes have been used often used as a linearization strategy, as done by Klein et al. (2016). A significant limitation of this strategy is the necessity for an adequate selection of the under-relaxation factors, which are highly dependent on the specific problem. A much more robust strategy is the use of Newton type methods. Here, a problem-dependent factor is not needed. There is however a trade-off, because the Jacobian matrix has to be calculated, which can be computationally expensive. This approach has been used for combustion related problems in numerous works. Karaa et al. (2003) studied the axisymmetric laminar jet diffusion flame and investigated the behavior of a multi-grid solver when using different pre-conditioners with a damped Newton algorithm. Shen et al. (2006) investigated the use and efficiency of a Newton method coupled with the Bi-CGSTAB method for an axisymmetric laminar jet flame. They concluded that, in terms of computational cost, the steady-state solution is more efficiently obtained by directly solving the steady formulation of the equations, than by solving the transient Navier-Stokes equations until the steady state is reached.

4.2 The XNSEC solver

The XNSEC solver is mainly focused on the simulation of combustion using the low-Mach equations. The equations are solved in a fully coupled way, and the associated nonlinear problem is solved by means of a globalized Newton method. Motivated by future work, where a burning droplet is going to be simulated, the solver is embedded in the framework for eXtended Discontinuous Galerkin (XDG) solvers presented in Kummer (2017), which focuses on applications for multi-phase flows using a sharp interface approach employing a level-set method. However, in the present work only the single-phase case is treated.

The fully coupled solution of the equations is realized by means of various algorithmic components

- The solution of the flame-sheet problem for initialization of a fully coupled steady-state finite-reaction rate system. The strategy is presented in Section 4.4.3
- A timestepping framework based on a BDF scheme, described in Kummer et al. (2018).
- A homotopy continuation scheme that allows solving highly nonlinear problems by generating a series of convergent solutions. This algorithm is described in Section 4.4.1.
- A Newton-Dogleg method for the solution of nonlinear problems. The Dogleg globalization increases the likelihood of finding a convergent solution even in cases where no adequate initial estimate is available. An increased computational efficiency is archived by an special method for the calculation of the Jacobian matrix. The algorithm is described in Section 4.3.3

Note that even for steady state calculations, a time stepping scheme is used and the steady-state solutions are obtained by using a Implicit Euler time stepping scheme. Since the scheme is unconditionally stable (see Section 3.1.3), it is possible to select a very large timestep to obtain the steady state solution. In particular, a value $\Delta t = 1.7976931348623157 \cdot 10^{304}$ is used, which is four orders of magnitude lower than the largest possible value of a double-precision floating-point number.

4.3 Solution of the nonlinear problem

In the early stages of development of the XNSEC solver, the BoSSS code featured a framework for the solution of nonlinear systems using Picard iterations. These proved to be useful for systems where no large nonlinearities exist. Although the use of Picard iterations was useful for solving various types of problems (particularly problems involving incompressible flows), the method did not prove to be a particularly robust method, since it requires user-defined under-relaxation parameters in order to obtain a stable algorithm. This motivated the development of the implementation of a Newton method for the resolution of the nonlinear system which will be presented in the following pages. The use of this globalized Newton method proved to be very successful for all testcases treated in the present work.

The variational problem defined by Equations (3.42a) to (3.42d) can be cast into a more compact notation. By subtracting all terms from the right-hand sides from the terms of the left-hand sides of Equations (3.42a) to (3.42d) the problem can be written as: Find $\mathbf{U}_h \in \mathbb{V}_k$

$$\mathcal{N}(\mathbf{U}_h, \mathbf{V}_h) = 0 \quad \forall \mathbf{V}_h \in \mathbb{V}_k, \quad (4.1)$$

for $\mathbf{U}_h = (p_h, \mathbf{u}_h, T_h, \mathbf{Y}'_h)$ and $\mathbf{V}_h = (q_h, \mathbf{v}_h, r_h, \mathbf{s}_h)$. A basis is assumed as $\underline{\Phi} = (\Phi_1, \dots, \Phi_L)$ of \mathbb{V}_k , written as a row vector, with $L := \dim(\mathbb{V}_k)$. Then \mathbf{U}_h can be represented as $\mathbf{U}_h = \underline{\Phi} \cdot \mathbf{U}$. The nonlinear problem (4.1) can then be expressed as

$$\mathcal{A}(\mathbf{U}) = 0, \quad (4.2)$$

with the nonlinear function $\mathbb{R}^L \ni \mathbf{U} \mapsto \mathcal{A}(\mathbf{U}) \in \mathbb{R}^L$. The i -th component of $\mathcal{A}(\mathbf{U})$, can be defined by $\mathcal{N}(-, -)$ through the relation $[\mathcal{A}(\mathbf{U})]_i = \mathcal{N}(\underline{\Phi} \cdot \mathbf{U}, \Phi_i)$.

4.3.1 Newton's method

Newton's method is a very popular and well known iterative method used for finding roots of nonlinear systems. The method is particularly attractive because shows the property of having quadratic convergence sufficiently close to the solution (Deuflhard, 2011). In this section the method will be briefly described. For more information the interested reader is referred to the textbook from Kelley (1995).

Consider the linearization of Equation (4.2) around \mathbf{U}_n ,

$$\mathcal{A}(\mathbf{U}_n) + \partial\mathcal{A}(\mathbf{U}_n) \underbrace{(\mathbf{U}_{n+1} - \mathbf{U}_n)}_{=: \mathbf{s}'_n} = 0. \quad (4.3)$$

Here is $\partial\mathcal{A}$ the Jacobian matrix of \mathcal{A} , defined as

$$\partial\mathcal{A}_{ij}(\mathbf{U}) := \frac{\partial\mathcal{A}_i}{\partial U_j}(\mathbf{U}). \quad (4.4)$$

By repeatedly solving Equation (4.3) one obtains a standard Newton scheme for Equation (4.2), yielding a sequence of approximate solutions $\mathbf{U}_0, \mathbf{U}_1, \mathbf{U}_2, \dots$ obtained from an initial guess \mathbf{U}_0 through the iteration scheme $\mathbf{U}_{n+1} = \mathbf{U}_n + \mathbf{s}'_n$. In the classical undamped Newton method, the correction step \mathbf{s}'_n is set to be the whole Newton-step, i.e $\mathbf{s}'_n = \mathbf{s}_n$ with

$$\mathbf{s}_n := -\partial\mathcal{A}(\mathbf{U}_n)^{-1}\mathcal{A}(\mathbf{U}_n), \quad (4.5)$$

which is computed using a direct solver. Unfortunately, convergence of the Newton method for any starting value \mathbf{U}_0 is not guaranteed. As a way to remedy this problem, so-called globalization methods have been developed, where basically the area of convergence of the Newton algorithm is enlarged used different kind of strategies.

A big drawback of Newton method is the calculation is the necessity of the Jacobian matrix, since its direct calculation using usual methods can be computationally expensive. The BoSSS framework provides an efficient algorithm for the evaluation of the Jacobian, and is presented next.

4.3.2 Calculation of the Jacobian matrix

During the development process of the XNSEC solver different strategies for the calculation of the Jacobian matrix $\partial\mathcal{A}$ were developed and are shown here.

First, it is interesting to show the relationship existing between two well known methods for solving nonlinear systems: Picard iterations and Newton's method. Note that the nonlinear problems Equation (4.2) appearing in this work have the structure

$$\mathcal{A}(\mathbf{U}) := A(\mathbf{U})\mathbf{U} - \mathbf{b}. \quad (4.6)$$

Thus, the Jacobian matrix Equation (4.4) can be written as

$$\partial\mathcal{A}_{ij}(\mathbf{U}) = A_{ij} + \sum_k \frac{\partial A_{ik}}{\partial U_j} U_K = A_{ij} + A'_{ij} U_K. \quad (4.7)$$

Inserting Equation (4.6) and Equation (4.7) into Equation (4.3), the linear system to be solved using Newton's method can be written as

$$\underbrace{A(\mathbf{U}_n)(\mathbf{U}_n + \mathbf{s}'_n) - \mathbf{b}}_{\text{Picard system}} + A'(\mathbf{U}_n)\mathbf{U}_n \mathbf{s}'_n = 0 \quad (4.8)$$

This makes the relationship between the two algorithms apparent, and shows that by using Picard iterations some terms are being neglected from the iteration scheme. Unlike Picard's method of iterations, Newton's method requires additionally the evaluation of the Jacobi matrix, which must be approximated in some way. This section shows three strategies that were used throughout the development of this work for that purpose.

Ad-hoc linearization of the Jacobian matrix

For some problems, particularly saddle-point problems, the Jacobian A' can be approximated fairly well by simply evaluating the operator matrix. Thus, the system to be solved for Newton Iteration yields

$$A(\mathbf{U}_n)(\mathbf{U}_n + \mathbf{s}'_n) - \mathbf{b} + A(\mathbf{U}_n)\mathbf{U}_n\mathbf{s}'_n = 0 \quad (4.9)$$

This strategy offers a computationally cheap algorithm to obtain a solution of the nonlinear problem. However, the method offers limited robustness, and is known to be prone to fail for non-saddle-point problems (Kikker, 2020).

Approximation of the Jacobian matrix by finite differences

A straightforward way of calculating the Jacobian matrix appearing in Equation (4.8) is to use forward finite differences as an approximation

$$A'(\mathbf{U})_j := \frac{A(\mathbf{U} + \varepsilon \|\mathbf{U}\| \mathbf{e}_j) - A(\mathbf{U})}{\varepsilon \|\mathbf{U}\|}, \quad (4.10)$$

where \mathbf{e}_j is the unit vector with j th component equal to one, and zero in all other components. The value of ε should be chosen small, as usual when calculating finite differences, but also large enough not to disturb the calculations due to problems caused by floating-point rounding calculations. Here, value $\varepsilon = \sqrt{\text{eps}}$ is selected, where $\text{eps} = 2.22044604925031 \cdot 10^{-16}$ is the floating point accuracy for double precision.

The calculation of the forward finite difference approximation is a costly operation, especially for large systems, where it can be particularly prohibitive. However it offers a robust way to approximate the Jacobian. Strategies for improving the efficiency of this calculation exists, such as the use of analytic Jacobians, or use of the sparsity patterns of the Jacobian (Kelley, 1995). These are not treated in the present work.

Approximation of the Jacobian from differentiation of equation components

The finite difference Jacobi matrix calculation shown above is a fairly simple but computationally expensive calculation. The *BoSSS* code is capable of evaluating the Jacobian matrix automatically from the equation components given in Section 3.1.1. First, note that $\mathcal{A}(\mathbf{U})$ could be written as

$$[\mathcal{A}(\mathbf{U})]_i = \mathcal{N}(\mathbf{U}_h, \Phi_i) = \int_{\Omega_h} N_1(\mathbf{x}, \mathbf{U}_h, \nabla \mathbf{U}_h) \cdot \Phi_i + N_2(\mathbf{x}, \mathbf{U}_h, \nabla \mathbf{U}_h) \cdot \nabla \Phi_i dV + \oint_{\Gamma} \dots dS. \quad (4.11)$$

The edge integral, which is left out in Equation (4.11), can be expressed analogously to the volume integral, i.e. as a sum over four nonlinear functions, multiplied by Φ_i^+ , Φ_i^- , $\nabla \Phi_i^+$ and $\nabla \Phi_i^-$, respectively. These functions themselves may include the dependence on \mathbf{x} , \mathbf{U}_h^+ ,

\mathbf{U}_h^- , $\nabla \mathbf{U}_h^+$ and $\nabla \mathbf{U}_h^-$. These are however omitted here for the sake of compactness, but the treatment is analogue. Realizing that

$$\frac{\partial \mathbf{U}_h}{\partial \mathbf{U}_j} = \Phi_j \quad (4.12)$$

and by application of the chain rule, it is possible to derive an expression for the calculation of the entries of the Jacobian matrix from the equation components as

$$\partial \mathcal{A}_{ij}(\mathbf{U}) = \int_{\Omega_h} (\partial_{\mathbf{U}_h} N_1(\mathbf{x}, \mathbf{U}_h, \nabla \mathbf{U}_h) \Phi_j + \partial_{\nabla \mathbf{U}_h} N_1(\mathbf{x}, \mathbf{U}_h, \nabla \mathbf{U}_h) \nabla \Phi_j) \cdot \Phi_i + \dots dV + \oint_{\Gamma} \dots dS. \quad (4.13)$$

All omitted terms in Equation (4.13) can be approximated analogously to the contributions for N_1 . In the BoSSS code, derivatives $\partial_{\mathbf{U}_h} N_1(\dots)$ and $\partial_{\nabla \mathbf{U}_h} N_1(\dots)$ are approximated by a finite difference, using a perturbation by eps in the respective argument.

This approach has the significant improvement that it offers an efficient and accurate way to obtain the Jacobian matrix, unlike the two approaches mentioned above. For this reason, this option is the one chosen for the resolution of all the testcases shown in this work.

4.3.3 Newton-Dogleg Method

A well known problematic of Newton methods is the necessity of a good starting estimate for the algorithm to get a convergent solution. If the initial estimate is far away from a solution, the algorithm could converge but at a very slow rate and in the most critical cases it could stagnate or even diverge. For some highly nonlinear problems this is a significant issue. The so called globalization methods are auxiliary procedures designed to alleviate this problem.

In general two kinds of globalization algorithms can be identified. The so called backtracking methods consist in a modification of the Newton step length (usually a reduction), in order to obtain steps that lead to a solution of the system. These are usually easy to implement, but suffer from the restriction that the Newton step direction is restricted to the one of the trial step, which could not be an ideal direction, specially if the Jacobian is ill conditioned (Pawlowski et al., 2006).

The second globalization type are the so called Trust-region globalization methods. The main idea of these kind of algorithms is to use a quadratic approximation of the function, which is assumed to be valid within a "trust region". This trust region is enlarged or reduced based on defined strategies, which improves the likelihood of finding a solution and accelerates the convergence. This kind of approaches has proven to be robust and very useful for a variety of problems, but are usually not easy to implement.

In this work, in order to increase robustness when the distance between \mathbf{U}_0 and the exact solution \mathbf{U} is large, a trust region globalization approach known as the Newton-Dogleg method is used. The algorithm is presented by Pawlowski et al. (2006) and Pawlowski et al. (2008). In this section the intention is to give only the main ideas of method and refer to the original works for further details.

Note that the exact solution of Equation (4.2) is also a minimum of the functional

$$f(\mathbf{U}) := \frac{1}{2} \|\mathcal{A}(\mathbf{U})\|_2^2. \quad (4.14)$$

Thus $\nabla f(\mathbf{U}) = \partial \mathcal{A}(\mathbf{U})^T \mathcal{A}(\mathbf{U})$. For \mathbf{U}_n , the approximate Cauchy point with respect to the 2-norm, is defined as the minimizer \mathbf{g}_n of $\|\mathcal{A}(\mathbf{U}_n) + \partial \mathcal{A}(\mathbf{U}_n) \mathbf{g}_n\|_2$ in the direction of steepest decent,

i.e. $\mathbf{g}_n = \lambda \nabla f(\mathbf{U}_n)$, $\lambda \in \mathbb{R}$. Substituting $\mathbf{w} := -\partial \mathcal{A}(\mathbf{U}_n) \nabla f(\mathbf{U}_n)$, \mathbf{g}_n is given by

$$\mathbf{g}_n = \frac{\mathcal{A}(\mathbf{U}_n) \cdot \mathbf{w}}{\mathbf{w} \cdot \mathbf{w}} \nabla f(\mathbf{U}_n). \quad (4.15)$$

In contrast to the classical undamped Newton Method, where each iteration used the whole Newton-step \mathbf{s}_n (cf. Equation (4.5)) within the Newton-Dogleg method, the correction step \mathbf{s}'_n is chosen along the so-called Dogleg curve, which is the piece-wise linear curve from the origin to \mathbf{g}_n and further to \mathbf{s}_n . The selection of \mathbf{s}'_n on this curve is controlled by the trust-region diameter $\delta > 0$:

- If $\|\mathbf{s}_n\|_2 \leq \delta$, meaning that the Newton estimate lies inside the trust region, the whole Newton step is accepted and $\mathbf{s}'_n = \mathbf{s}_n$.
- If $\|\mathbf{g}_n\|_2 \leq \delta$ and $\|\mathbf{s}_n\|_2 > \delta$, i.e. the Newton guess is outside the trust region, but the Cauchy point is inside the trust region, \mathbf{s}'_n is chosen on the linear interpolation from \mathbf{g}_n to \mathbf{s}_n so that $\|\mathbf{s}'_n\|_2 = \delta$: For the ansatz $\mathbf{s}'_n = \tau \mathbf{s}_n + (1 - \tau) \mathbf{g}_n$, the interpolation factor τ is given as $\tau = (a^2 - c + \sqrt{(a^2 + b^2 - 2c)\delta^2 - a^2b^2 + c^2})/(a^2 + b^2 - 2c)$ with $a = \|\mathbf{g}_n\|_2$, $b = \|\mathbf{s}_n\|_2$ and $c = \mathbf{g}_n \cdot \mathbf{s}_n$. Thus, the new estimate is taken as point where the line connecting the Newton guess and the Cauchy point intersect the boundary of the trust region.
- If $\|\mathbf{g}_n\|_2 > \delta$, both Newton guess and Cauchy point lie outside the trust region, the new iterate is taken to be the point at the edge of the trust region from the line connecting the actual Newton guess and the Cauchy point. $\mathbf{g}_n = (\delta/\|\mathbf{g}_n\|_2) \mathbf{g}_n$.

The choice and adaptation of the trust region diameter δ throughout the Newton-Dogleg procedure follows a sophisticated heuristic. It is for the sake of completeness described here. The adaptation of the trust region diameter is based on comparing the actual residual reduction $\text{ared}_n := \|\mathcal{A}(\mathbf{U}_n)\|_2 - \|\mathcal{A}(\mathbf{U}_n + \mathbf{s}'_n)\|_2$ with the predicted residual reduction $\text{pred}_n := \|\mathcal{A}(\mathbf{U}_n)\|_2 - \|\mathcal{A}(\mathbf{U}_n) + \partial \mathcal{A}(\mathbf{U}_n) \mathbf{s}'_n\|_2$. The algorithm for the adaptation of the trust region can be resumed as

- (1) Set $n = 0$, $\delta_n = \min(10^{10}, \max(2 \cdot 10^{-6}, \|\mathbf{s}_0\|_2))$.
- (2) Compute the Newton step \mathbf{s}_n and the Cauchy point \mathbf{g}_n and find \mathbf{s}'_n on the Dogleg curve with respect to the recent δ_n .
- (3) While $\text{ared}_n \leq \text{pred}_n$ do: Update trust region diameter $\delta_n \leftarrow 0.5 \delta_n$ and re-compute \mathbf{s}'_n . If $\delta_n < 10^{-6}$ terminate abnormally and mark the computation as failed.
- (4) If the convergence criterion (see below) is fulfilled, terminate and mark the computation as success.
- (5) Perform a final update of the trust region: Set

$$\delta_{n+1} = \begin{cases} \max(10^{-6}, \|\mathbf{s}_n\|_2) & \text{if } \text{ared}_n/\text{pred}_n < 0.1 \text{ and } \|\mathbf{s}_n\|_2 \delta_n \\ \max(10^{-6}, 0.25 \cdot \delta_n) & \text{else, if } \text{ared}_n/\text{pred}_n < 0.1 \\ \min(10^{10}, 4 \cdot \delta_n) & \text{else, if } \text{ared}_n/\text{pred}_n > 0.75 \\ \delta_n & \text{otherwise} \end{cases}$$

Set $\mathbf{U}_{n+1} = \mathbf{U}_n + \mathbf{s}'_n$, update $n \leftarrow n + 1$ and return to step (2).

4.3.4 Linear solver

The computation of the Newton step according to Equation (4.5) requires the inversion of the Jacobian matrix. For most of the problems presented in this work, the system is solved by using the package Parallel Sparse Direct and Multi-Recursive Iterative Linear Solvers (PARDISO), originally developed by Schenk et al. (Schenk et al., 2000; Schenk and Gärtner, 2002; Schenk and Gärtner, 2004), from the “Intel(R) Parallel Studio XE 2018 Update 3 Cluster Edition for Windows” library collection. However for some of the testcases presented in this work, particularly the cases where combustion is present, the use of PARDISO for the solution of the linear problem was not possible due to memory problems. A limit of approximately 500,000 DOFs was observed. For larger problems an iterative scheme was used.

An active field of study in the BoSSS development group is that of iterative algorithms for solving linear systems. The BoSSS code features a multigrid orthonormalization algorithm (Kummer et al., 2021), which uses additive Schwarz schemes as smoothers for all multigrid levels, except the coarsest one, where PARDISO is used. This method of solution proved to be adequate to solve systems that are too big to be solved directly by PARDISO, and is adopted for all combustion calculations. Additionally, BoSSS includes a matrix preconditioning procedure using LU-factorization. In particular, it allows preconditioning of each block of the matrix, with the objective of reducing the condition number of the system.

4.3.5 Termination criterion

The usual approach to determine whether the nonlinear solver should terminate is to check whether the residual norm has fallen under a certain threshold, i.e. $\|\mathcal{A}(U_n)\| \leq \text{tol}$. As noted by Pawłowski et al. (2008), this approach is not always helpful. A universal choice of tolerance is in fact difficult, especially for investigations of the convergence properties of numerical methods. The reason for this is that, if the tolerance tol is chosen to be too high, the error due to the premature termination may dominate the error of the spatial discretization and the advantages offered by the high-order methods cannot be fully employed. On the other hand, if the tolerance is set too low, the algorithm may never terminate, due to dominant numerical rounding errors. Therefore, the goal is to continue the Newton-Dogleg method until the lowest possible limit dictated by the floating point precision is reached.

To identify the limit in a robust way, the residual-norm skyline is defined as

$$\text{sr}_n := \min_{j \leq n} \|\mathcal{A}(\mathbf{U}_j)\| \quad (4.16)$$

and, for $n \geq 2$, the averaged reduction factor

$$\text{arf}_n := \frac{1}{2} \left(\frac{\text{sr}_{n-2}}{\max\{\text{sr}_{n-1}, 10^{-100}\}} + \frac{\text{sr}_{n-1}}{\max\{\text{sr}_n, 10^{-100}\}} \right). \quad (4.17)$$

The Newton-Dogleg method is terminated if

$$n \geq 2 \text{ and } \text{sr}_n \leq 10^{-5} + 10^{-5} \|\mathbf{U}_n\|_2 \text{ and } \text{arf}_n < 1.5. \quad (4.18)$$

The skyline approach ensures robustness against oscillations close to the lower limit. For the computations in this work, this choice guarantees that the nonlinear system is solved as accurately as possible. It secures that the numerical error is dominated by the error of the spatial or temporal discretization and not by the termination criterion of the Newton-Dogleg method.

4.4 Additional convergence supporting strategies

Although the Newton-Dogleg method works well for a variety of cases, in some of the test cases discussed in this work, convergence problems are encountered. This section shows a series of strategies used in the present work that allowed the solution of problems where large nonlinearities, or the lack of adequate initial estimates, made it difficult to obtain results by simply using the Dogleg-Method Newton.

4.4.1 Homotopy method

In some cases the problem to be solved contains some parameter that makes it difficult to obtain a result using the methods presented above. A typical example of this is a system where the Reynolds number is very high. An approach that makes it easier to obtain a solution is to choose as an initial guess a solution of a similar but simpler problem - such as the same system with a moderate Reynolds number - where even with a bad initial guess Newton's algorithm is able to obtain a solution. This strategy can be used repeatedly to gradually approach the full system. Such approaches are usually called homotopy methods (also called homotopy continuation methods).

The choice of the values of the parameter of the intermediate steps of the homotopy method is a point that requires attention. A straightforward option would be to manually choose the path to the solution. While such a strategy proved useful in cases such as the one presented in (Klingenberg, 2022) for a turbulent boundary layer flow, the requirement for user intervention to choose a suitable homotopy path makes it a not always robust solution.

Based on the above, a methodology for homotopy methods was implemented in the BoSSS framework making use of an algorithm that automatically determines a homotopy path to the full system solution. This algorithm is based on the ideas from the textbook by Deuflhard (2011). In this section the main ideas of the algorithm are presented, as already shown in (Gutiérrez-Jorquera and Kummer, 2022b). For a more detailed explanation of the method, the interested reader is referred to the mentioned textbook.

The first step is to identify a parameter that causes difficulties in the solution of the nonlinear problem. Hereafter this variable will be referred to as the homotopy parameter h_p . As mentioned, the main idea of the homotopy strategy is to solve a series of simpler problems, starting with a parameter where the problem is easy to solve, and carefully increasing it until the desired value is reached. Let H_p be the value of the homotopy parameter for which a solution is sought. Let

$$\mathcal{A}_{h_p^*}(\mathbf{U}) = 0 \quad (4.19)$$

be the discretized system for a certain intermediate homotopy-parameter h_p^* , between 0 and the target homotopy-parameter H_p , i.e. $0 \leq h_p^* \leq H_p$. In addition, let $\mathbf{U}_{h_p, \epsilon}$ be an approximate solution to the problem (4.19) with $h_p^* = h_p$, up to a tolerance ϵ , i.e.

$$\|\mathcal{A}_{h_p}(\mathbf{U}_{h_p, \epsilon})\|_2 \leq \epsilon. \quad (4.20)$$

For the sake of clarity when discussing the algorithm which follows below, a distinction is made between the intermediate homotopy-parameter h_p for which it is assumed to already have found an acceptable solution, and the next homotopy-parameter h_p^* whose solution is being looked for. For any $h_p^* > h_p$, $\epsilon = 10^{-5} \|\mathcal{A}_{h_p^*}(\mathbf{U}_{h_p, \epsilon})\|_2$ is set, meaning that the accepted solution for the intermediate homotopy parameter h_p^* should show a residual norm reduction

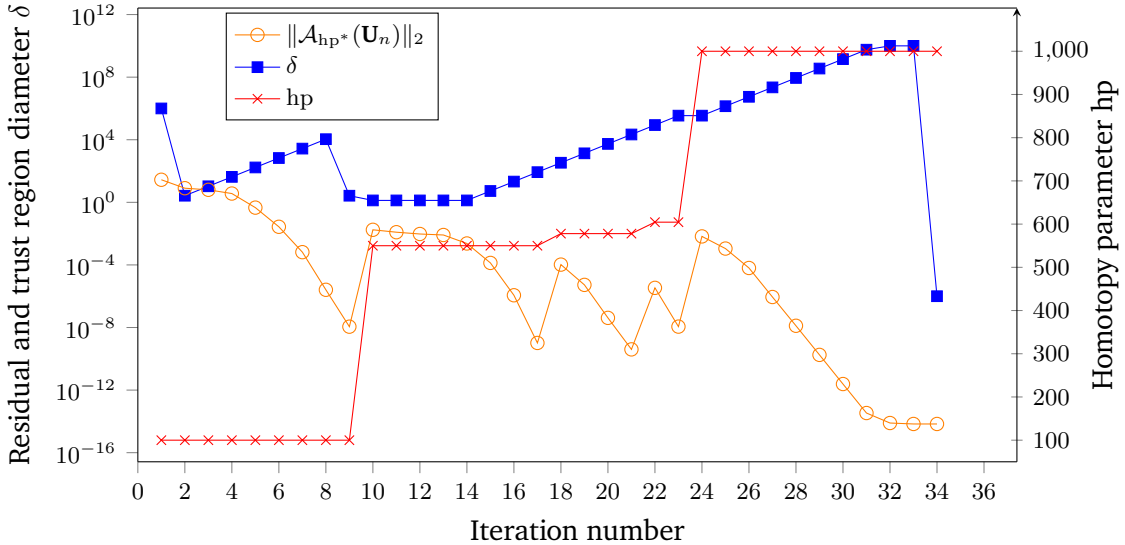


Figure 4.1: Residual, trust region diameter and homotopy parameter history of the differentially heated cavity test case using the Homotopy strategy. The homotopy parameter hp in this case is the Reynolds number.

of at least five orders of magnitude with respect to the initial residual norm. Finally, if $hp^* = Hp$, the termination criterion presented in section 4.3.5 is applied. An approximate solution for the target homotopy-parameter is obtained by means of the following algorithm:

- (1) Set $hp = 0$, i.e. start by obtaining an (approximate) solution $\mathbf{U}_{0,\epsilon}$.
- (2) Search for an increased homotopy-parameter hp^* : Find the minimal $i \geq 0$ so that for $hp^* = \frac{1}{2^i}(Hp - hp) + hp$ one has $\|\mathcal{A}_{hp^*}(\mathbf{U}_{hp,\epsilon})\|_2 \leq \delta_{\max} \|\mathcal{A}_{hp}(\mathbf{U}_{hp,\epsilon})\|_2$. Here, δ_{\max} is the maximal allowed increase of the residual for an increased homotopy-parameter hp^* ; δ_{\max} is adapted in the following steps, as an initial guess $\delta_{\max} = 10^6$ is used.
- (3) Use the Newton-Dogleg method to compute an approximate solution to the problem (4.19), for the homotopy-parameter hp^* , using the solution $\mathbf{U}_{hp,\epsilon}$ as an initial guess.
 - If the Newton-Dogleg method did not converge successfully within ten steps, the homotopy-parameter increase from hp to hp^* was probably too large. Set $\delta_{\max} \leftarrow 0.2\delta_{\max}$ and go to step (2).
 - If the Newton-Dogleg method reached its convergence criterion and if the target homotopy-parameter is reached, i.e. $hp^* = Hp$, the algorithm has successfully found an approximate solution for $\mathcal{A}_{Hp}(\mathbf{U}) = 0$ and can terminate.
 - Otherwise, if the Newton-Dogleg method converged successfully, but is below the target homotopy-parameter: Accept the solution and set $hp \leftarrow hp^*$. If the Newton-Dogleg method took less than three iterations to reach the convergence criterion, set $\delta_{\max} \leftarrow 8\delta_{\max}$. Return to step (2).

An exemplary run of the method is shown in Figure 4.1. The homotopy parameter hp in this particular case is the Reynolds number. The homotopy-parameter hp was increased for iterations 10, 18, 22 and 24, causing an increase of the residuals $\|\mathcal{A}_{hp^*}(\mathbf{U}_n)\|_2$, leading to

a convergent solution after 34 Newton iterations. The presented algorithm offers a robust method for finding steady-state solutions of highly nonlinear systems.

4.4.2 Solver safeguard

Another strategy that proved to be useful in improving the convergence properties of the iterative scheme is the use of a solver safeguard, which is used to avoid unphysical solutions during the solution procedure, such as negative temperatures or temperatures higher than the adiabatic temperature.

In particular, the basic idea is to clip values from the solution fields delivered by Newton's algorithm which are known to be unphysical, and limit the solution fields by user defined values. This clipping emulates in a sense the effect of schemes such as Total Variation diminishing Method (TVM) or Essentially Non-Oscillatory methods (ENO) (Nicoud, 2000).

For an arbitrary scalar ξ the values are bounded in the range $[\xi_{\min} - \epsilon_{\text{safe}}, \xi_{\max} + \epsilon_{\text{safe}}]$, where ξ_{\min} and ξ_{\max} are user defined bounds, and $\epsilon_{\text{safe}} = 10^{-4}$. For example, the mass fractions by definition should have a value between zero and one, thus $Y_{k,\min} = 0$ and $Y_{k,\max} = 1$. For certain problems, particularly problems involving combustion, it could be also useful to limit the value of the temperature, which can be bounded using the inlet conditions as the minimum value, and the adiabatic temperature as the maximum value.

The occurrence of these non-physical values is not always problematic, and in theory the Newton algorithm above should be able to correctly handle them and finally find the solution of the nonlinear system. However in certain cases this can lead to problems. Just to mention one example, a negative temperature would result in a imaginary value of the viscosity if it is calculated according to Equation (2.29). Particularly for problems with sharp gradients this could be problematic due to dispersion phenomena.

4.4.3 Flame sheet estimates for steady state combustion simulations

The proposed algorithm for obtaining steady state solutions of finite reaction rate combustion problems involves first solving the problem assuming an infinite reaction rate (the flame sheet problem). This requires first solving the system presented in Section 2.2, where Equations (3.43a) to (3.43c) need to be solved in a coupled manner together with the expressions that link the temperature and mass fractions to the mixture fraction in order to be able to evaluate the density and transport parameters. This idea has been already employed in various works (Smooke et al., 1986a; Smooke and Giovangigli, 1992).

The reason for the use of this pre-step is twofold:

- Solving Equations (2.22a) to (2.22d) using a Newton-type method requires adequate starting estimates in order to converge. Using the flame sheet solution as initial estimate improves the convergence properties of the method.
- The system of Equations (2.22a) to (2.22d) has multiple solutions. One is the pure mixing (frozen) solution, where no chemical reaction has taken place, and other one is the ignited solution, where the flame is present (see Figure 2.1). Using the flame sheet solution as initial estimate makes much more likely that the path taken by Newton's algorithm will tend towards the ignited solution.

This approach proved to be very useful for finding solutions of steady state flame simulations in a variety of cases.

One question one could certainly ask is under what flame conditions the infinite reaction rate solution (also called flame sheet solution in the following) effectively is a good initial estimate for Newton's algorithm. Obviously for systems that respect the assumptions done for the flame sheet the obtained solution will be very close to the finite-rate solution (see Figure 2.2). The assumption of an infinitely fast chemical reaction implies that the time scales associated with the chemical reaction are infinitely smaller than the flow scales, or in other words, $\text{Da} \rightarrow \infty$. For this reason, the flame sheet solution is expected to give a similar solution for cases close to equilibrium (where the Damköhler number is large). On the other hand, in cases that are far from equilibrium, as, for example, in the case of a flame in conditions close to extinction, it is expected that the flame sheet solution will depart considerably from the solution with a finite reaction rate.

It should be noted that within the derivation of the equations for the flame sheet it is only assumed that the heat capacity is the same for all components ($c_{kp} = c_p$), but it is still possible to consider a dependence on temperature. However, this introduces a difficulty, since the evaluation of the temperature with Equation (2.35) requires c_p , which according to Equation (2.28), depends in turn on the temperature. Solving the system of equations required to obtain c_p and T is very expensive, since it would require solving it every time the temperature must be evaluated -in particular for the evaluation of the density ρ and transport parameters μ and ρD . This problem can be solved by simply assuming a constant representative value of c_p .

The problem that now arises is the selection of a suitable c_p . In the work by Xu and Smooke (1993) it is suggested to estimate it simply on the basis of experimental measurements, or also by selecting some representative value, such as c_p evaluated at the adiabatic temperature and stoichiometric conditions. In particular, in this work the value $\hat{c}_p = 1.3 \text{ kJ kg}^{-1} \text{ K}^{-1}$ was adequate for all calculations. This constant value of the heat capacity proved to yield a flame sheet solution which is an adequate estimate for finite-rate simulations, even for cases with a nonconstant heat capacity.

In a similar fashion, the assumption of unity Lewis number in the flame sheet system delivers a solution that slightly deviates from the solution of the finite chemistry rate problem with nonunity Lewis numbers. Nevertheless, this small deviation does not preclude the use of the flame sheet solution as an adequate initial estimate for Newton's method.

Smoothing of the flame sheet

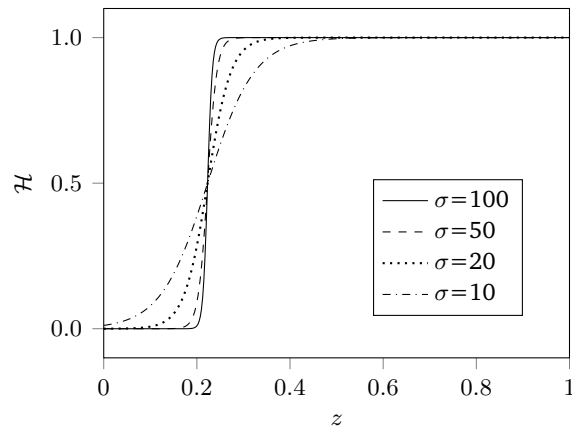


Figure 4.2: Smoothing function at $z_{\text{st}} = 0.22$ for different smoothing parameters σ .

It should be noted regarding the solution of the flame sheet problem (cf. Section 2.2) that the sharp change in the primitive variables around $z = z_{st}$ is problematic in certain scenarios. In particular, the non-smoothness of the derived variables could lead to Gibbs phenomenon-type problems if the stoichiometric point happens to be in a unfavourable position within a cell. This inconvenient can be remedied to a certain extent by using a regularized form of the equations. The smoothing function \mathcal{H} is defined as

$$\mathcal{H}(z) \approx \frac{1}{2}(1 + \tanh(\sigma(z - z_{st}))). \quad (4.21)$$

This function is useful for creating a smooth transition between two functions, since it returns values close to 0 for $z \ll z_{st}$ and values close to 1 for $z \gg z_{st}$. The sharpness of the transition at the point $z = z_{st}$ is dictated by the parameter σ . In Figure 4.2 the smoothing function \mathcal{H} using different smoothing parameters σ is shown. Clearly, increasing the value of σ increases the sharpness of the transition at the point z_{st} . For a very big σ value the function \mathcal{H} resembles the Heaviside step function

Using Equation (4.21) for creating a smooth transition of Equations (2.34) to (2.37), the temperature and mass fraction fields can be written as

$$T(z) = zT_F^0 + (1 - z)T_O^0 + \frac{QY_F^0}{c_p} z_{st} \frac{1 - z}{1 - z_{st}} \mathcal{H}(z) + \frac{QY_F^0}{c_p} z (1 - \mathcal{H}(z)), \quad (4.22a)$$

$$Y_F(z) = Y_F^0 \frac{z - z_{st}}{1 - z_{st}} \mathcal{H}(z), \quad (4.22b)$$

$$Y_O(z) = Y_O^0 \frac{z_{st} - z}{z_{st}} (1 - \mathcal{H}(z)), \quad (4.22c)$$

$$Y_P(z) = Y_O^0 \frac{M_P \nu_P}{M_O \nu_O} (1 - z) \mathcal{H}(z) + Y_F^0 \frac{M_P \nu_P}{M_F \nu_F} z (1 - \mathcal{H}(z)), \quad (4.22d)$$

$$Y_N(z) = (1 - Y_F^0)z + (1 - Y_O^0)(1 - z). \quad (4.22e)$$

The use of this regularized form of the equations results in practice on a spreading of the flame front, which eases the numerical calculation (Braack et al., 1997). In Figure 4.3 the effect of the smoothing factor σ on calculations of a flame in a counter-flow configuration are shown. It can be clearly observed how for decreasing σ the solution becomes smoother.

4.4.4 Adaptive Mesh Refinement

The BoSSS code offers the capability to modify throughout the simulation the numerical mesh by means of an Adaptive Mesh Refinement (AMR) algorithm. In particular, the locality of a DG method allows a straightforward implementation, as the DG discretization admits the apparition of hanging nodes in the numerical mesh. The base mesh can be refined by subdividing a cell element into four elements of the same size using a quadtree-like data structure. It is also ensured that neighbouring cells always exhibit a 2:1 cell ratio on every edge (Smuda, 2021).

The mesh refinement process occurs before each time-step is started. This allows to use the AMR algorithm on start of the application, which can be useful in case the user needs an increased mesh resolution in particular areas of the computational domain. Note that, in practice, the mesh-refinement procedure results in a soft-restart of the simulation.

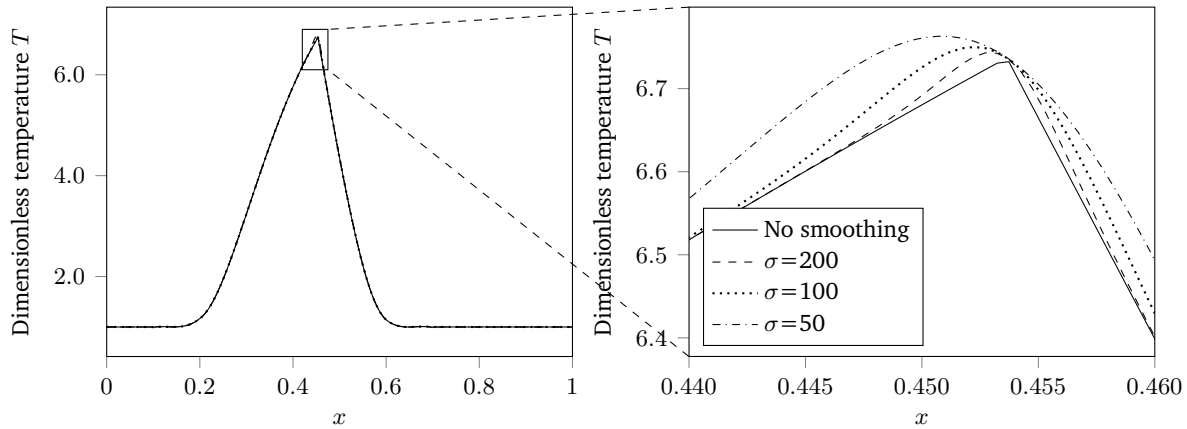


Figure 4.3: Temperature profile calculated in the center-line of a counter-flow flame configuration for different smoothing parameters σ .

The mesh refinement is controlled by user defined refinement-coarsening criteria. During the development of the XNSEC solver different refinement strategies were investigated and implemented. Some of them worth mentioning are the refinement strategy `AMRBasedOnFieldGradient`, where the mesh is refined or coarsened based on the magnitude of the gradients of a particular solution field. For simulations where combustion is present, a sensible choice for the refinement strategy are the magnitude of temperature gradients or magnitude of mass fraction gradients. Additionally, the strategy `AMRonFlameSheet` allows the refinement/coarsening around the stoichiometric surface $z = z_{st}$.

In Figure 4.4 the refinement of a coflowing flame configuration using the `AMRonFlameSheet` strategy is shown. The mentioned strategies proved to be useful in combustion simulations, as will be discussed later.

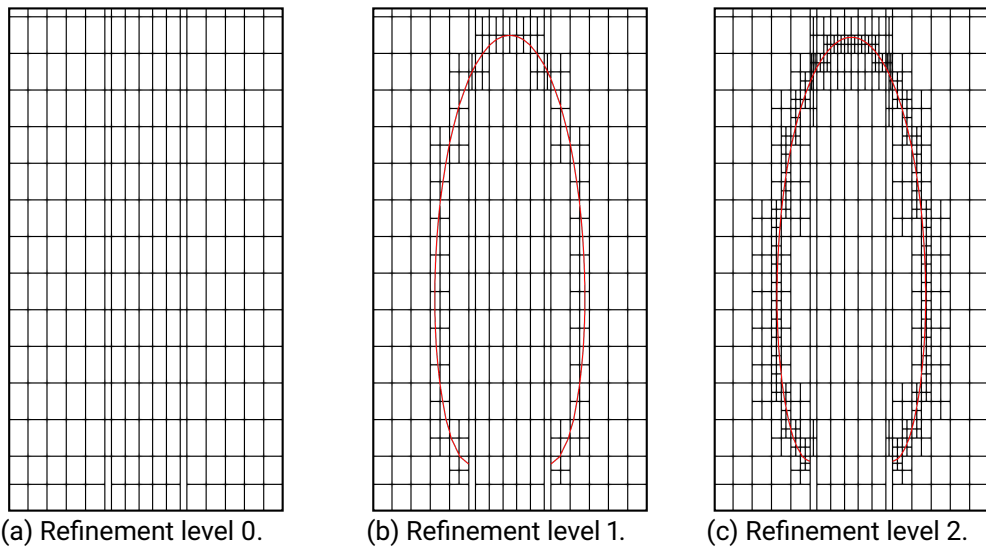


Figure 4.4: Adaptive mesh refinement around the stoichiometric surface in a coflow flame configuration. The iso-contour $z = z_{st}$ of the mixture fraction is shown in red.

5 Numerical results

The following sections show a comprehensive solver validation using various test cases presented in increasing levels of complexity. The tests also allow to highlight some of the benefits of the DG method and the algorithms introduced before in this work, namely the globalized Newton method, homotopy strategy and the initialization of combustion applications using flame sheet estimates.

First, in Section 5.1 the applicability of the solver is analyzed for isothermal single-component systems. Later in Section 5.2 several single-component non-isothermal configurations are studied. Finally, in Section 5.3 test cases for multicomponent non-isothermal systems are presented, with a particular emphasis on systems where combustion is present.

All calculations shown here were performed on a cluster with the following specifications:

- CPU 4x8 cores (Intel(R) Xeon(R) CPU E5-4627 v2)
- CPU vector extension Intel® AVX
- CPU speed basis 3.30 GHz, turbo 3.6 GHz
- Memory 512 GByte (DDR3-1600)

Unless otherwise stated, all calculations use the termination criteria presented in Section 4.3.5. Some of the results presented in this section have been published in (Gutiérrez-Jorquera and Kummer, 2022a).

In the following, only two dimensional configurations are considered. However, the methods shown in this work could be also used for three-dimensional problems.

5.1 Single-component isothermal cases

The XNSEC solver presented in the previous chapter is validated first for single-component isothermal cases. In these cases, only the continuity and momentum equations are solved. The energy equation and the species concentration equations are replaced by the conditions $T = 1.0$ and $Y_0 = 1.0$ in the entire domain. This means that the physical properties of the flow (density and viscosity) are constant. Therefore, the flow is totally incompressible, since the density shows no thermodynamic or hydrodynamic dependence.

5.1.1 Lid-driven cavity flow

The lid-driven cavity flow is a classic test problem used for the validation of Navier-Stokes solvers. The system configuration is shown in Figure 5.1. It consists simply of a two-dimensional square cavity enclosed by walls whose upper boundary moves at constant velocity, causing the fluid to move. Benchmark results can be found widely in the literature for different Reynolds

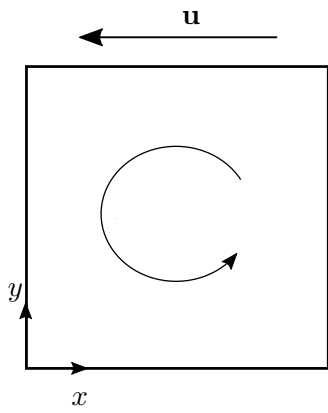


Figure 5.1: Schematic representation of the Lid-Driven cavity flow.

numbers. In this section, the results obtained with the XNSEC solver are compared with those published by Botella and Peyret (1998).

The problem is defined in the domain $\Omega = [0, 1] \times [0, 1]$. The system is solved for the velocity vector $\mathbf{u} = (u, v)$ and the pressure p . All boundary conditions are Dirichlet-type, particularly with $\mathbf{u} = (-1, 0)$ for the boundary at $y = 1$ and $\mathbf{u} = (0, 0)$ for all other sides. The gravity vector is set to $\mathbf{g} = (0, 0)$. A Cartesian mesh with extra refinement at both upper corners is used, and is shown in Figure 5.2. The refinement was done to better represent the complex effects that take place in the corners. The streamline plot presented in Figure 5.2 shows the different vortex structures typical of this kind of system, where in addition to the main vortex of the cavity, smaller structures appear in the corners.

The lid-driven cavity was calculated for a Reynolds number $Re = 1000$. For the calculations presented here, the polynomial degree is set to four for both velocity components and three for the pressure. A regular Cartesian mesh with 16×16 elements is used with extra refinement in the corners. In Figure 5.3 a comparison of the calculated velocity with the DG-Solver and the velocities provided by the benchmark is shown. Clearly, very good agreement is obtained, even by using a relatively coarse mesh (the benchmark result uses a grid with 160×160 elements).

A more rigorous comparison of results is presented in Table 5.1, where the extreme values

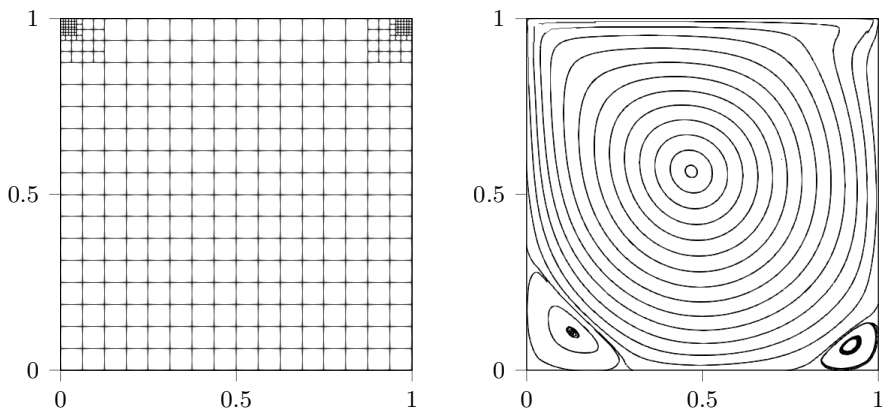


Figure 5.2: Mesh and streamlines of the lid-driven cavity flow with $Re = 1000$

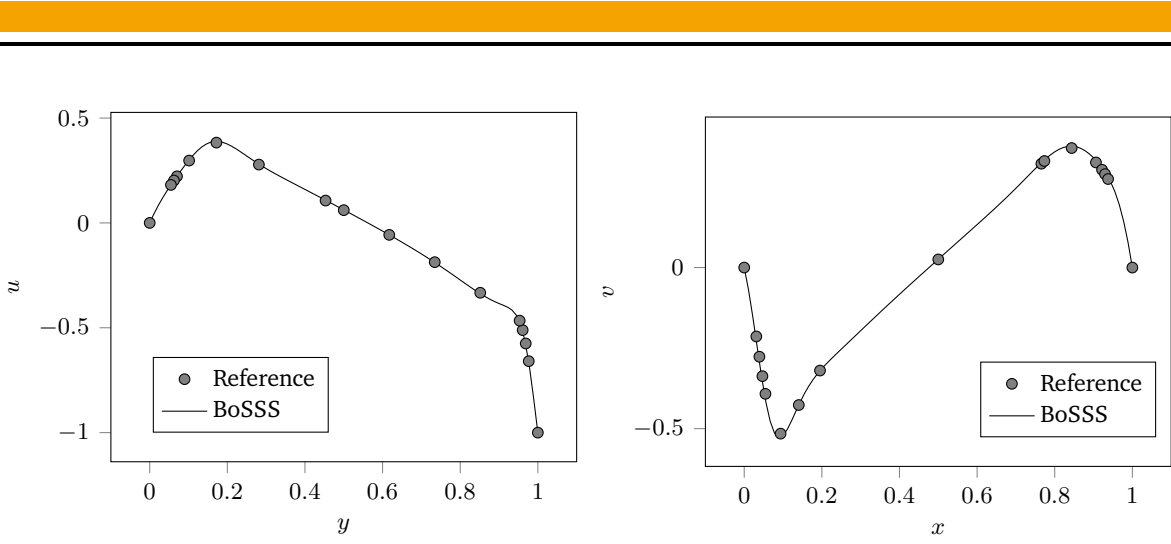


Figure 5.3: Calculated velocities along the centerlines of the cavity and reference values. Left plot shows the x-velocity for $x = 0.5$. Right plot shows the y-velocity for $y = 0.5$

Mesh	u_{\max}	y_{\max}	v_{\max}	x_{\max}	v_{\min}	x_{\min}
16×16	0.3852327	0.1820	0.3737295	0.8221	-0.5056627	0.0941
32×32	0.3872588	0.1821	0.3760675	0.8227	-0.5080496	0.0943
64×64	0.3897104	0.1748	0.3774796	0.8408	-0.5248360	0.0937
128×128	0.3886452	0.1720	0.3770127	0.8422	-0.5271487	0.0907
256×256	0.3885661	0.1717	0.3769403	0.8422	-0.5270653	0.0907
Reference	0.3885698	0.1717	0.3769447	0.8422	-0.5270771	0.0908

Table 5.1: Extrema of velocity components through the centerlines of the lid-driven cavity for $\text{Re} = 1000$. Reference values obtained from Botella and Peyret (1998)

of the velocity components calculated through the centerline of the cavity are compared with the results presented by Botella and Peyret (1998). Different mesh resolutions were used for this comparison, particularly meshes with 16×16 , 32×32 , 64×64 , 128×128 and 256×256 elements, each with extra refinement at the corners. It can be clearly seen how for the finest mesh the results obtained with the DG-solver are extremely close to the reference. A difference is only appreciated at the fifth digit after the decimal point for the velocity components. In case of the position of the extremal values no difference is observed. It can also be seen that the results obtained with the coarser meshes are still very close to those of the reference.

5.1.2 Backward-facing step

The backward-facing step problem is another classical configuration widely used for validation of incompressible CFD codes. It has been widely studied theoretically, experimentally, and numerically by many authors in the last decades (see, for example, Armaly et al. (1983), Barkley et al. (2000), and Biswas et al. (2004)). In Figure 5.4 a schematic representation of the problem is shown. It consists of a channel flow (usually considered fully developed) that is subjected to a sudden change in geometry that causes separation and reattachment phenomena. For these reasons, this case can be considered more challenging than the one presented in the previous section, since special care of the mesh used has to be taken in order to capture accurately all complex phenomena taking place.

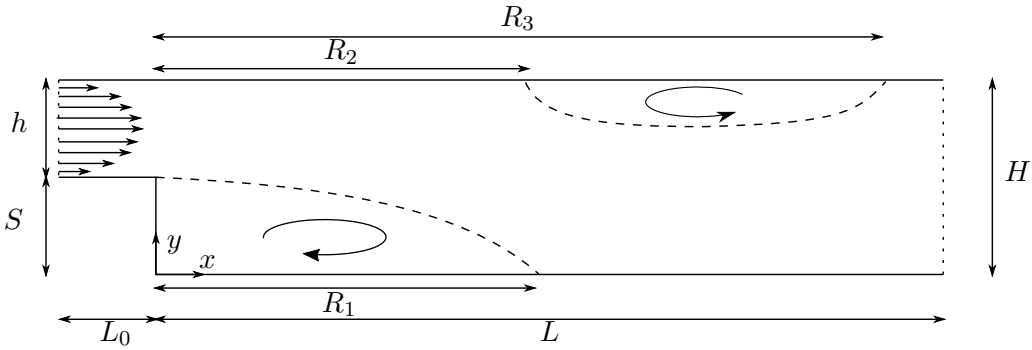


Figure 5.4: Schematic representation (not to scale) of the backward-facing step. Both primary and secondary vortices are shown.

Although the backward-facing step problem is known to be inherently three-dimensional, it has been shown that it can be studied as a two-dimensional configuration along the symmetry plane for moderate Reynolds numbers. For the range of Reynolds numbers used in the calculations presented here, the two-dimensional assumption is justified (Barkley et al., 2000; Biswas et al., 2004). The origin of the coordinate system is set in the bottom part of the step. The step height S and channel height h characterize the system. Results in the literature are often reported as a function of the expansion ratio, defined as $\text{ER} = (h + S)/h$.

A series of simulations were performed with the objective of reproducing the results reported by Biswas et al. (2004), where the backward-facing step was calculated for Reynolds numbers up to 400 and for an expansion ratio of $\text{ER} = 1.9423$. In particular, the reported lengths of detachment and reattachment are used as a means of comparison with the results from the XNSEC solver.

The Reynolds number for the backward-facing step configuration is defined in the literature in many forms. Here, the definition based on the step height \hat{S} and the mean inlet velocity \hat{U}_{mean} is adopted as the reference length and velocity, resulting in

$$\text{Re} = \frac{\hat{S}\hat{U}_{\text{mean}}}{\hat{\nu}}. \quad (5.1)$$

The boundary at $x = -L_0$ is an inlet boundary condition, where a parabolic profile is defined with

$$u(y) = -6 \frac{(y - S)(y - (h + S))}{h^2} \quad (5.2)$$

The system is isothermal, and the fluid is assumed to be air. The step length is set $S = 1$ and $h = 1.061$. To minimize the effects of the outlet boundary condition on the part of interest in the system, the length L of the domain is set to $L = 70S$. All other boundaries are fixed isothermal walls. Based on prior calculations, the effect of the domain length before the step was found to have almost no impact on the results and is set to $L_0 = S$. Preliminary studies showed that the calculated reattachment and detachment lengths are highly sensitive to the mesh resolution. For all simulations in this section, a structured grid with 88,400 elements is used. To better resolve the complex structures that occur in this configuration, smaller elements are used in the vicinity of the step, as seen in Figure 5.5. A polynomial degree of three was chosen for both velocity components and two for pressure.

The backward-facing step configuration exhibits varying behavior as the number of Reynolds changes. For small Reynolds numbers, a single vortex, usually called the primary vortex, appears

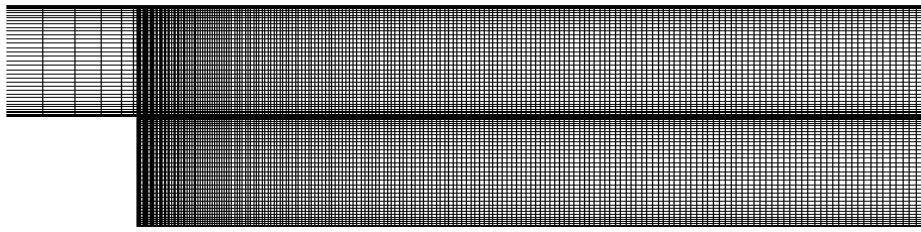


Figure 5.5: Mesh used for the backward-facing step configuration.

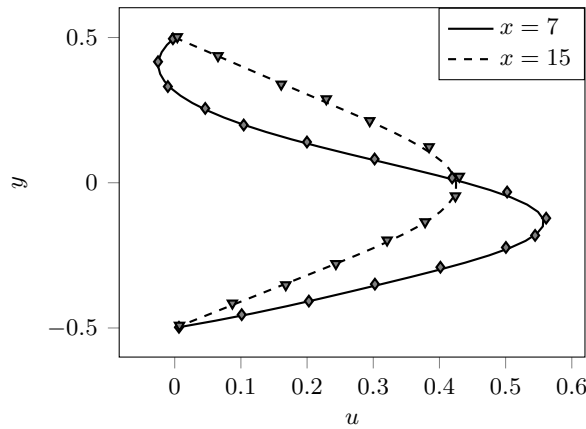


Figure 5.6: Distribution of x-component of velocity in the backward-facing step configuration for a Reynolds number of 400. Solid lines correspond to results obtained with the XNSEC solver.

in the vicinity of the step. Furthermore, as the Reynolds number increases, a second vortex eventually appears on the top wall, as shown schematically in Figure 5.4. The detachment and reattachment lengths of the vortices are values that are usually reported in the literature. It is possible to determine the detachment position by finding the point along the wall where the velocity gradient normal to the wall acquires a value equal to zero.

Figure 5.7 shows the detachment and reattachment lengths of the primary and secondary vortices obtained with the XNSEC solver for different Reynolds numbers, which are also compared with the results presented in the reference paper from Biswas et al. (2004). Cubic splines and a bisection method have been used to accurately locate this point. It can be seen that the results for the detachment lengths of the primary vortex R_1 are in very good agreement with those of the reference. In the case of the secondary vortex, it is possible to see a very minimal deviation for the lengths of the reattachment R_3 , hinting at a possible spatial under-resolution far away from the step. It is interesting to note that, despite the fact that the reference does not report the existence of a secondary vortex for $\text{Re} = 200$, it was possible to observe it with the XNSEC solver. The results allow to conclude that it is possible to study flows with complex behavior for low- to moderate Reynolds numbers, at least in the isothermal case. In the next section, a non-isothermal case of this configuration will be studied.

It is worth mentioning that the evaluation of the global order of accuracy of the solver using the two incompressible test cases presented in this section is problematic due to the presence of singularities. Specifically the points at the corners at the coordinates $\mathbf{x} = (0, 1)$ and $\mathbf{x} = (1, 1)$ of the Lid-driven cavity (where the pressure is not finite according to Botella and Peyret (1998)), and at the corner of the step $\mathbf{x} = (0, S)$ of the backward-facing step are problematic. The

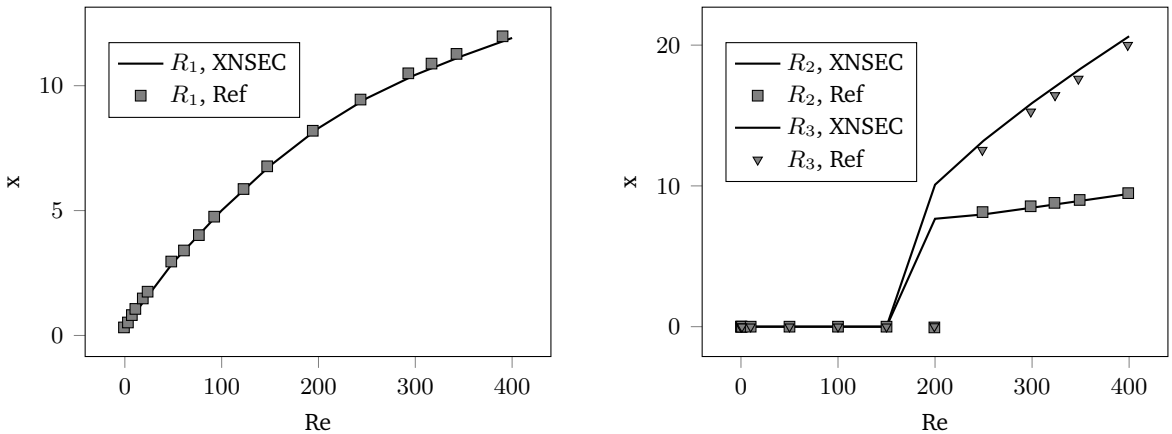


Figure 5.7: Detachment and reattachment lengths of the primary (left figure) and secondary (right figure) recirculation zones after the backward-facing step compared to the reference solution (Biswas et al., 2004).

accuracy of the solver will be assessed later in Section 5.2.2 making use of a analytical solution and in Section 5.2.3 using a solution obtained with a high spatial resolution.

5.2 Single-component non-isothermal cases

For the test cases presented in this section, the equations for continuity, momentum and energy are solved. All systems are assumed to be single-component, thus $N = 1$ and $Y_0 = 1.0$. The tests shown in this section shall serve as a throughout validation of the XNSEC solver spatial and temporal discretization for low-Mach variable density flows.

First in Section 5.2.1 an extension of the backward-facing step configuration for a non-isothermal system is shown, and benchmark values are compared to references. Later in Section 5.2.2 a Couette flow configuration that presents a temperature gradient in the vertical direction is studied and compared to an analytical solution. Additionally the numerical accuracy of the solver is shown and compared to calculations using a SIMPLE-type algorithm. Later in Section 5.2.3 a heated square cavity configuration is studied to assess the solver's ability to simulate steady state flow configurations of variable density in closed systems. In Section 5.2.4 the flow over a heated cylinder is studied, which serves as a test for unsteady calculations of non-isothermal systems. Finally in Section 5.2.5 a classical Rayleigh-Bénard convection system is treated, showing the behavior of the solver for unstable systems.

5.2.1 Heated backward-facing step

As an extension to the previous case the backward-facing step configuration in a non-isothermal configuration is studied. In this case the bottom wall is heated to a constant temperature and higher than the inlet temperature.

In this section the configuration for a heated backward-facing step proposed in the work of Xie and Xi (2016) is solved. The fluid entering the system has a temperature equal to $\hat{T}_0 = 283\text{ K}$ and the bottom wall is set to a constant temperature of $\hat{T}_1 = 313\text{ K}$. The inlet temperature is used as the reference temperature, obtaining $T_0 = 1.0$ and $T_1 = 1.106$. In

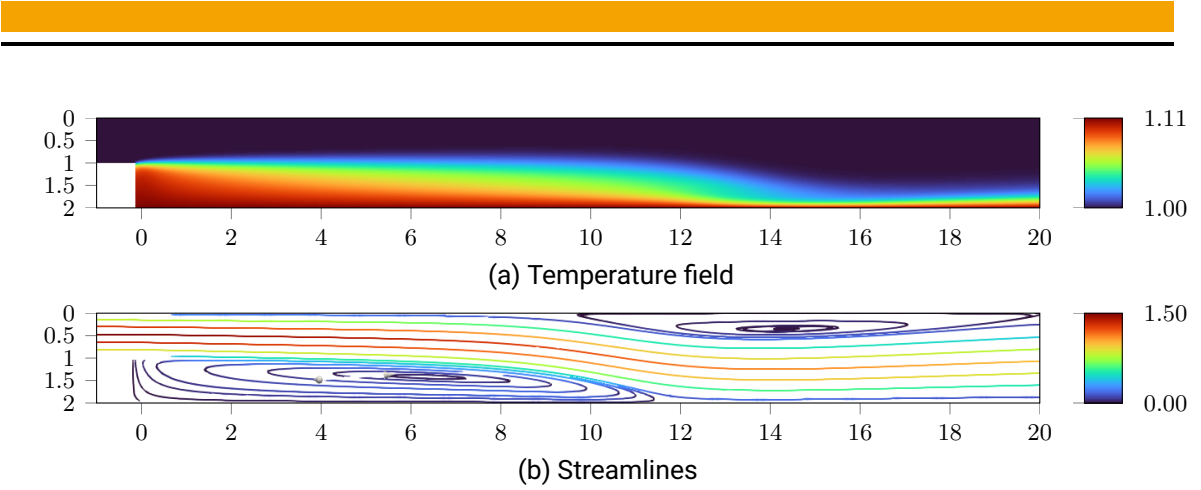


Figure 5.8: Temperature profile and streamlines corresponding to the backward-facing Step configuration for $\text{Re} = 400$ and an expansion ratio of two.

the work of Xie and Xi (2016) results are reported for the local Nusselt numbers and the local friction coefficients f_d along the bottom wall ($y = 0$) for different expansion ratios and Reynolds numbers. By combining the definition of the Nusselt number ($\text{Nu} = \hat{h}\hat{L}/\hat{\lambda}$), Newton's law of cooling ($\hat{\mathbf{q}} = \hat{h}(\hat{T}_0 - \hat{T}_1)$), and Fourier's law of heat conduction ($\hat{\mathbf{q}} = \hat{\lambda}\hat{\nabla}\hat{T}$) a expression for the local Nusselt number is obtained.

$$\text{Nu}_{\text{loc}} = \frac{\hat{L}}{\hat{T}_0 - \hat{T}_1} \hat{\nabla}\hat{T} \cdot \hat{\mathbf{n}} \quad (5.3)$$

where \hat{L} is the reference length. $\hat{L} = \hat{S}$ is chosen to be consistent with the definition of the Reynolds number of the reference. Furthermore, the local friction factor can be written as

$$f_d = \frac{8\hat{\nu}}{(\hat{U}_{\text{mean}})^2} \hat{\nabla}\hat{u} \cdot \hat{\mathbf{n}} \quad (5.4)$$

Simulations were conducted for different Reynolds numbers and expansion ratios. In Figure 5.8 the temperature field and the streamlines corresponding to a calculation with $\text{Re} = 700$ are shown. Here, the apparition of the secondary vortex is seen in the top wall. Note that only a small part of the computational domain is shown. Far away from the step, a lightly skewed parabolic velocity profile is obtained, which is influenced by the density variations on the vertical direction.

For this range of temperature differences, the temperature profile is just influenced by conductive effects, since no appreciable natural convection phenomena appears. For larger temperature differences, Rayleigh-Bénard type instabilities would appear in the flow. This type of system will be treated later in Section 5.2.5.

It should be noted here that the results obtained using the XNSEC solver are substantially different from those reported by Xie and Xi (2016), and will not be shown here. However, in the work of Hennink (2022) the same is also reported, stating that with his method it was not possible to reproduce the results presented by Xie and Xi (2016).

In Figure 5.9 the local friction factor and local Nusselt number along the wall $y = 0$ are plotted for $\text{Re} = 700$ and $\text{ER} = 2$. Comparing the results from the XNSEC solver with those reported in Hennink (2022) a very good agreement can be observed. With this test it is possible to confirm that the XNSEC solver is able to deal with complex systems where heat transfer is

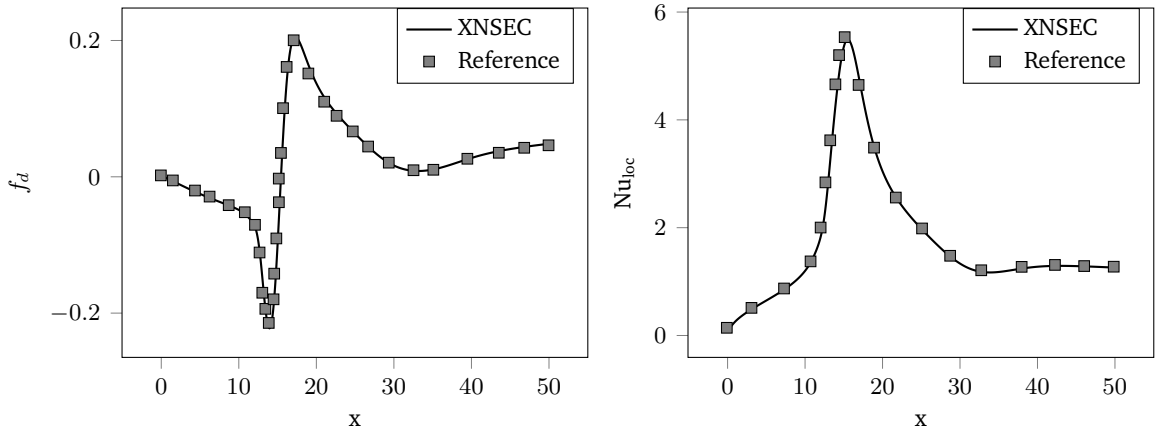


Figure 5.9: Local friction factor and local Nusselt number along the bottom wall of the backward-facing step for $\text{Re} = 700$ and an expansion ratio of two. The solid lines corresponds to the present solution and the marks to the reference (Hennink, 2022)

present. However, for the range of temperature differences involved in this case, the variation of physical parameters such as density, viscosity and thermal conductivity with respect to temperature has no appreciable influence on the simulated flow fields. The next two test-cases will show how the XNSEC solver is able to simulate low-Mach number flows with a larger temperature difference.

5.2.2 Couette flow with vertical temperature gradient

As a further test case for the low-Mach solver, a Couette flow with a vertical temperature gradient is considered. This configuration was already studied in Klein et al. (2016), where the SIMPLE algorithm was used in an DG framework for the solution of the governing equations. In this section, the results from said publication are reproduced by using the XNSEC solver, which features a fully coupled algorithm, in contrast to the SIMPLE solver, which solves the system in a segregated way. Additionally, it will be shown how the implemented solver performs in relation to the SIMPLE based solver in terms of runtime.

In Figure 5.10 a schematic representation of the test case is shown. The domain is chosen as $\Omega = [0, 1] \times [0, 1]$, and Dirichlet boundary conditions are used for all boundaries. The upper wall corresponds to a moving wall ($u = 1$) with a fixed temperature $T = T_h$. The bottom wall is static ($u = 0$) and has a constant temperature $T = T_c$. Additionally, the system is subjected to a gravitational field, where the gravity vector only has a component in the y direction. Under these conditions, the x-component of velocity, pressure, and temperature are only dependent on the y coordinate, that is, $u = u(y)$, $T = T(y)$ and $p = p(y)$. The governing equations (??) reduce to

$$\frac{1}{\text{Re}} \frac{\partial}{\partial y} \left(\mu \frac{\partial u}{\partial y} \right) = 0, \quad (5.5a)$$

$$\frac{\partial p}{\partial y} = -\frac{\rho}{\text{Fr}^2}, \quad (5.5b)$$

$$\frac{1}{\text{Re} \text{Pr}} \frac{\partial}{\partial y} \left(\lambda \frac{\partial T}{\partial y} \right) = 0. \quad (5.5c)$$

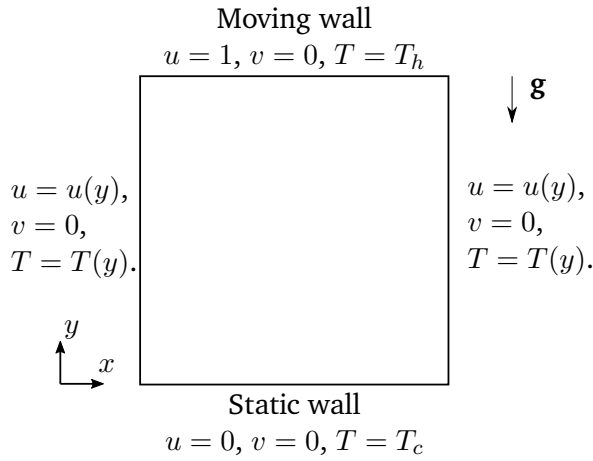


Figure 5.10: Schematic representation of the Couette flow with temperature difference test case.

By assuming a temperature dependence of the transport properties according to a Power Law ($\mu = \lambda = T^{2/3}$) it is possible to find an analytical solution for this problem.

$$u(y) = C_1 + C_2 \left(y + \frac{T_c^{5/3}}{T_h^{5/3} - T_c^{5/3}} \right)^{3/5}, \quad (5.6a)$$

$$p(y) = -\frac{5p_0}{2Fr^2} \frac{\left(y \left(T_h^{5/3} - T_c^{5/3} \right) + T_c^{5/3} \right)^{2/5}}{\left(T_h^{5/3} - T_c^{5/3} \right)} + C, \quad (5.6b)$$

$$T(y) = \left(C_3 - \frac{5}{3} C_4 y \right)^{3/5}. \quad (5.6c)$$

Where the constants C_1 , C_2 , C_3 and C_4 are determined using the boundary conditions on the upper and lower walls and are given by

$$C_1 = \frac{\left(\frac{T_c^{5/3}}{T_h^{5/3} - T_c^{5/3}} \right)^{3/5}}{\left(\frac{T_c^{5/3}}{T_h^{5/3} - T_c^{5/3}} \right)^{3/5} - \left(\frac{T_h^{5/3}}{T_h^{5/3} - T_c^{5/3}} \right)^{3/5}} \quad (5.7a)$$

$$C_2 = \frac{1}{\left(\frac{T_h^{5/3}}{T_h^{5/3} - T_c^{5/3}} \right)^{3/5} - \left(\frac{T_c^{5/3}}{T_h^{5/3} - T_c^{5/3}} \right)^{3/5}} \quad (5.7b)$$

$$C_3 = T_c^{5/3}, \quad (5.7c)$$

$$C_4 = \frac{3}{5} \left(T_c^{5/3} - T_h^{5/3} \right) \quad (5.7d)$$

and C is a real-valued constant determined by an arbitrary zero level for the pressure. The dimensionless parameters are set as $Re = 10$ and $Pr = 0.71$, $T_h = 1.6$, and $T_c = 0.4$ for all calculations. The system is considered open and the thermodynamic pressure is $p_0 = 1.0$. The Froude number is calculated as

$$Fr = \left(\frac{2Pr(T_h - T_c)}{(T_h + T_c)} \right)^{1/2}. \quad (5.8)$$

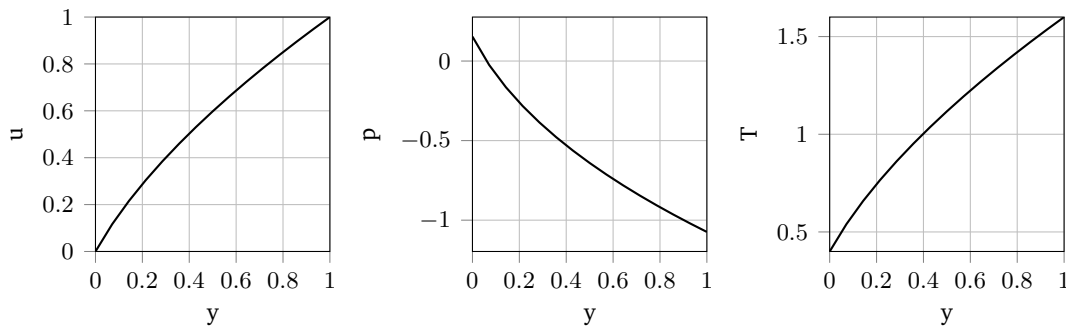


Figure 5.11: Solution of the Couette flow with vertical temperature gradient using a Power-Law.

A derivation for Equation (5.8) will be given in Section 5.2.3. In Figure 5.11 the solutions for the velocity, pressure and temperature are shown. The results are for a mesh with 26×26 elements and a polynomial degree of three for u and T , and a polynomial degree of two for p . The vertical velocity v is zero everywhere.

h-convergence study

The convergence properties of the DG method for this nonisothermal system were studied using the analytical solution described before. The domain is discretized and solved in uniform Cartesian meshes with 16×16 , 32×32 , 64×64 and 128×128 elements. The polynomial degrees for the velocity and temperature are changed from one to four and for the pressure from zero to three. The convergence criterion described in Section 4.3.5 was used for all calculations. The analytical solutions given by Equation (5.6) are used as Dirichlet boundary conditions on all the boundaries of the domain. The global error is calculated against the analytical solution using a L^2 norm. In Figure 5.12 the results of the h-convergence study are shown. Recall that, for increasing polynomial order, the expected order of convergence is given by the slope of the line curve when cell length and errors are presented in a log-log plot. Due to the mixed-order formulation used, the slopes should be equal to k for the pressure and equal to $k + 1$ for all other variables, which is possible to observe for all variables.

Comparison with SIMPLE

As mentioned before, a solver for solving low-Mach number flows based on the SIMPLE algorithm presented in Klein et al. (2016) has already been developed and implemented within the BoSSS framework. Although the solver was validated and shown to be useful for a wide variety of test cases, there were also disadvantages inherent to the SIMPLE algorithm. For example, within the solution algorithm, under-relaxed Picard-type iterations are used to search for a solution. This usually requires some prior knowledge from the user in order to select suitable relaxation factor values that provide stability to the algorithm, but at the same time do not slow down the computation substantially. The intention of this subsection is to show a comparison of runtimes of the calculation of the Couette flow with vertical temperature gradient between the DG-SIMPLE algorithm (Klein et al., 2016) and the XNSEC solver. Calculations were performed on uniform Cartesian meshes with 16×16 , 32×32 , 64×64 and 128×128 elements,

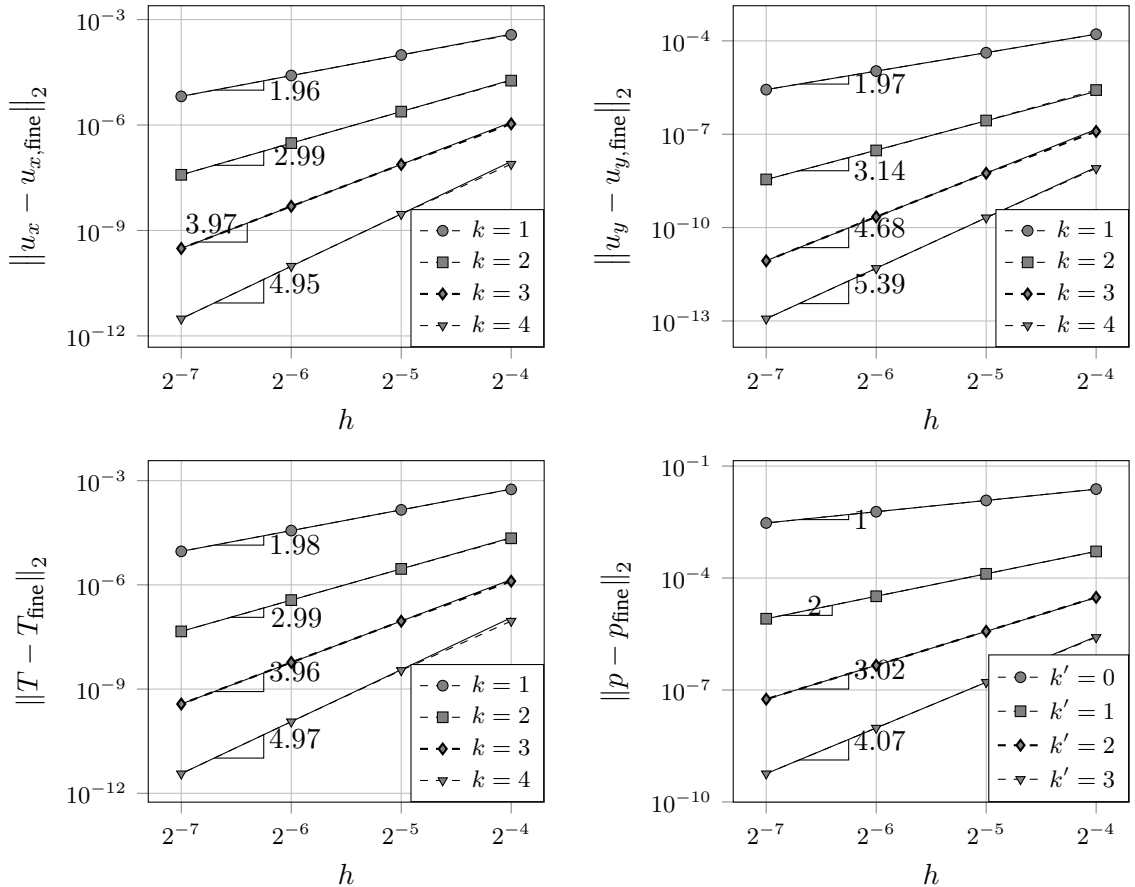


Figure 5.12: Convergence study of the Couette-flow with temperature difference. A power-law is used for the transport parameters.

and with varying polynomial degrees between one and three for the velocity and temperature, and between zero and two for the pressure. All calculations were initialized with a zero velocity and pressure field, and with a temperature equal to one in the whole domain. All calculations were performed in a single core. The convergence criteria of the nonlinear solver is set to 10^{-8} for both solvers. The under-relaxation factors for the SIMPLE algorithm are set for all calculations to 0.8, 0.5 and 1.0 for the velocity, pressure and temperature, respectively.

In Figure 5.13, a comparison of the runtimes from both solvers is presented. It is evident that the runtimes of the SIMPLE algorithm are generally higher for almost all the cases studied. Only for systems with a small number of cells does the solver using the SIMPLE algorithm outperform the XNSEC solver. Additionally, it is observed that the runtimes are comparable only for low polynomial degrees. Furthermore, it is noticeable that the runtimes are similar only for low polynomial degrees. It can be observed how the runtime of the simulations with the XNSEC code seems to scale linearly with the polynomial degree. In the case of the SIMPLE solver, the scaling is much more unfavourable, and the runtime increases dramatically as the polynomial degree increases. Obviously, the under-relaxation parameters used within the SIMPLE algorithm have an influence on the calculation times and an appropriate selection of them could decrease the runtimes. This is a clear disadvantage, since the adequate selection of under-relaxation factors is highly problem dependent and requires previous expertise from the

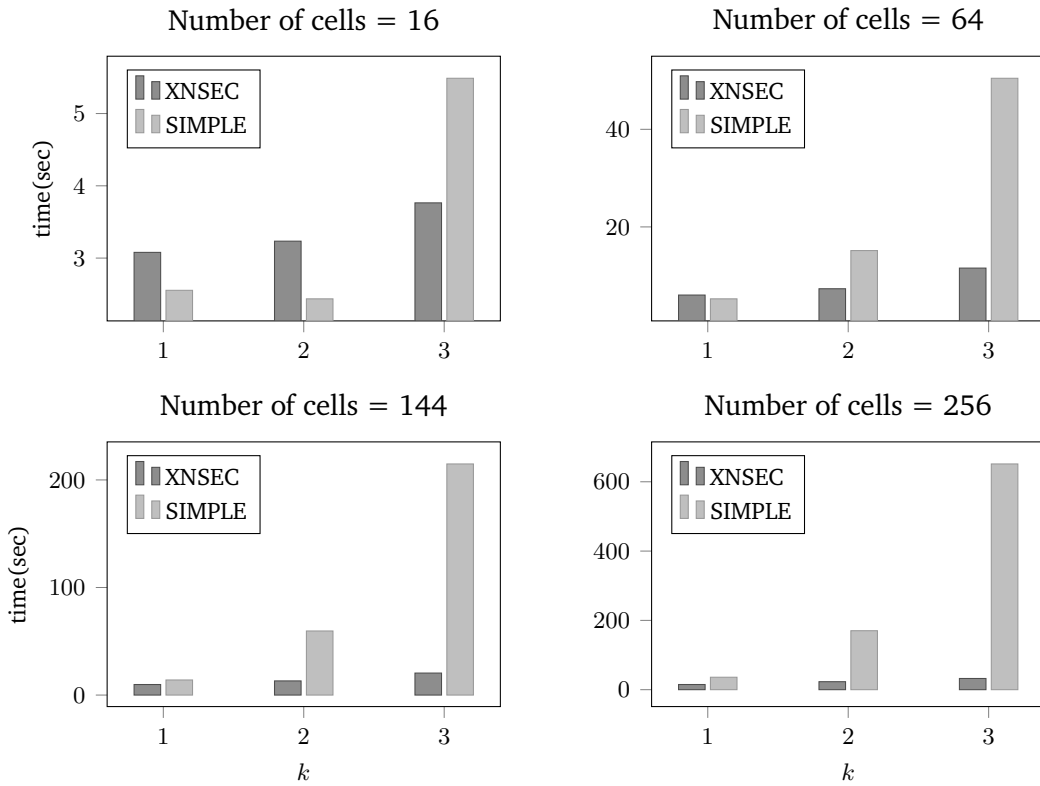


Figure 5.13: Runtime comparison of the DG-SIMPLE solver and the XNSEC solver for the Couette flow with vertical temperature gradient for different polynomial degrees k and number of cells.

user. On the other hand, the globalized Newton method used by the XNSEC solver avoid this problem by using a more sophisticated method and heuristics in order to find a better path to the solution, which does not require user-defined parameters.

5.2.3 Differentially heated cavity problem

The differentially heated cavity problem is a classical benchmark case that is often used to assess the ability of numerical codes to simulate variable density flows (Paillere et al., 2000; Vierendeels et al., 2003; Tyliszczak, 2014). The test case has the particularity that deals with a closed system, where the thermodynamic pressure p_0 is a parameter that must be adjusted so that the mass is conserved. The thermodynamic pressure p_0 determines the density field, which in turn appears in the momentum equation and the energy equation, making it necessary to use an adequate algorithm to solve the system. This point presents a special difficulty for the solution, since the calculation of p_0 requires knowledge of the temperature field on the whole computational domain, inducing a global coupling of the variables.

The system is a fully enclosed two-dimensional square cavity filled with fluid. A sketch of the problem is shown in Figure 5.14. The left and right walls of the cavity have constant temperatures \hat{T}_h and \hat{T}_c , respectively, with $\hat{T}_h > \hat{T}_c$, and the top and bottom walls are adiabatic. A gravity field induces fluid movement because of density differences caused by the difference in temperature between the hot and cold walls. The natural convection phenomenon

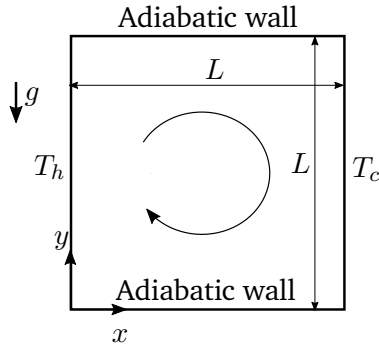


Figure 5.14: Schematic representation of the differentially heated cavity problem.

is characterized by the Rayleigh number, defined as

$$\text{Ra} = \text{Pr} \frac{\hat{g}\hat{\rho}_{\text{ref}}^2(\hat{T}_h - \hat{T}_c)\hat{L}_{\text{ref}}^3}{\hat{T}_{\text{ref}}\hat{\mu}_{\text{ref}}^2}, \quad (5.9)$$

For small values of Ra, conduction dominates the heat transfer process, and a boundary layer covers the entire domain. On the other hand, large values of Ra represent a flow dominated by convection. When the number Ra increases, a thinner boundary layer is formed. Following Vierendeels et al. (2003), a reference velocity for buoyancy-driven flows can be defined as

$$\hat{u}_{\text{ref}} = \frac{\sqrt{\text{Ra}}\hat{\mu}_{\text{ref}}}{\hat{\rho}_{\text{ref}}\hat{L}_{\text{ref}}}. \quad (5.10)$$

The Rayleigh number is then related to the Reynolds number according to

$$\text{Re} = \sqrt{\text{Ra}}. \quad (5.11)$$

Thus, it is sufficient to select a Re number in the simulation, fixing the value of the Ra number. The driving temperature difference $(\hat{T}_h - \hat{T}_c)$ appearing in Equation (5.9) can be represented as a nondimensional parameter:

$$\varepsilon = \frac{\hat{T}_h - \hat{T}_c}{2\hat{T}_{\text{ref}}}. \quad (5.12)$$

Using these definitions, the Froude number can be calculated as

$$\text{Fr} = \sqrt{\text{Pr}2\varepsilon}. \quad (5.13)$$

The average Nusselt number is defined for a given wall Γ as

$$\text{Nu}_\Gamma = \frac{1}{T_h - T_c} \int_\Gamma k \frac{\partial T}{\partial x} dy. \quad (5.14)$$

The results of the XNSEC solver are compared with those of the reference solution for $\hat{T}_{\text{ref}} = 600\text{K}$ and $\varepsilon = 0.6$. All calculations assume a constant Prandtl number equal to 0.71. The dependence of viscosity and heat conductivity on temperature is calculated using Sutherland's law (Equation (2.29)). The nondimensional length of the cavity is $L = 1$. The nondimensional temperatures T_h and T_c are set to 1.6 and 0.4, respectively. The nondimensional equation

of state (Equation (2.26)) depends only on the temperature (not on the mass fractions) and reduces to

$$\rho = \frac{p_0}{T}. \quad (5.15)$$

The thermodynamic pressure p_0 in a closed system must be adjusted to ensure mass conservation. For a closed system is given by

$$p_0 = \frac{\int_{\Omega} \rho_0 dV}{\int_{\Omega} \frac{1}{T} dV} = \frac{m_0}{\int_{\Omega} \frac{1}{T} dV}, \quad (5.16)$$

where Ω represents the complete closed domain. The initial mass of the system m_0 is constant and is set $m_0 = 1.0$. Note that the thermodynamic pressure is a parameter with a dependence on the temperature of the entire domain. This makes necessary the use of an iterative solution algorithm, so that the solution obtained respects the conservation of mass. Within the solution algorithm of the XNSEC solver, Equation (5.16) is used to update the value of the thermodynamic pressure after each Newton iteration.

Comparison of results with the benchmark solution

Here a comparison of the results obtained with the XNSEC solver and the results presented in the work of Vierendeels et al. (2003) is made. Vierendeels et al. (2003) solved the fully compressible Navier-Stokes equations on a stretched grid with 1024×1024 using a finite-volume method with quadratic convergence, providing very accurate results that can be used as reference. The benchmark results are presented for $\text{Ra} = \{10^2, 10^3, 10^4, 10^5, 10^6, 10^7\}$. In this range of Rayleigh numbers, the problem has a steady-state solution. The cavity is represented by the domain $[0, 1] \times [0, 1]$. For all calculations in this subsection, the simulations are done with a polynomial degree of four for both velocity components and temperature and three for the pressure. The mesh is in an equidistant 128×128 mesh.

Preliminary calculations showed that for cases up to $\text{Ra} = 10^5$ the solution of the system using Newton's method presented in Section 4.3.3 is possible without further modifications, while for higher values the algorithm couldn't find a solution and stagnates after certain number of iterations. For this particular case a limit of 100 Newton iterations was set. The homotopy strategy mentioned in Section 4.4.1 is used to overcome this problem and obtain solutions for higher Rayleigh numbers. Here, the Reynolds number is selected as the homotopy parameter and is continuously increased until the desired value is reached.

In Figure 5.15 the streamlines corresponding to the different simulations are shown. It is apparent that for an increasing Rayleigh number the flow behaviour becomes more complex. While for low Ra numbers the flow exhibits just one vortex, for higher Ra number more vortex like structures appear. It is also possible to observe how an increasing Ra value creates a thinner boundary layer.

In Figures 5.16 to 5.18 the temperature and velocity profiles across the cavity for different Rayleigh numbers are shown. The profiles calculated with the XNSEC solver agree closely to the benchmark solution.

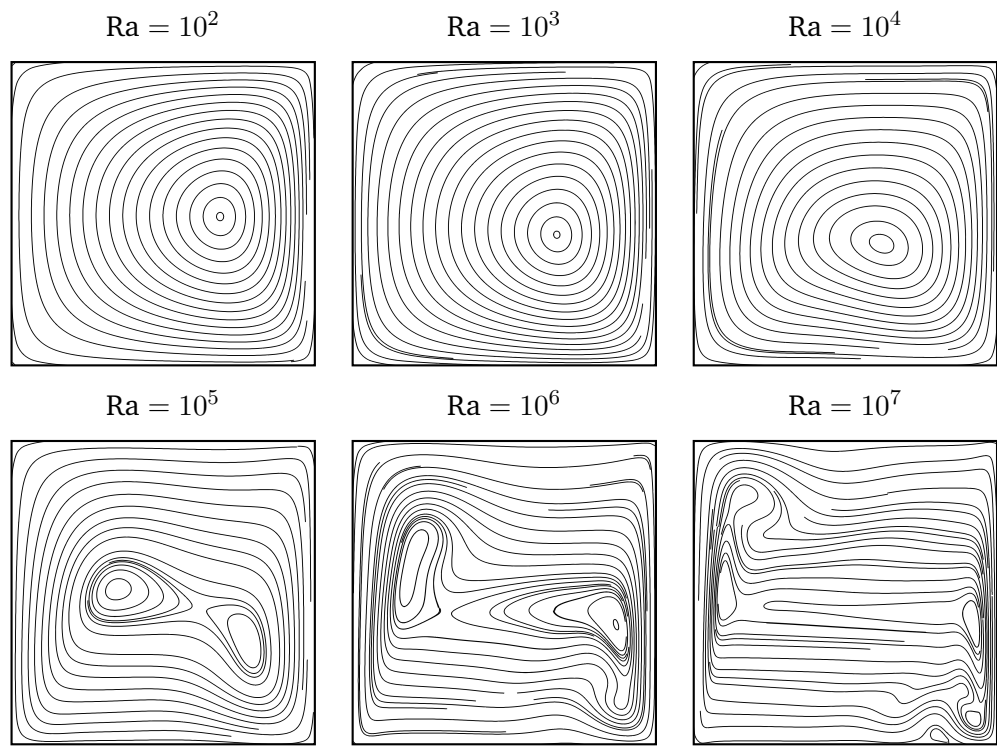


Figure 5.15: Streamlines of the heated cavity configuration with $\epsilon = 0.6$ for different Reynold numbers.

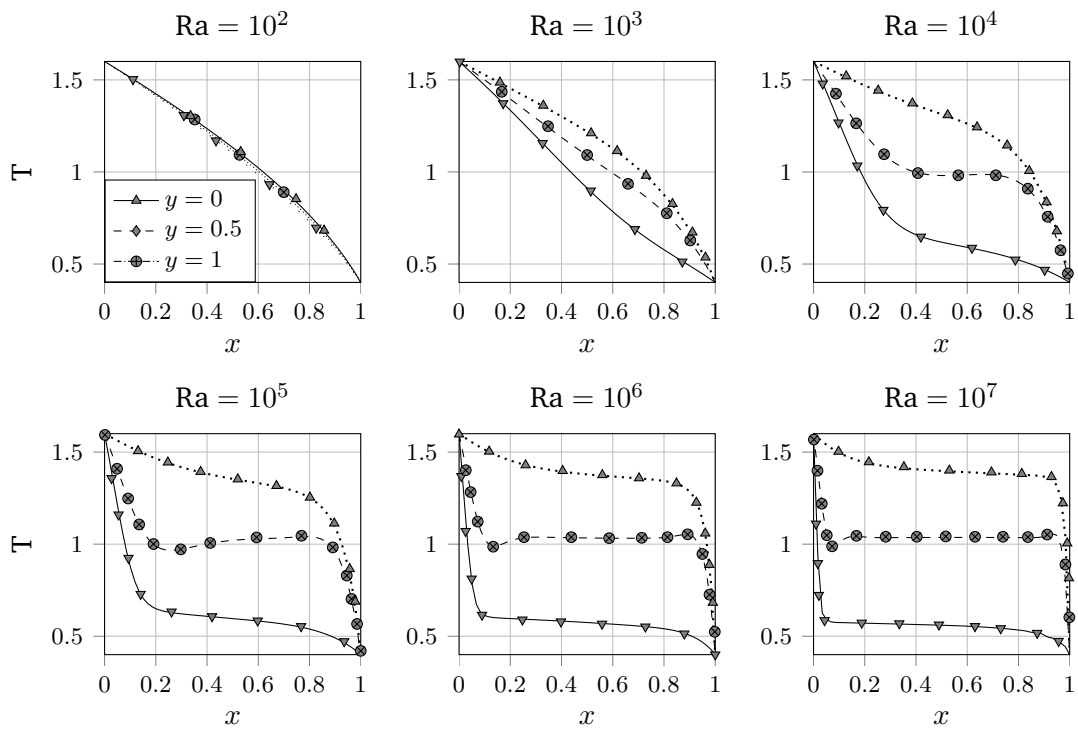


Figure 5.16: Temperature profiles for the differentially heated square cavity along different vertical levels. Solid lines represent the XNSEC solver solution and marks the benchmark solution.

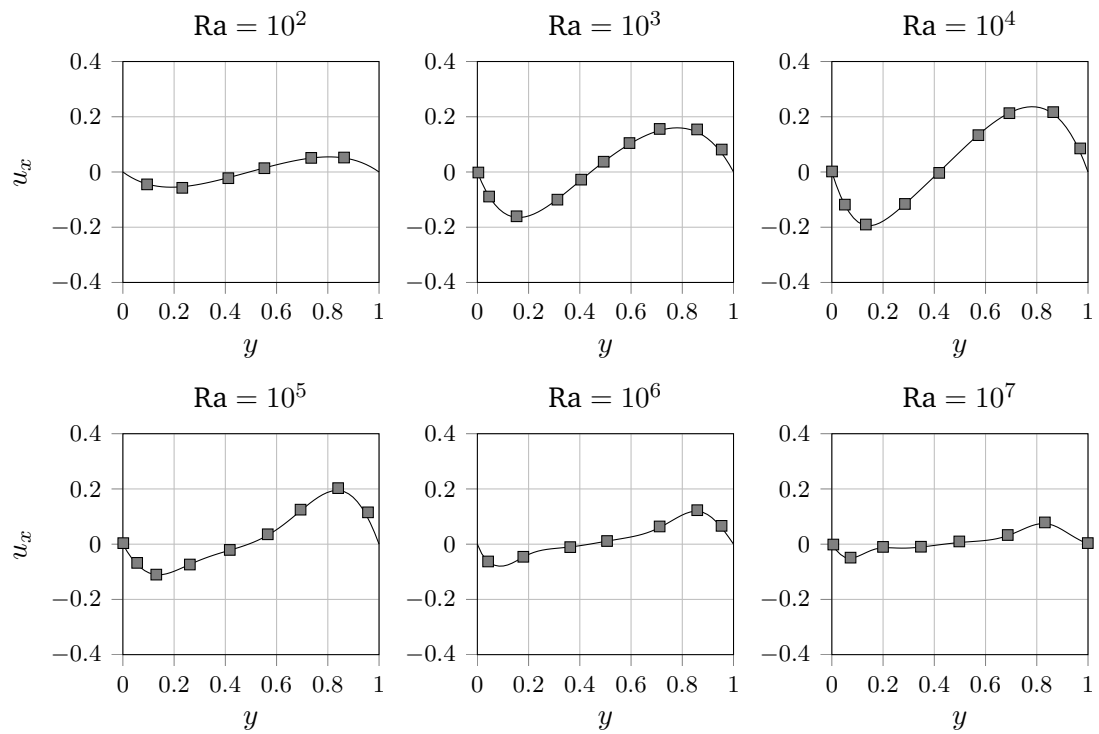


Figure 5.17: Profiles of the x-velocity component for the differentially heated square cavity along the vertical line $x = 0.5$. Solid lines represent the XNSEC solver solution and marks the benchmark solution.

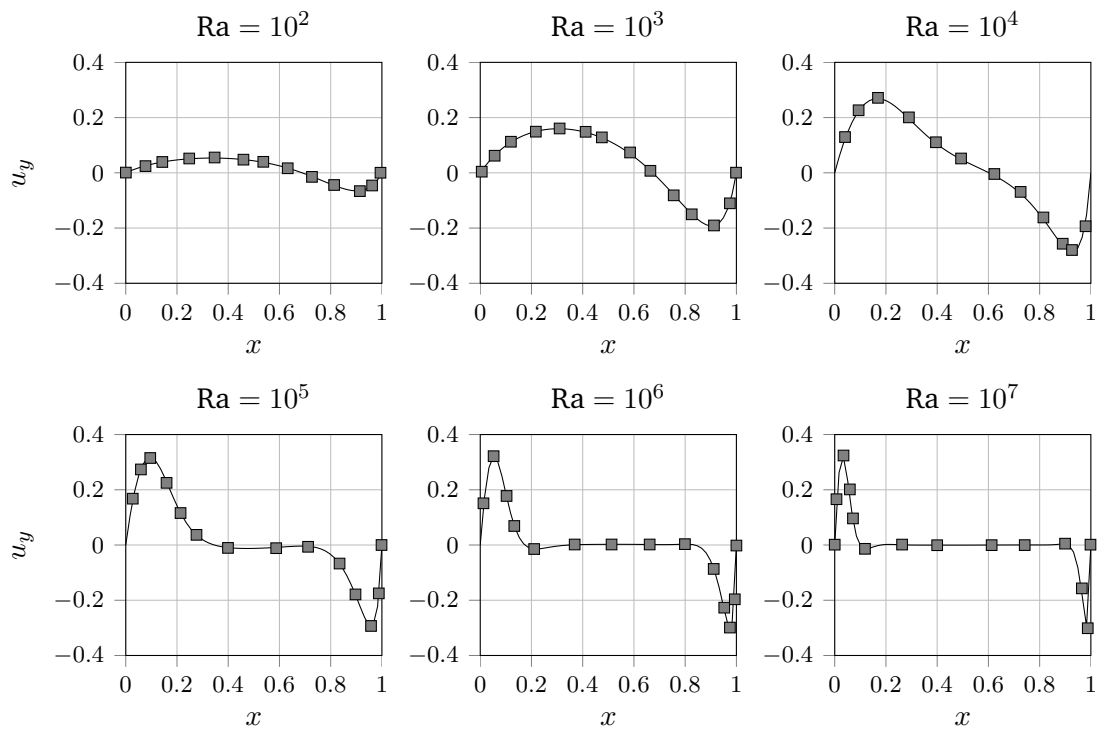


Figure 5.18: Profiles of the y-velocity component for the differentially heated square cavity along the horizontal line $y = 0.5$. Solid lines represents the XNSEC solver solution and marks the benchmark solution.

Rayleigh	p_0	$p_{0,\text{ref}}$	Nu_h	Nu_c	Nu_{ref}
10^2	0.9574	0.9573	0.9787	0.9787	0.9787
10^3	0.9381	0.9381	1.1077	1.1077	1.1077
10^4	0.9146	0.9146	2.2180	2.2174	2.2180
10^5	0.9220	0.9220	4.4801	4.4796	4.4800
10^6	0.9245	0.9245	8.6866	8.6791	8.6870
10^7	0.9225	0.9226	16.2411	16.1700	16.2400

Table 5.2: Comparison of calculated Nusselt numbers of the hot and cold wall and Thermodynamic pressure p_0 reported values by Vierendeels et al. (2003) for the differentially heated cavity.

A comparison of the thermodynamic pressure and the Nusselt numbers with the benchmark solution was also made. The results are shown in Table 5.2. The thermodynamic pressure is obtained from Equation (5.16), and the average Nusselt number is calculated with Equation (5.14). The results obtained with the XSEC solver agree very well with the reference results, as can be seen for the thermodynamic pressure, which differs at most in the fourth decimal place.

Note that the average Nusselt number of the heated wall Nu_h and the Nusselt number of the cold wall Nu_c are different. While for an energy conservative system Nu_h and Nu_c should be equal, for the DG-formulation this is not the case, since conservation is only ensured locally and the global values can differ. This discrepancy can be seen as a measure of the discretization error of the DG formulation and should decrease as the mesh resolution increases. As the Rayleigh number grows, the discrepancy becomes larger, hinting that, at such Rayleigh numbers, the mesh used is not refined enough to adequately represent the thin boundary layer and more complex flow structures appearing in high-Rayleigh number cases. This point will be discussed in the next section.

Convergence study

An h -convergence study of the XSEC solver was conducted using the heated cavity configuration. Calculations were performed for polynomial degrees $k = 1, 2, 3, 4$ and equidistant regular meshes with, respectively, 8×8 , 16×16 , 32×32 , 64×64 , 128×128 and 256×256 elements. The L^2 -Norm was used to calculate errors against the solution in the finest mesh. The results of the h -convergence study for varying polynomial orders k are shown in Figure 5.19. It is observed how the convergence rates scale approximately as $k + 1$. Interestingly, for $k = 2$ the rates are higher than expected. On the other hand, some degeneration is observed in convergence rates for $k = 4$. This strange behavior can be explained if one considers that the heated cavity presents a singular behavior at the corners (similar to the problem previously exposed for the lid-driven cavity), which causes global pollution in the convergence behavior of the algorithm.

As discussed in the previous section, the difference in the average values of the Nusselt number on the hot wall Nu_h and the cold wall Nu_c is a direct consequence of the spatial discretization error and should decrease for finer meshes. In Figure 5.20 the convergence behavior of the Nusselt number is presented for different polynomial degrees k , different number of elements and for two Rayleigh numbers. As expected, it can be observed that this discrepancy is smaller when a larger number of elements is used. It can also be seen that

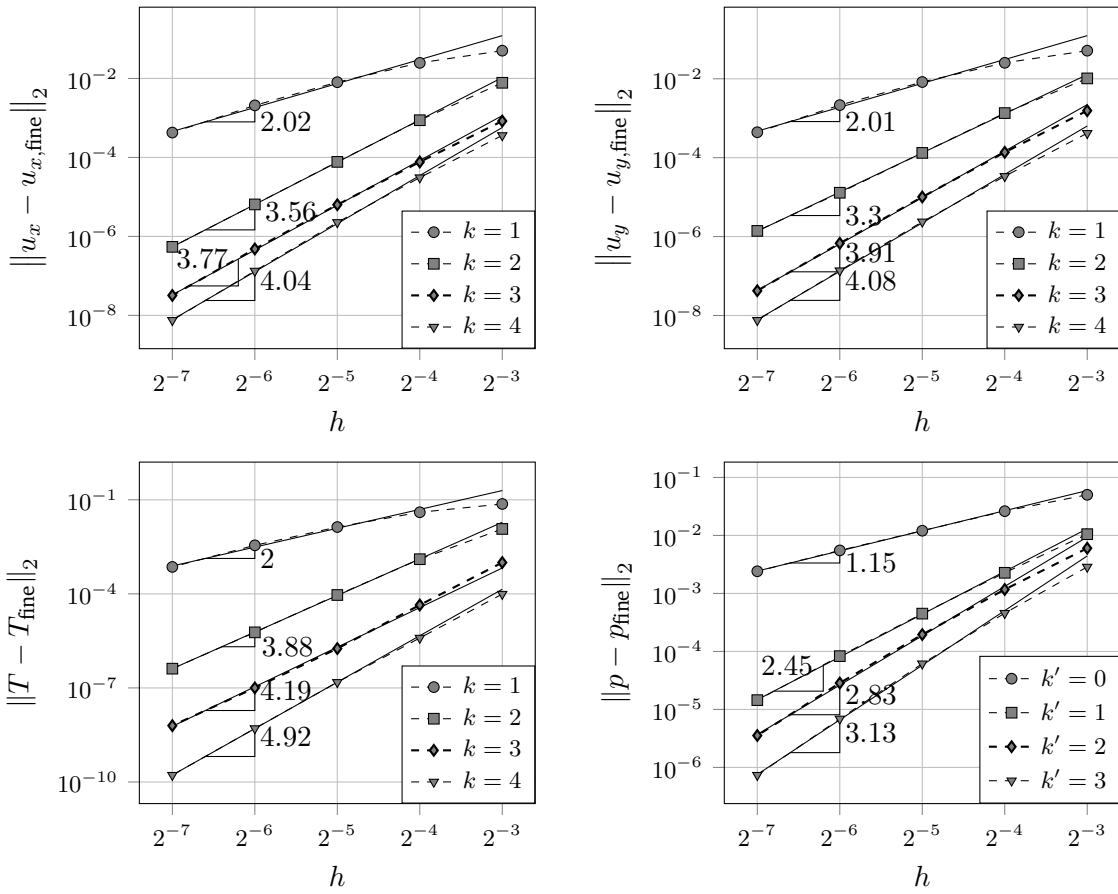


Figure 5.19: Convergence study of the differentially heated cavity problem for $\text{Ra} = 10^3$.

Nu_h reaches the expected solution of cells for a much smaller number of elements. This can be explained if one thinks that more complex phenomena take place near the cold wall (see Figure 5.15), which makes necessary a finer mesh resolution in that area.

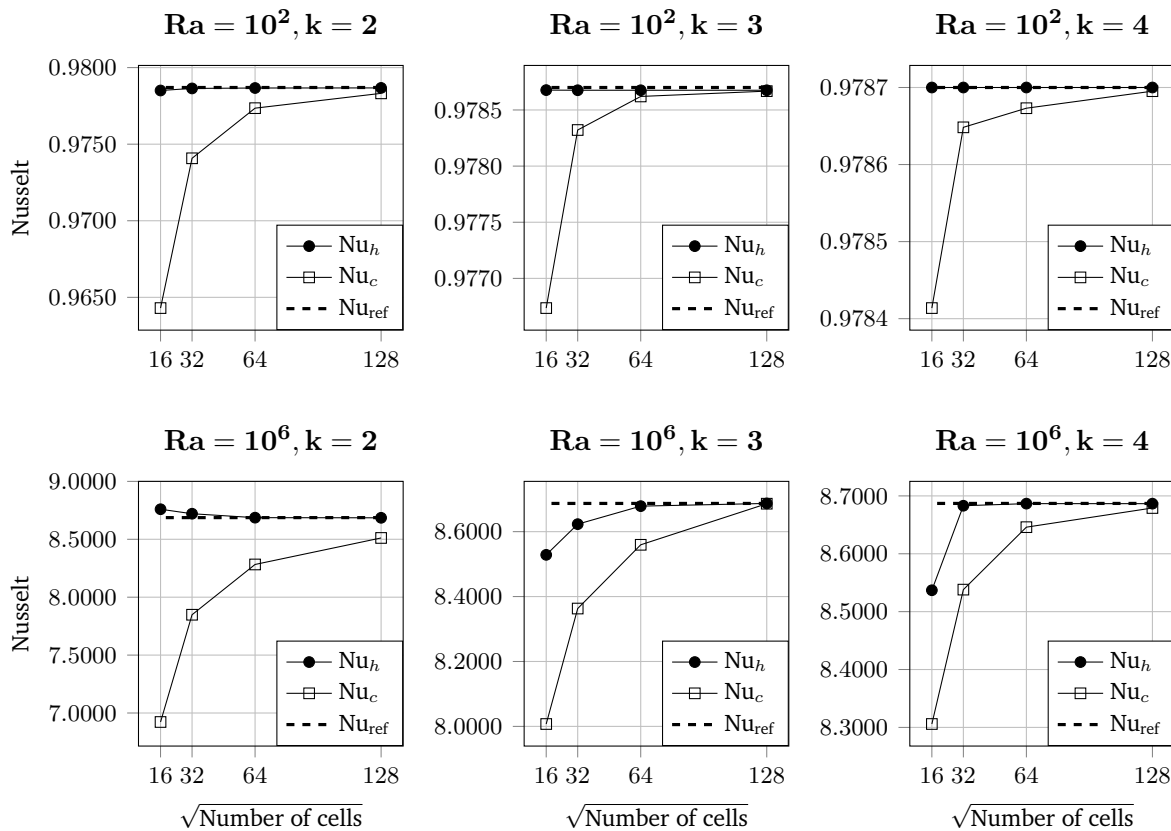


Figure 5.20: Nusselt numbers of the differentially heated square cavity at the hot wall (Nu_h) and the cold wall (Nu_c) for different number of cells and polynomial order k . The reference values from Vierendeels et al. (2003) are shown with dashed lines.

Influence of the penalty factor

A point not still discussed is the choice of the safety parameter η_0 of the penalty terms from the SIP discretization (see Section 3.2.3). Table 5.3 shows results obtained for $\text{Ra} = 10^3$, for different polynomial degrees and penalty safety factor. For the tests presented here, the penalty terms of the diffusive terms from the momentum and energy equations are considered equal. Furthermore, the number of elements in the mesh is selected in such a way that the number of degrees of freedom remains approximately constant for each simulation.

It is possible to see that the penalty safety factor (and therefore the penalty term) can have a great influence on the solution. If the value chosen is very small, as in the case of the table for $\eta_0 = 0.01$, the algorithm is not able to find a solution. On the other hand, if the chosen value is too high, the error also increases. It can be concluded that an optimal value for the penalty factor exists.

It is also noticeable that, maintaining a constant penalty safety factor, increasing the polynomial degree for an approximately constant number of DOFs gives an improvement in the results compared to the literature. Although for this testcase the effect of the penalty factor on the solution is not very large, the effect could be considerable, especially when dealing with more complex geometries and coarser meshes. The value $\eta_0 = 4$ has shown to be a value that

η_0	k	DOFs	Nu_c	$\frac{Nu_c - Nu_{c,ref}}{Nu_{c,ref}} \times 10^2$	p_0	$\frac{p_0 - p_{0,ref}}{p_{0,ref}} \times 10^4$
0.01	2	6804	0.549483*	50.39424	0.899757*	408.7292
	3	7056	0.722593*	34.76637	0.936085*	21.48436
	4	6655	-0.50954*	146	1.016691*	837.7683
1	2	6804	1.090047	1.593667	0.938192	0.980674
	3	7056	1.102072	0.508037	0.938057	0.453674
	4	6655	1.105225	0.22348	0.938046	0.570494
4	2	6804	1.089332	1.65817	0.93843	3.521926
	3	7056	1.102261	0.491027	0.938076	0.25384
	4	6655	1.105359	0.211372	0.938047	0.561709
16	2	6804	1.08694	1.874166	0.939109	10.75641
	3	7056	1.102266	0.490563	0.938124	0.251627
	4	6655	1.105439	0.204153	0.93805	0.537265

Table 5.3: Thermodynamic pressure and cold-side Nusselt number for different penalty safety factors in a heated cavity with $Ra = 10^3$. Values marked with an asterisk are from problems not converged after 100 iterations.

gives stability to the scheme and is used for all simulations in this thesis, as already has been done in many works (Krause and Kummer, 2017; Kummer, 2017; Smuda, 2021) and is used for all calculations in this work.

The results presented in this section allows to conclude that the implemented solver is capable of dealing with flows with variable densities, and in particular in closed spaces. Additionally, it was observed that even for this complex test, convergence properties close to those expected from the DG method are obtained. Until this point only systems with a steady state solution were treated. Later in Section 5.2.4 the ability of the solver to compute flows with varying densities in non-steady state will be shown.

5.2.4 Flow over a circular cylinder

A further thest case of the XSEC solver is the simulation of flow over a circular cylinder. The results shown section are based on the work by Miao (2022)

The simulation of a 2D flow over an obstacle exhibits different flows states depending on the Reynolds number. For low Reynolds numbers, the flow is laminar and stationary. When the Reynolds number reaches a critical value, the flow becomes non-stationary and eventually turbulent. In particular, for $50 \leq Re \leq 160$ the behavior of the fluid is laminar with an non-stationary periodic character, and the well-known vortex shedding phenomenon appears (Sharma and Eswaran, 2004). In this section the ability of the XSEC solver for dealing with isothermal and non-isothermal unsteady flow will be assessed. This is done by calculating the Strouhal number, average drag and lift coefficients and the Nusselt number and comparing them to reference solutions.

Set-up

Figure 5.21 shows the geometry of the problem. In the center of the domain is located a heated cylinder of diameter $d = 1$, which is subjected to a flow of constant velocity magnitude. The size of the computational domain is chosen as $D = 59d$, which is large enough so that the

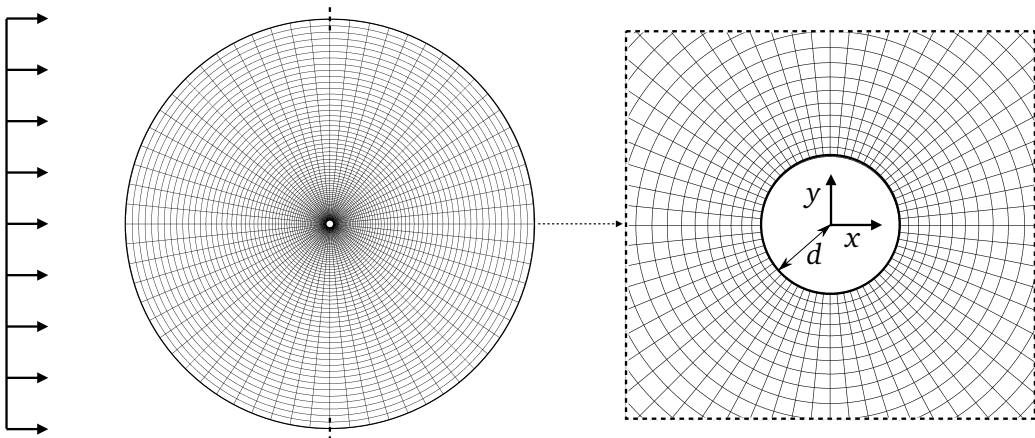


Figure 5.21: Schematic representation of the heated circular cylinder. Figure adapted from (Miao, 2022)

outlet boundary conditions do not influence the solution. The left half of the boundaries of the computational domain corresponds to a velocity inlet with constant velocity $(u, v) = (1, 0)$ and temperature $T = T_\infty$. The right half of the domain corresponds to a pressure outlet. The boundary condition corresponding to the heated cylinder is a no-slip wall defined with $(u, v) = (0, 0)$, and with a constant temperature $T = T_h$. The system is an open system, and the thermodynamic pressure has a constant value set to $p_0 = 1$.

As mentioned, a isothermal and non-isothermal system is considered in this section. A reference temperature of $\hat{T}_{\text{ref}} = 298.15 \text{ K}$ is selected. The conditions for the velocity inlet are for the isothermal case a dimensionless temperature of $T_h = 1.0$ and $T_\infty = 1$, while for the non-isothermal $T_h = 1.5$ and $T_\infty = 1.0$. A Reynolds number of 100 is used, for which the flow is known to be unsteady and periodic. Gravity effects are taken as negligible. The Prandtl number has a constant value of $\text{Pr} = 0.71$ and the heat capacity ratio is $\gamma = 1.4$. The transport parameters are calculated with Sutherland's law which is given by Equation (2.29) and the equation of state for the density is Equation (2.26).

For all calculations a polynomial degree of order three is used for both velocity components and the temperature, and two for pressure. In this simulation a curved mesh consisting of 64 elements in the radial direction and 64 elements in the angular direction is used. The use of a curved mesh for this problem was done primarily to adequately represent the geometry of the cylinder. Another possibility could have been to use a method such as a Immersed Boundary Method -which is also supported in the BoSSS-framework-, but it is beyond the scope of this work.

One point to note regarding the use of curved meshes within the DG method (and in all High-order methods), is that special care has to be taken in the representation of curved elements in order to use correctly quadrature rules (Bassi and Rebay, 1997). This is critical to preserve the convergence properties of DG-methods. In particular, since the highest degree of the polynomials used in this simulation is three, elements of the bi-cubic type are used, where 16 nodes are used per element for the discretization for a two-dimensional element. Furthermore, the time discretization is performed with a BDF-3 scheme, and the time derivative of the continuity equation is calculated with a second order backward difference scheme (see Section 3.1.3). The simulation time corresponds to $t = 100$, and constant timesteps of $\Delta t = 0.2$

are used. The initial conditions are

$$u(t=0) = 1 + u^{\text{vortex}}, \quad (5.17\text{a})$$

$$v(t=0) = 0 + v^{\text{vortex}}, \quad (5.17\text{b})$$

$$T(t=0) = 1, \quad (5.17\text{c})$$

$$p(t=0) = 0. \quad (5.17\text{d})$$

Here, u^{vortex} and v^{vortex} are the velocity component of a vortex field of radius r , strength a and central point (x^o, y^o) defined by

$$u^{\text{vortex}}(x, y) = \begin{cases} -a(y - y^o) & \text{if } \sqrt{(x - x^o)^2 + (y - y^o)^2} \leq r \\ 0 & \text{if } \sqrt{(x - x^o)^2 + (y - y^o)^2} > r \end{cases} \quad (5.18\text{a})$$

$$v^{\text{vortex}}(x, y) = \begin{cases} a(x - x^o) & \text{if } \sqrt{(x - x^o)^2 + (y - y^o)^2} \leq r \\ 0 & \text{if } \sqrt{(x - x^o)^2 + (y - y^o)^2} > r \end{cases} \quad (5.18\text{b})$$

The reason for placing a vortex in the initial conditions is to include a perturbation in the system which triggers the vortex shredding phenomenon. The vortex moves with the flow and is eventually advected from the calculation domain. Specifically, for this simulation, a vortex of radius $r = 1$ and strength $a = 1$ is placed at $(x^o, y^o) = (2, 0)$. It is worth mentioning that the inclusion of the vortex in the initial conditions is not imperative to make the vortex-shedding phenomenon emerge, but it is a way to accelerate its appearance. For the range of Reynolds numbers mentioned, even instabilities of the numerical method should be enough to cause the phenomenon to arise, but in a much slower way.

The variables lift coefficient C_L , drag coefficient C_D , Strouhal number St , and Nusselt number Nu are calculated and compared with reference results. These characteristic quantities are defined as

$$C_L = \frac{2F_L}{\rho_\infty u_\infty^2 d} \quad (5.19)$$

$$C_D = \frac{2F_D}{\rho_\infty u_\infty^2 d} \quad (5.20)$$

$$\text{St} = \frac{fd}{u_\infty} \quad (5.21)$$

$$\text{Nu} = \frac{d}{\Delta T} \frac{1}{\|\partial S\|_{\text{leb}}} \oint_{\partial S} \nabla T \cdot \mathbf{n} dS \quad (5.22)$$

F_L and F_D are the lift and drag force respectively, f is the vortex shedding frequency and $\|\partial S\|_{\text{leb}} = \pi d$ is the circumference of the cylinder.

Isothermal case.

The isothermal case results are compared with the work of Sharma and Eswaran (2004). They reported results for the case $\text{Re} = 100$ and $T_h = T_\infty$. The Strouhal number and average drag coefficient calculated with the XNSEC solver are $\text{St} = 0.1639$ and $C_{D,\text{avg}} = 1.3103$, while the reference values $\text{St} = 0.164$ and $C_{D,\text{avg}} = 1.3183$, which means a error of less than a 0.6% on both quantities. Its worth noting that preliminary calculations with a implicit Euler scheme for the discretization of the temporal terms didn't cause the vortex shedding phenomenon to appear, making necessary a scheme of higher order. This is probably due to an excess of numerical dissipation by using a low-order temporal discretization, which smooths out and removes the natural perturbation effects that trigger vortex shedding.

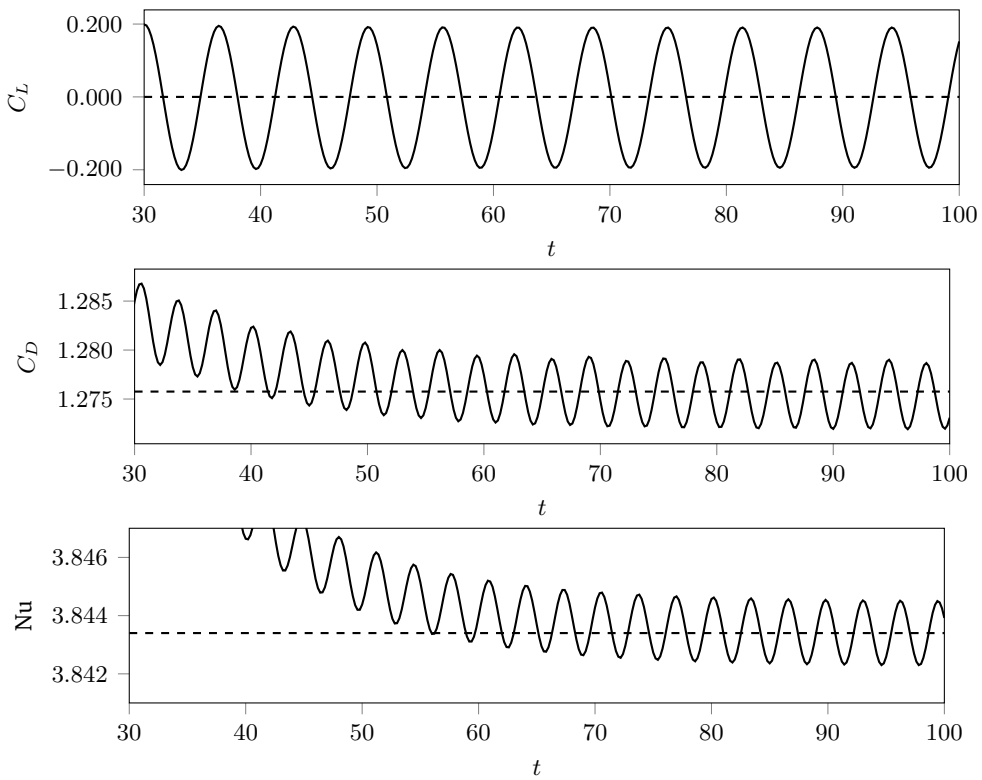


Figure 5.22: Temporal evolution of average Nusselt number, lift coefficient and drag coefficient of the heated cylinder

Non-isothermal case.

A comparison of the calculation results for the non-isothermal case was performed based on the results reported in Shi et al. (2004), Wang et al. (2000) and Hennink (2022). The temporal evolution of the characteristic quantities C_D , C_L and Nu is shown in Figure 5.22. The results agree very closely with the references. The average Nusselt number is $\text{Nu} = 3.8434$, while the reference value from Hennink (2022) is $\text{Nu} = 3.804$, which corresponds to a difference of 1.04%. The Strouhal number is $\text{St} = 0.1538$ and the references report values of $\text{St} = 0.152$ and $\text{St} = 0.1536$, a difference of approximately 1%. It is possible then to conclude that the XNSEC solver allows to simulate adequately unsteady non-isothermal flows, where the fluid properties do present a scalar dependence (in this case, on the temperature).

It is worth noting that in this test-case the temperature changes causes only a moderate variation in the density. As will be seen later, the temporal term appearing in the continuity equation, as implemented in the present solver, is problematic in the case of larger density differences (Knijker, 2011), as it is a cause of numerical instabilities.

5.2.5 Rayleigh-Bénard Convection

The Rayleigh-Bénard convection problem is a configuration similar to the heated cavity (see Section 5.2.3) as the flow is also induced by buoyancy effects. The configuration consists of a fluid located between two horizontal plates maintained at different temperatures, with the temperature of the lower plate being higher than that of the upper plate. It is known that

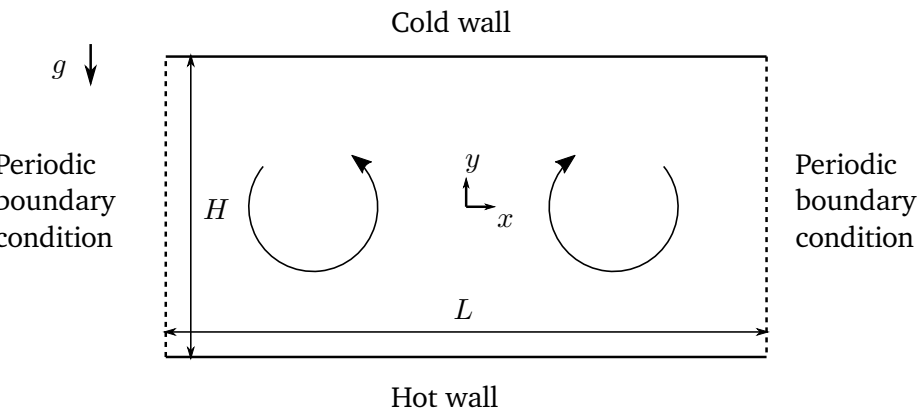


Figure 5.23: Geometry of the Rayleigh-Bénard convection problem. Convection rolls are sketched.

under a certain Rayleigh number the flow presents a macroscopically stable behavior and the heat is simply transferred by conduction. When the Rayleigh number exceeds a certain critical value Ra_{crit} , the system becomes unstable, which causes a perturbation of the system to give rise to fluid motion, creating the so-called convection cells, also usually referred to as Bénard cells.

In the following sections two aspects of this situation will be discussed by making use of different types of boundary conditions on the sides of the domain. First in Section 5.2.5 periodic boundary conditions are used, which allows studying a single pair of convection rolls and to calculate numerically the critical value Ra_{crit} , which is compared with theoretical values. Subsequently, in Section 5.2.5 a transient simulation of this configuration is performed by using pressure-outlet boundary conditions. The results shown in this section are taken from the work by Miao (2022).

Periodic boundary conditions

In this section the fluid behavior will be analysed by studying a system where a single convection cell appears. Making use of linear stability theory for the governing equations under the Boussinesq assumption, it is possible to determine that for a system with rigid boundaries the critical Rayleigh number is $\text{Ra}_{\text{crit}} = 1707.762$ (Chandrasekhar, 1961). Moreover, the dimensionless wave number is $a_c = 3.117$, which implies that the convective rolls develop at an aspect ratio of $2\pi/a_c = 2.016$. For the simulations presented in this section an aspect ratio of $L/H = 2$ is used, as is done by Kao and Yang (2007). The geometry and boundary conditions of the analysed problem can be found in Figure 5.23. The upper wall corresponds to a no-slip wall that is maintained at a constant temperature T_c . Similarly, the bottom wall is also a no-slip wall with a temperature T_h , where $T_h > T_c$. The boundary conditions on the left and right of the computational domain are periodic boundary conditions. Gravity has only one component in the negative direction of y .

For the range of Rayleigh numbers treated here, the simulations are steady state. For all simulations in this section a regular Cartesian grid consisting of 32×64 cells, with dimensionless lengths $L = 2$ and $H = 1$ was used. The polynomial degree of both velocity components and temperature is four, and for pressure it is three. An open system is assumed, and $p_0 = 1.0$ throughout the simulation.

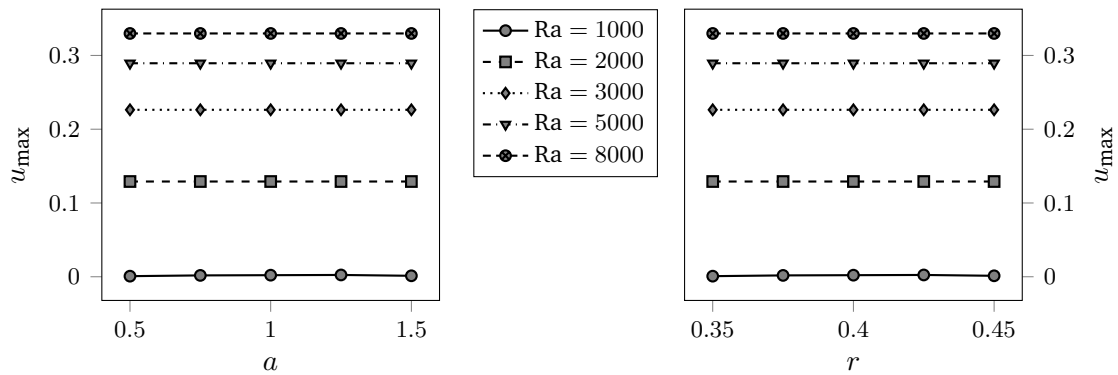


Figure 5.24: Maximum x-velocity in the Rayleigh-Bénard convection configuration for different a and r .

First, the stability of the XNSEC solver is studied by determining the critical value Ra_{crit} . As mentioned above, the theoretical value $\text{Ra}_{\text{crit}} = 1707.762$ was determined using the Boussinesq assumption in the governing equations, which, unlike the low-Mach equations, is only valid if the variation of temperature within the system is very small. For this reason, an analysis is performed for a dimensionless temperature difference $\epsilon = (T_h - T_c)/(T_h + T_c) = 0.0001$, meaning $T_h = 1.0001$ and $T_c = 0.9999$. The reference temperature is chosen to be $\hat{T}_{\text{ref}} = 600 \text{ K}$. Since the XNSEC solver is based on the low-Mach equations, this choice of low temperature difference allows comparing the present results with those obtained analytically using the Boussinesq approximation. The definition of the dimensionless numbers as well as the reference velocity are exactly the same as those mentioned in Section 5.2.3. The transport coefficients are calculated with Sutherland's law.

Similarly to the case discussed in Section 5.2.4, velocity fields are initialized with vortices, which are used to trigger the inherent instabilities of the studied system. In particular, two vortices with opposite directions of rotation are added. The velocity components of these are again given by Equation (5.18). The coordinates of the first vortex are $(x^o, y^o) = (-0.5, 0)$ and it has a strength $a = 1$ and a radius $r = 0.4$. For the second vortex $(x^o, y^o) = (0.5, 0)$, $a = -1$ and $r = 0.4$ are selected. The initial conditions are

$$u(t = 0) = 1 + u^{\text{vortex-left}} + u^{\text{vortex-right}}, \quad (5.23a)$$

$$v(t = 0) = 0 + v^{\text{vortex-left}} + v^{\text{vortex-right}}, \quad (5.23b)$$

$$T(t = 0) = 1, \quad (5.23c)$$

$$p(t = 0) = -\frac{\rho y}{\text{Fr}^2}. \quad (5.23d)$$

It is worth noting that the initialization of the solver without the vortices leads the solver to a stationary solution with no fluid motion. Clearly this is a solution of the equations, but is an unstable solution.

First, a study was performed to demonstrate the independence of the steady-state solution from the chosen initial conditions. This is demonstrated in Figure 5.24, where for a given Rayleigh number the maximum velocity obtained inside the system is shown, varying the strength a or the radius r of the vortices. It is apparent that the case $\text{Ra} = 1000$ does not exhibit a macroscopic fluid motion, while $\text{Ra} = 2000$ does. This points to the fact that the critical value is effectively in this range.

Subsequently a series of simulations were performed with $a = 0.5$ and $r = 0.4$ were done to

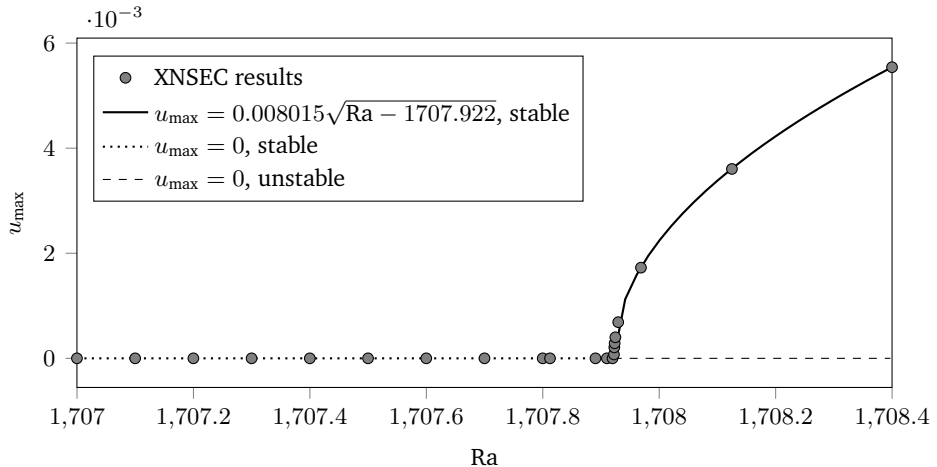


Figure 5.25: Stability behavior of the Rayleigh-Bénard convection with $\epsilon = 0.0001$.

find the critical Rayleigh value. By using a bisection strategy, the critical Rayleigh was found to be $\text{Ra} = 1707.922$, as shown in Figure 5.25.

A the theoretical value for the critical Ra number can be calculated. For the case of two plates with no-slip boundaries the value corresponds to $\text{Ra} = 1707.762$ (Shishkina, 2021). The calculated value with the XNSEC solver presents a difference of only 0.009% compared with the analytical value. In addition, the proportionality $u \propto \sqrt{\text{Ra} - \text{Ra}_{\text{Ra}}}$ that is expected by analytical arguments is also obtained, in particular, $u_{\max} = 0.008015\sqrt{\text{Ra} - 1707.922}$. It is possible to conclude that, at least for small temperature differences, the low-Mach approximation has a behavior similar to that of the equations with the Boussinesq approximation.

Finally, in Figure 5.26 the temperature fields obtained with the XNSEC solver for $\epsilon = 0.5$ and $\hat{T}_{\text{ref}} = 600$ K for different Rayleigh numbers are shown. For a Ra number of 2000 -which corresponds to a value slightly higher than the critical value- the apparition of convection rolls can be appreciated. As the value increases, the fluid departs from its purely conductive state, and the fluid gets more accelerated. As this happens, more complex structures appear.

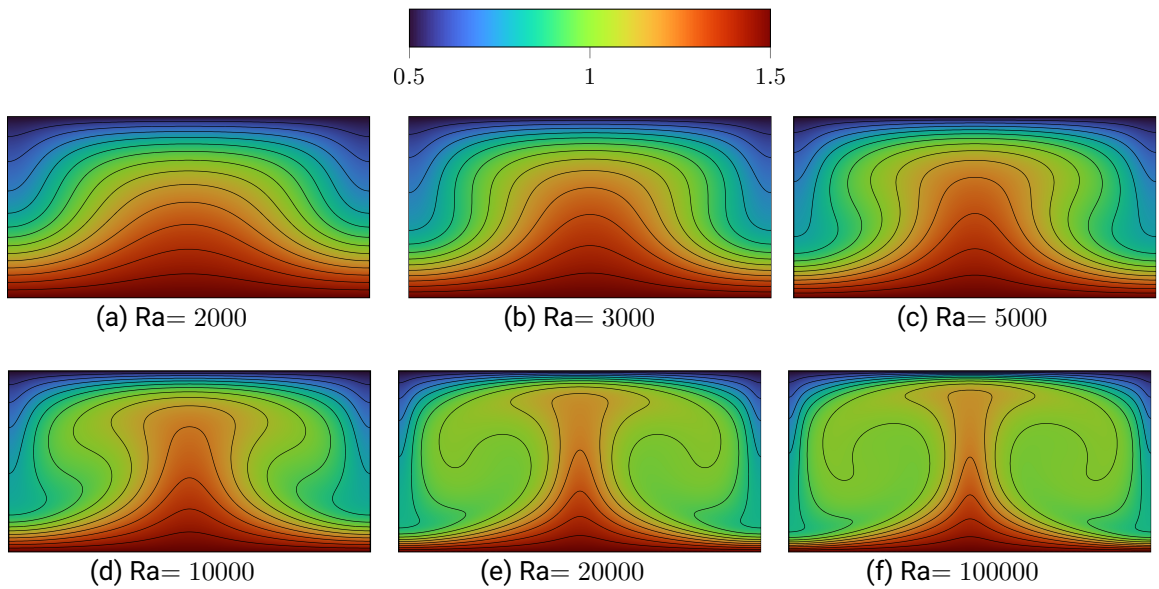


Figure 5.26: Temperature field and temperature contours of a Rayleigh-Bénard convection roll

Simulation with open boundaries

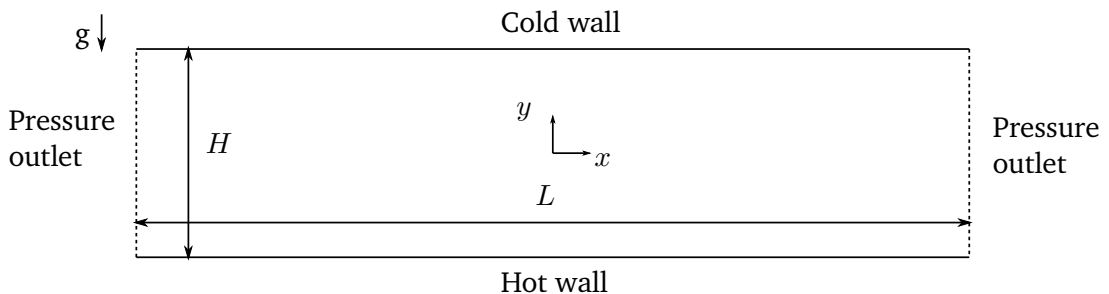


Figure 5.27: Geometry of the Rayleigh-Bénard convection with pressure outlet boundary conditions.

Finally, a transient calculation of the Rayleigh-Bénard configuration is shown. This example shall work as a test for the implementation of the time-stepping algorithm. The configuration is similar to the one described for the case with periodic boundary conditions, with the difference that the boundaries of the left and right sides are now pressure outlet boundary conditions, representing an open system. The length L of the system is chosen to be considerably longer in order to allow the apparition of multiple convection rolls. A sketch of the system is shown in Figure 5.27. The nondimensional lengths are chosen to be $H = 1$ and $L = 10$. A grid with 32×320 cells is used. The polynomial degrees for the velocity components and temperature are set to four and for the pressure to three. The time discretization is done again with a BDF-3 scheme and the calculation time is 150, using timesteps of $\Delta t = 0.5$. The temperatures are set to $T_h = 1.5$ and $T_c = 0.5$, with a reference temperature of $\hat{T}_{\text{ref}} = 600$ K. The Rayleigh number

is $\text{Ra} = 5659$, which is above the critical value. The initial conditions are chosen to be

$$u(t=0) = 0, \quad (5.24\text{a})$$

$$v(t=0) = 0, \quad (5.24\text{b})$$

$$T(t=0) = 1, \quad (5.24\text{c})$$

$$p(t=0) = -\frac{\rho y}{\text{Fr}^2}. \quad (5.24\text{d})$$

Note that no vortex is included in the initial conditions and that only a fluid at rest is considered. A perturbation effect caused by the pressure outlet boundaries triggers the movement of the fluid. At the first stages of the simulation the perturbations induce a vortex-like structure close to the left and right boundaries, and start gradually filling the whole domain, finally reaching a steady solution. This can be seen in Figure 5.28. Clearly, in the center of the domain (far away from the outlet boundary conditions), the structure of the solution is very similar to the ones shown in the last subsection. In fact, if the domain length is chosen sufficiently large, they should be equal.

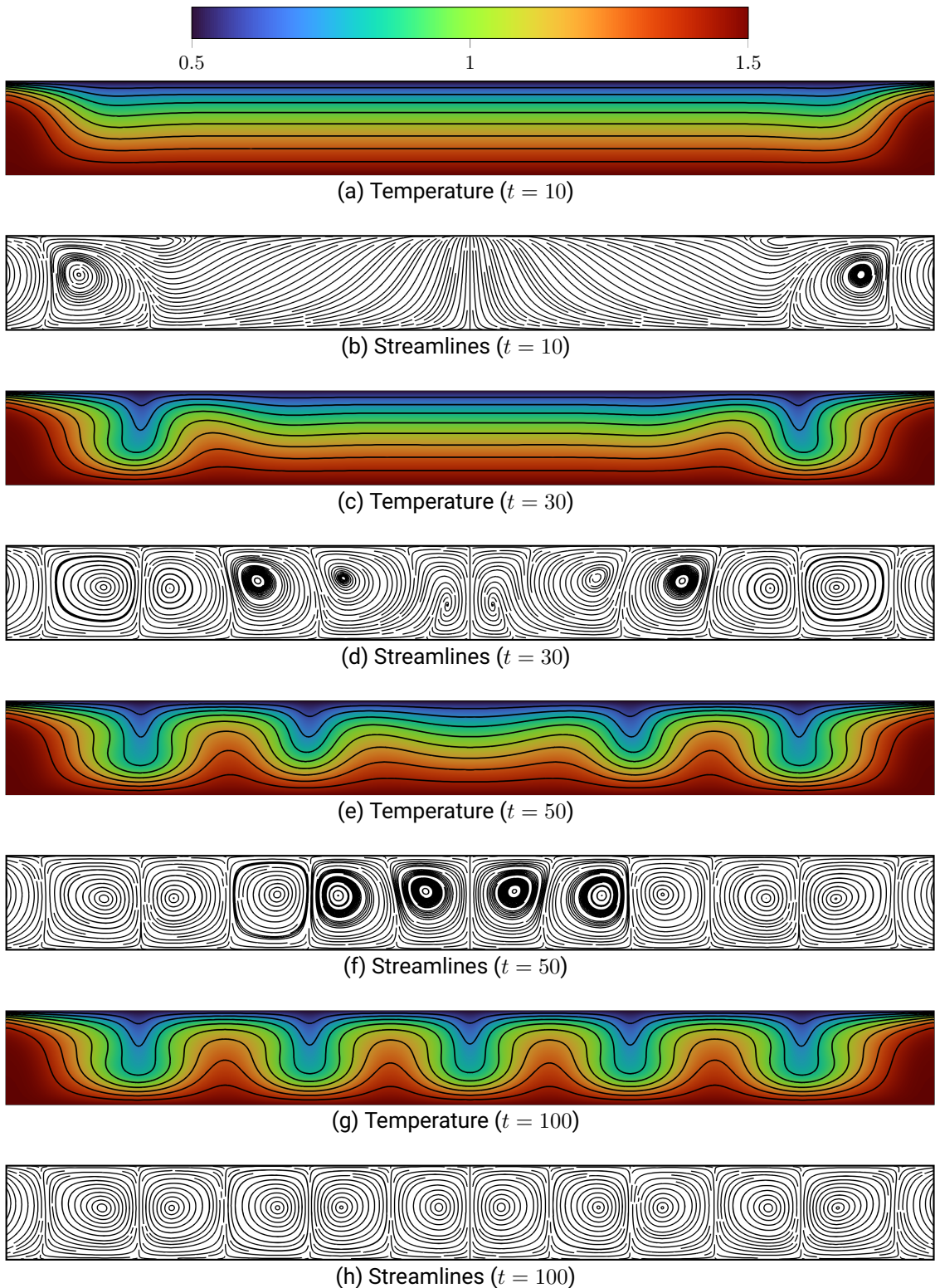


Figure 5.28: Temperature and streamlines of the Rayleigh-Bénard flow with pressure outlets.

5.3 Multi-component non-isothermal cases

Finally in this section, test cases where the whole operator presented in Chapter 3 is used are shown. The balance equations of continuity, momentum, energy and species are considered and solved in a coupled manner, together with a equation of state and expressions for the transport parameters. For all the steady state cases treated here, the solution of the flame sheet problem described in Section 2.2 is calculated first, and then this solution is used as an initial estimate for the solution of the finite chemistry rate problem (see Section 2.1.2). Also for all test cases presented a smoothing parameter $\sigma = 40$ is used (see Section 4.4.3).

The resolution of the linear solver using a direct solver such as *PARDISO* proved to be problematic as the large number of DoFs arising from the discretization of all 8 balance equations leaded to large memory requirements. In order to avoid this, in all calculations of this section the multigrid orthonormalization method commented in Section 4.3.4 is used.

The combustion model used is the one-step model shown in Section 2.1. All calculations assume methane as fuel, therefore, the relevant chemical components are CH_4 , O_2 , CO_2 , H_2O and N_2 , thus $N = 5$ and $\mathbf{Y}' = (Y_{\text{CH}_4}, Y_{\text{O}_2}, Y_{\text{CO}_2}, Y_{\text{H}_2\text{O}})$. The nitrogen mass fraction Y_{N_2} is calculated according to Equation (2.23).

This subsection is divided as follows. First in Section 5.3.1 a coflow laminar diffusion flame configuration is calculated and some remarks about the convergence behavior of the XSEC solver are made. Next in Section 5.3.2 a diffusion flame in a two-dimensional counterflow configuration is simulated and compared with results from a one-dimensional configuration. Finally in Section 5.3.3 the convergence rates of the fully coupled solver are investigated by studying a pseudo-one-dimensional diffusion flame configuration.

5.3.1 Coflow laminar diffusion flame

The coflowing flame configuration is used as a first test to assess the behavior of the solver for reactive flows applications, particularly the initialization strategy using the flame-sheet. The configuration classically consists of two concentric ducts that emit fuel and oxidant into the system, which after ignition forms a flame. This configuration has been widely studied, starting with the seminal work of Burke and Schumann (1928) and followed by many others (see, for example, Smooke and Giovangigli (1992), Smooke et al. (1986a), and Braack et al. (1997)). Since the solution of the axisymmetric system of equations presents numerical difficulties that are not the main concern of the present work, in this section an infinitely long slot burner configuration is considered. For that kind of configuration, cartesian coordinates describe the problem naturally.

Set-up

A schematic diagram of the configuration can be seen in Figure 5.29a. The system consists of a fuel inlet with two oxygen inlets on its sides. These inlets are separated by a finite wall thickness. The inclusion of this separation is observed to be necessary to be able to obtain a converged solution, which makes sense, since a finite separation between both inlets smooths the big gradients due to strong mixing and reaction in that area. Although the system is clearly symmetric around the axis $x = 0$, no symmetry assumption is made and the whole domain is considered for the simulation.

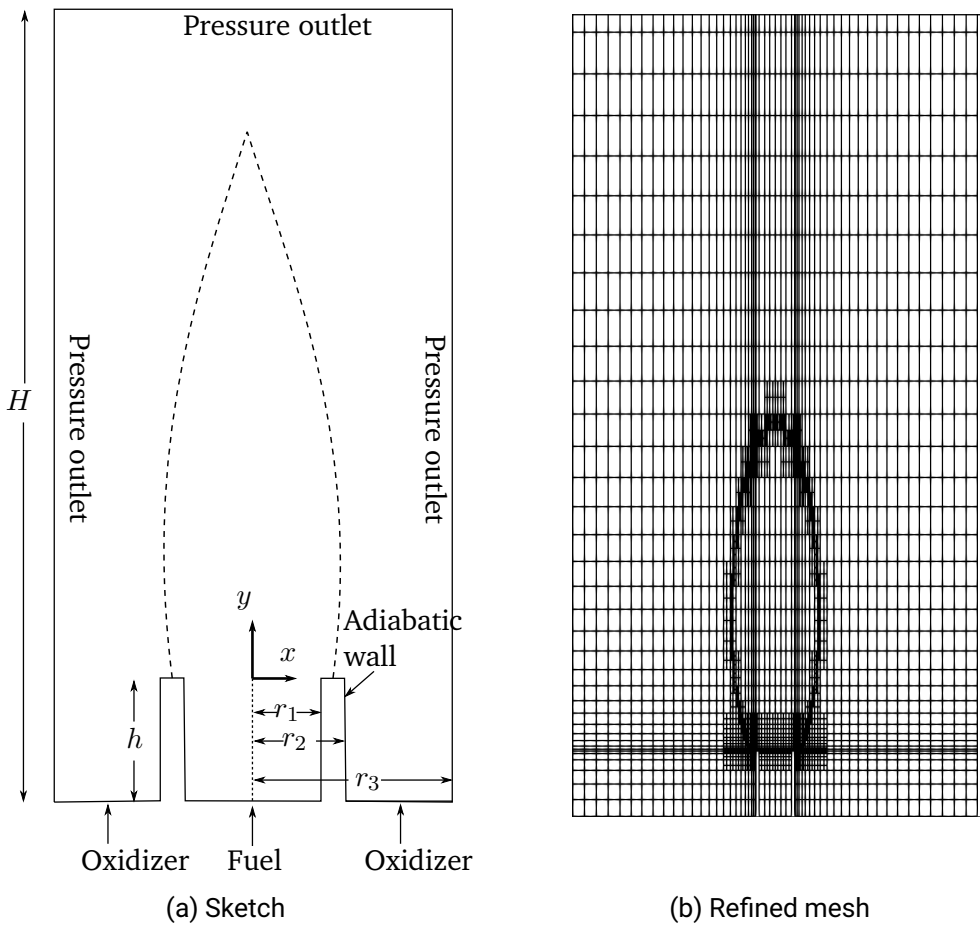


Figure 5.29: Geometry of a coflowing flame configuration (not to scale).

The lengths depicted in Figure 5.29a are set as $r_1 = 1$, $r_2 = 1.2$, and $r_3 = 11.763$. Additionally $h = 4$ and $H = 63$. The lengths r_3 and H are set as arbitrarily large values in order to avoid influence of the outer boundary conditions on the solution of the flame zone. Setting a higher value of r_3 or L did not significantly affect the results. The inlet boundary conditions are set as:

- Oxidizer inlet: $\{\forall(x, y) : y = -h \wedge x \in [-r_3, -r_2] \cup [r_2, r_3]\}$

$$u = 0, \quad v = v_O, \quad T = T^O, \quad \mathbf{Y}' = (0, Y_{O_2}^O, 0, 0)$$

- Fuel Inlet: $\{\forall(x, y) : y = -h \wedge x \in [-r_1, r_1]\}$

$$u = 0, \quad v = v^F(x), \quad T = T^F, \quad \mathbf{Y}' = (Y_{CH_4}^F, 0, 0, 0)$$

The oxidizer enters the system as a plug flow with a constant velocity of $v_O = 1$. The inlet velocity of the fuel stream v_F is a parabolic profile given by

$$v^F(x) = \left[1 - \left(\frac{x}{X_1} \right)^2 \right] v_m^F \quad (5.25)$$

with $v_m^F = 0.592$. The inlet temperatures of both streams is $T^F = T^O = 1$. Combustion of diluted methane on air is considered, with $Y_{CH_4}^F = 0.2$ and $Y_{N_2}^F = 0.8$ for the fuel stream, and

$Y_{O_2}^O = 0.23$ and $Y_{N_2}^O = 0.77$ for the oxidizer stream. The superscripts F and O represent the fuel and oxidizer inlet respectively. The pressure outlet boundary condition is the same as Equation (2.38c). Finally, the boundary conditions at the tips correspond to adiabatic walls, which are defined as in Equation (2.38b), with $\mathbf{u}_D = (0, 0)$.

The variables defined above were nondimensionalized in the usual way. The reference length is $\hat{L}_{\text{ref}} = 0.635$ cm and the reference velocity $\hat{u}_{\text{ref}} = 8.19 \text{ cm s}^{-1}$. The reference temperature is $\hat{T}_{\text{ref}} = 300 \text{ K}$. All derived variables are nondimensionalized using the air stream as a reference condition, i.e. $\hat{\rho}_{\text{ref}} = 1.17 \text{ kg m}^{-3}$, $\hat{\mu}_{\text{ref}} = 1.85 \times 10^{-5} \text{ kg m}^{-1} \text{ s}^{-1}$ and $\hat{W}_{\text{ref}} = 28.82 \text{ kg kmol}^{-1}$, resulting in the nondimensional numbers $\text{Re} = 33.02$ and $\text{Da} = 2.17 \cdot 10^9$. The Prandtl number is assumed to be constant with $\text{Pr} = 0.71$. The reference heat capacity is $\hat{c}_{p,\text{ref}} = 1.3 \text{ kJ kg}^{-1} \text{ K}^{-1}$, which is also the constant value used for the flame sheet calculation (i.e. $c_p = 1$). The choice of this value for the heat capacity is important because it gives a solution of the flame sheet which is similar to the actual solution of the full problem. Gravity effects are not taken into account. The transport parameters are calculated using Sutherland's law with $\hat{S} = 110.5 \text{ K}$. The mixture heat capacity c_p is calculated with Equation (2.28) and using NASA polynomials for the heat capacity of each component. Finally, a nonunity but constant Lewis number formulation is used, with $\text{Le}_{\text{CH}_4} = 0.97$, $\text{Le}_{\text{O}_2} = 1.11$, $\text{Le}_{\text{H}_2\text{O}} = 0.83$ and $\text{Le}_{\text{CO}_2} = 1.39$ (Smooke and Giovangigli, 1991)

Numerical results

The purpose of simulating this case is to test the XNSEC solver in a real-world application with realistic physical parameter values. In particular, it is intended to demonstrate that the strategy of using the flame sheet solution as the initial estimate is adequate for obtaining a converged solution. Numerical experiments using the XNSEC solver showed that the solution of this problem is highly mesh-dependent. The presence of very high gradients in some areas requires a higher density of cells to obtain a well-resolved solution. In Figure 5.29b the actual mesh used for the solution of the full problem is shown. A base mesh with smaller elements in

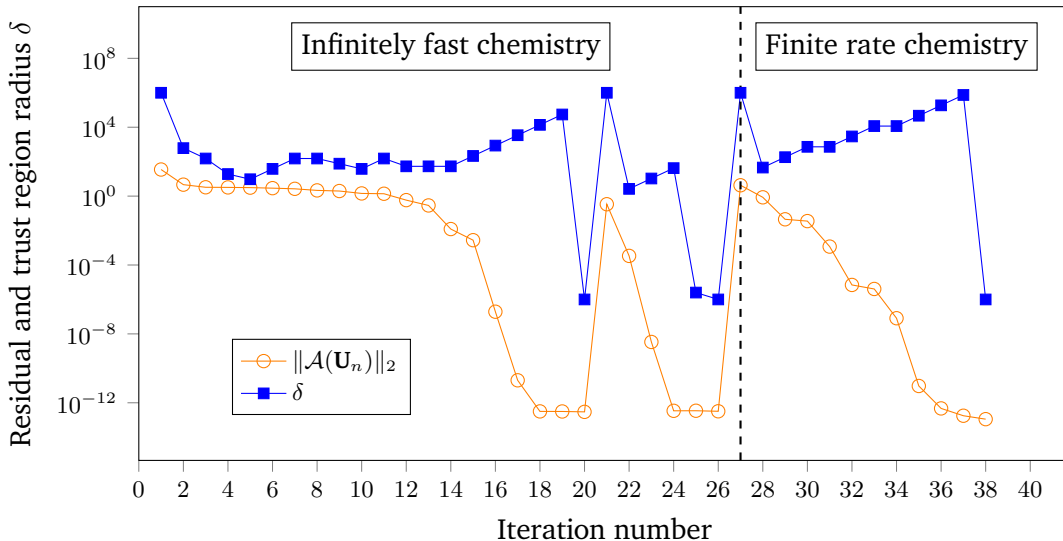


Figure 5.30: Typical convergence history of a diffusion flame in the coflowing flame configuration. Two mesh refinement passes are done. The second pass starts at iteration 21.

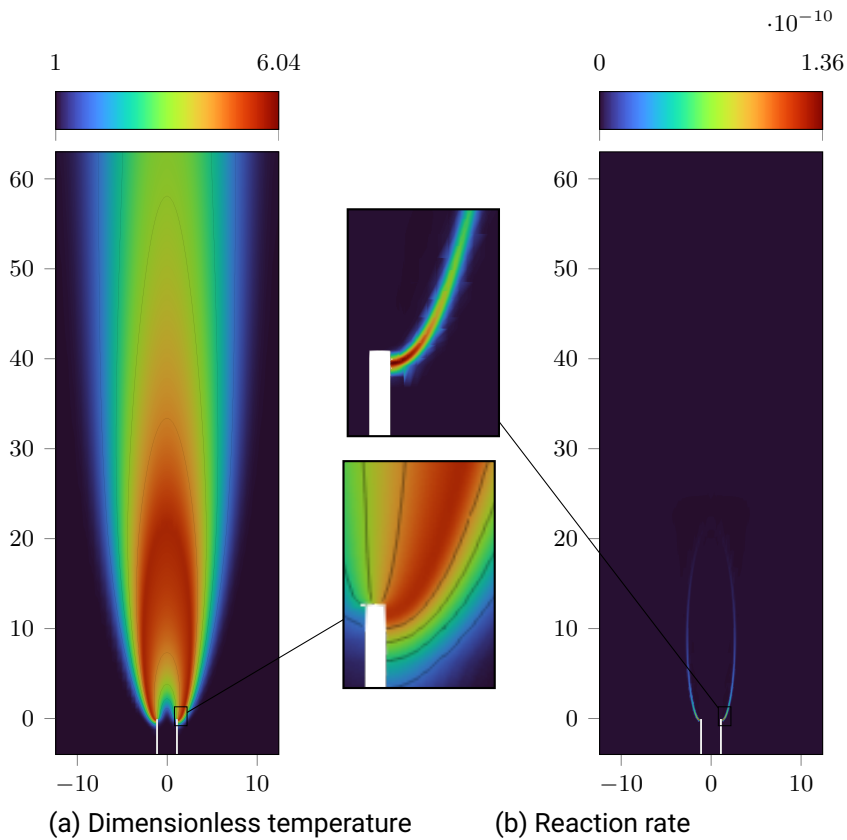


Figure 5.31: Temperature and reaction rate fields of the coflow configuration.

the vicinity of the inlets and larger elements further away from them is used. It is observed that the complex mixing and combustion phenomena that occur in the vicinity of the inlets have a critical effect on the convergence of the solution. For this reason, a special refinement of the base mesh is done in the vicinity of the tips. Another reason that could explain the need for extra refinement in the vicinity of the inlets is that the use of high-order methods introduces very little numerical diffusion into the formulation, which in theory would help to smooth out the large gradients that exist in the area.

It is clear that an adequate mesh resolution at the flame location is critical. In order to avoid over-solving on parts of the computational domain where it is not needed, multiple AMR passes are done. In each pass, after obtaining a steady-state solution the mesh is refined and the calculation is started again (see Section 4.4.4). In particular, for this case, three AMR passes were performed for the flame sheet calculation. After each pass, the mesh is refined in the vicinity of the flame sheet, that is, in the cells where $z = z_{st}$. Obviously, a finer grid in the vicinity of the surface $z = z_{st}$ will be beneficial for the solution of the finite reaction rate problem if the same conditions used to derive the flame sheet equations (namely constant c_p and unity Lewis number) are assumed. However, experiments with the XSEC solver have shown that this refinement strategy is still beneficial for the convergence of the full problem even when using non-constant c_p and nonunity Lewis numbers.

In Figure 5.30 the convergence history using the Newton algorithm presented in Section 4.3.3 is shown. The flame sheet calculation requires 20 Newton iterations to find a solution. It is clearly seen that the residuals $\|\mathcal{A}(\mathbf{U}_n)\|_2$ decrease very slowly for about the first 14 iterations,

while the trust region diameter δ of the globalised Newton method is adapted to find an optimal value to reduce the residuals. Around iteration 14 the algorithm starts to increase δ , leading to a faster reduction of the residuals. A solution to the problem according to the termination criterion exposed in Section 4.3.5 is found in iteration number 20. In iteration 21 mesh refinement based on the strategy mentioned above is used and now only 6 iterations are required to find a converged solution. Finally, in iteration number 27 the flame sheet solution is used as the initial estimate for the full problem, which requires only 11 iterations to find a solution.

For the flame sheet calculation a polynomial degree $k = 2$ is chosen, resulting in a rather small system with 49,140 degrees of freedom. For the finite rate calculation $k = 4$ is used, which resulted in a system with 482,310 degrees of freedom. This highlights another advantage of the approach of using the flame sheet calculation for two-dimensional simulations: the initial estimate can be found relatively easily for a system with few degrees of freedom. Using the solution found as the initial estimate for the full problem facilitates Newton's algorithm, as the complete problem only needs a few iterations to find a solution.

In Figure 5.31 the obtained temperature and reaction rate fields are shown. Since for the selected inlet velocities the flame corresponds to an over-ventilated one, the typical jet form is observed. The maximum dimensionless temperature T reached corresponds to 6.04 (meaning 1812 K). Magnified plots show that the bottom part of the flame sits on the outside part of the tips. The high reaction rates appearing in the area close to the inlets are also worth highlighting. This could explain why the mesh refinement in the vicinity of the inlets is crucial to obtain a converged solution.

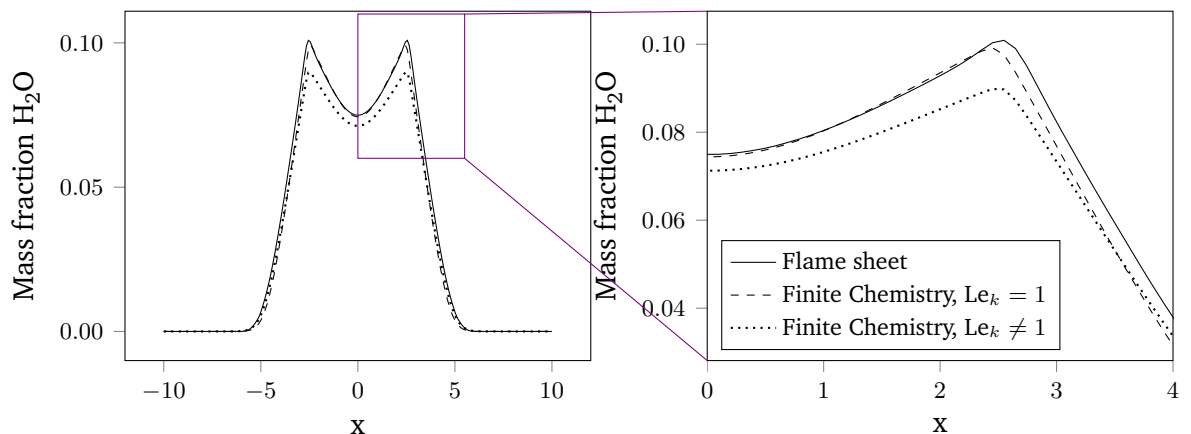


Figure 5.32: Mass fraction field of H_2O over the line $y = 10$

A question to consider is whether indeed the initialization of the finite reaction rate problem with the flame sheet provides adequate estimates for the Newton algorithm, in particular for more complex problems that do not fulfil the assumptions made to obtain the equations of the mixture fraction problem such as nonconstant heat capacity c_p or non-unity Lewis numbers. For illustrative purposes, the simulation of the coflowing flame for unity and nonunity lewis numbers was performed. In Figure 5.32 the solution obtained for the mass fraction field of H_2O along the line $y = 10$ is shown. As expected, the solution obtained for the case with unity Lewis number is very close to the one obtained using the flame sheet. Furthermore, the case with nonunity Lewis number also presents a solution very similar to that of the flame

sheet, with a small deviation in the vicinity of the zones where the chemical reaction occurs. Both finite chemistry calculations use the same initial estimate and both calculations find the converged solution after 11 Newton iterations. In all the simulations shown in this thesis, the use of the flame sheet estimation served as a way to initialize the finite-reaction rate problem.

The simulation of the coflowing flame shows that the strategy of using the flame sheet as an initial condition offers an efficient way to obtain steady-state solutions of combustion problems. Since the flame sheet is only used an estimate for the ignited solution, it is possible to perform the calculations on relatively coarse grids, and use low-order polynomial degrees. The obtained solution can be used as an estimate for calculations with higher polynomial degrees to find a more accurate solution of the full flame problem in a few iterations. A disadvantage, as already mentioned in Section 4.4.3, is the requirement to choose the c_p parameter, since an inappropriate choice gives a solution of the flame sheet problem far away from the solution of the full problem. However, the user's experience and access to experimental information allows estimating this value relatively easily, as also suggested by Smooke et al., 1986b. Note that the value chosen in this section ($\hat{c}_{p,\text{ref}} = 1.3 \text{ kJ kg}^{-1} \text{ K}^{-1}$) served as an adequate estimate for all the simulations presented in this thesis. Note that the results in this section assumed a zero gravity field. Next section will deal with the case where the gravity field influences the flame.

Gravity influence on the flame

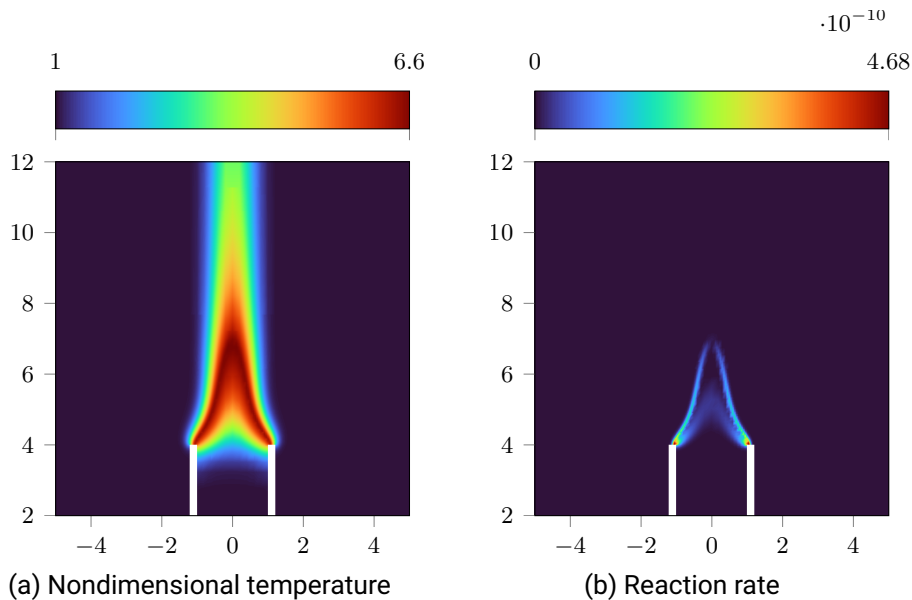


Figure 5.33: Nondimensional temperature and reaction rate fields of the coflow configuration considering gravity effects. Results are zoomed-in, in order to depict more clearly the solution fields.

In this part the case where $\mathbf{g} = (0, -1)$ and $\hat{\mathbf{g}}_{\text{ref}} = 9.8 \text{ m s}^{-2}$ is considered. The setup is exactly the same as the one presented before. Contrary to the case with zero gravity, the simulation of a gravity influenced configuration presented a considerable difficulty to solve. The external force influencing the flow field destabilizes the algorithm, and finding a solution is much more difficult. The flow is said to be convection controlled if the Froude number is large. On the other hand, for small Froude numbers the flow is said to be buoyancy controlled

. Under the conditions mentioned above, the Froude number is $\text{Fr} = 0.1643$, thus the buoyancy effects influence largely the flow field.

In order to obtain a converged solution under these characteristics, the homotopy strategy presented in previous chapters is necessary. The homotopy variable is the Froude number. The infinite reaction rate equations are solved for a series of decreasing Froude values until reaching the desired value $\text{Fr} = 0.1643$. The solution is found after 13 homotopy steps. Finally, when the solution for $\text{Fr} = 0.1643$ is obtained, it is utilized as a initial condition for the full problem, obtaining a converged flame solution. The results of the nondimensional temperature and reaction rate are shown in Figure 5.33. Note the different spatial scale of the figures shown. The flame obtained is much shorter than the case with zero gravity.

5.3.2 Counterflow diffusion flame [†]

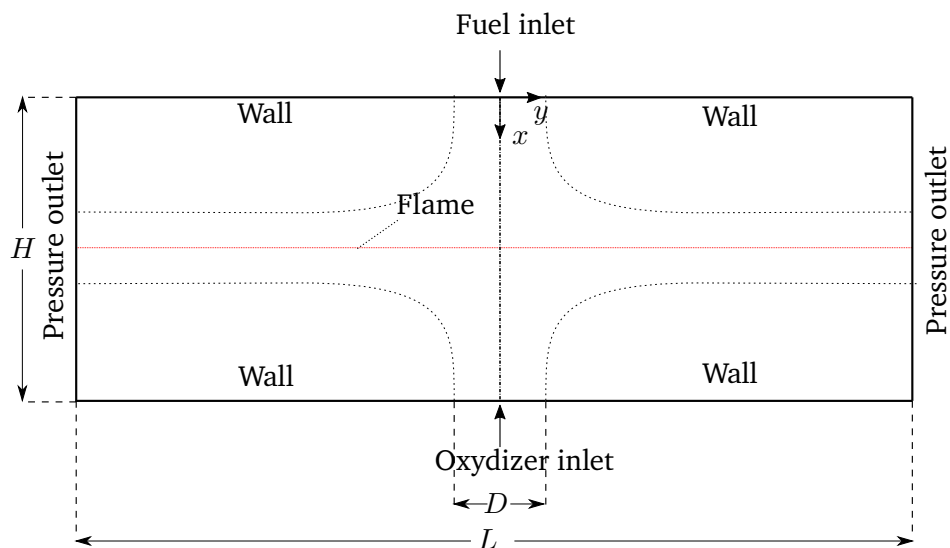


Figure 5.34: Schematic representation (not to scale) of the counterflow diffusion flame configuration.

The counterflow diffusion flame is a canonical configuration used to study the structure of nonpremixed flames. This simple configuration has been a subject of study for decades because it provides a simple way of creating a strained diffusion flame, which proves to be useful when studying the flame structure, extinction limits or production of pollutants of flames (Pandya and Weinberg, 1964; Spalding, 1961; Keyes and Smooke, 1987; Lee et al., 2000). In the work of Paxion et al. (2001) an unstructured multigrid solver for laminar flames with detailed chemistry is presented. A Krylov-Newton method was used for solving several flame configurations. A two-dimensional counter diffusion flame was calculated, and its results were compared with the one-dimensional self-similar solution of the equations. A similar study is presented in this section using the XNSEC-solver.

The counterflow diffusion flame consists of two oppositely situated jets. The fuel (possibly mixed with some inert component, such as nitrogen) is fed into the system by one of the jets, while the other jet feeds oxidizer to the system, thereby establishing a stagnation point flow. On contact and after ignition, the reactants produce a flame that is located in the vicinity of

[†]Modified version from Gutiérrez-Jorquera and Kummer (2022a)

the stagnation plane. A diagram of the setup can be seen in Figure 5.34. In this section, the solution of a steady two-dimensional flame formed in an infinitely long slot burner will be treated. Similarly to the coflow configuration treated before, the infinitely long slot burner configuration can be calculated naturally using cartesian coordinates.

First, as a means of verifying the solver for combustion applications, the results obtained with the XNSEC solver for steady two-dimensional counterflow diffusion flame are compared with the solution of a simplified system of equations for a steady and quasi one-dimensional flame. Later, the influence of the inlet velocities on the maximum temperature is studied and finally some remarks concerning the convergence behavior are given.

The one-dimensional diffusion flame

By assuming an infinite injector diameter, a self-similar solution and by neglecting the radial gradients of the scalar variables along the axis of symmetry, it is possible to reduce the three-dimensional governing equations to a one-dimensional formulation along the stagnation streamline $y = 0$ (see the textbook from Kee et al. (2003) for the derivation). The governing equations for a steady planar stagnation flow reduce to

$$\frac{\partial \hat{\rho} \hat{v}}{\partial \hat{x}} + \hat{\rho} \hat{U} = 0, \quad (5.26a)$$

$$\hat{\rho} \hat{v} \frac{\partial \hat{U}}{\partial \hat{x}} + \hat{\rho} \hat{U}^2 = -\hat{\Lambda} + \frac{\partial}{\partial \hat{x}} \left(\hat{\mu} \frac{\partial \hat{U}}{\partial \hat{x}} \right), \quad (5.26b)$$

$$\hat{\rho} \hat{c}_p \hat{v} \frac{\partial \hat{T}}{\partial \hat{x}} = \frac{\partial}{\partial \hat{x}} \left(\hat{\lambda} \frac{\partial \hat{T}}{\partial \hat{x}} \right) + \hat{Q} \hat{Q}, \quad (5.26c)$$

$$\hat{\rho} \hat{v} \frac{\partial Y_k}{\partial \hat{x}} = \frac{\partial}{\partial \hat{x}} \left(\hat{\rho} \hat{D} \frac{\partial Y_k}{\partial \hat{x}} \right) + \hat{W}_k \nu_k \hat{Q}, \quad (k = 1, \dots, N-1) \quad (5.26d)$$

where \hat{U} is the scaled velocity and $\hat{\Lambda}$ is the radial pressure curvature, which is an eigenvalue independent of \hat{x} . Again, the hat sign represents dimensional variables. The equations are written assuming Fick's law and an one-step combustion model. The system of equations need to be solved for \hat{v} , \hat{U} , \hat{T} and for Y_k with $(k = 1, \dots, N-1)$. In addition, an equation of state and expressions for the heat capacity \hat{c}_p and the transport parameters $\hat{\mu}$, $\hat{\lambda}$, $(\hat{\rho} \hat{D})$ are needed. This formulation is very well known and is often used for analysis of flame structure and determination of extinction points, just to mention a few.

In order to assess the ability of the XNSEC solver to simulate such a system, the solution obtained for a two-dimensional configuration is compared with the solution of the quasi one-dimensional equations solved with BVP4, a fourth order finite difference boundary value problem solver provided by MATLAB (Kierzenka and Shampine, 2001). The BVP4 solver provides automatic meshing and error control based on the residuals of the solution, allowing the development with relatively low effort of a code that solves the one-dimensional equations.

It is important to mention some points regarding the solution of these equations using the BVP4 solver. Analogous to the problem mentioned in Section 4.4.3, the system of Equations (5.26a) to (5.26d) has multiple solutions. One of them is the cold solution and the other is the burning one (see Figure 2.1). The same idea mentioned in Section 4.4.3 is also valid for the quasi-one-dimensional configuration. In particular, this means that a first step for finding a

converged solution of Equations (5.26a) to (5.26d) is to solve the system

$$\frac{\partial \hat{\rho}\hat{v}}{\partial \hat{x}} + \hat{\rho}\hat{U} = 0 \quad (5.27a)$$

$$\hat{\rho}\hat{v}\frac{\partial \hat{U}}{\partial \hat{x}} + \hat{\rho}\hat{U}^2 = -\hat{\Lambda} + \frac{\partial}{\partial \hat{x}} \left(\hat{\mu}\frac{\partial \hat{U}}{\partial \hat{x}} \right) \quad (5.27b)$$

$$\hat{\rho}\hat{v}\frac{\partial Z}{\partial \hat{x}} = \frac{\partial}{\partial \hat{x}} \left(\hat{\rho}\hat{D}\frac{\partial Z}{\partial \hat{x}} \right) \quad (5.27c)$$

together with the equation of state (Equation (2.26)) and expressions for the transport parameters. The dependency of the temperature and mass fractions on the mixture fraction Z is given by the Burke-Schumann limit (see Section 2.2). This solution can be used as an initial estimate for the solution of Equations (5.26a) to (5.26d). It is observed that if the constant value of \hat{c}_p for calculation of the flame sheet is chosen too big, the solver yields the solutions without a flame. For the calculations considered here $\hat{c}_p = 1.3 \text{ kJ kg}^{-1} \text{ K}$ is an adequate value that delivers the ignited solution.

However, it is observed that this flame sheet solution is not directly useful as an initial estimation for the solution using BVP4 of the full system of equations. In order to help the BVP4 solver find a converged solution, an intermediate step is necessary. First, the flame sheet solution is used as an initial estimate for the solution of Equation (5.26) using a constant heat capacity and unity Lewis number. Once the algorithm has found a solution, it can be used for solving the same system but with a variable heat capacity according to Equation (2.28) and user defined Lewis numbers.

It is interesting to mention that other values of the heat capacity \hat{c}_p can lead the algorithm to two other types of solutions. In some conditions it simply obtains the frozen solution, where there are no chemical reactions taking place. A more interesting situation, however, is that the algorithm also finds solutions that correspond neither to the frozen solution, nor to the burning solution, but to a solution where the maximum temperature is in between, which would correspond to the unstable branch shown in Figure 2.1.

Set-up of the two-dimensional counterflow diffusion flame

In this part, the simulation of combustion of diluted methane with air in a two-dimensional infinitely long slot burner configuration using the XNSEC solver is studied. The solution is obtained by solving Equations (2.22a) to (2.22d), making use of the flame sheet solution as initial estimates. The transport parameters are calculated using Sutherland law with $\hat{S} = 110.5 \text{ K}$. Gravity effects are not taken into account. The mixture heat capacity c_p is calculated with Equation (2.28) and using NASA polynomials for the heat capacity of each component.

	$\hat{v}_m^F (\text{cm s}^{-1})$	$\hat{v}_m^O (\text{cm s}^{-1})$	$a(\text{s}^{-1})$	$\hat{T}^F (\text{K})$	$\hat{T}^O (\text{K})$
case(a)	4.85	12.29	36.04	300	300
case(b)	12.13	30.73	84.03	300	300
case(c)	26.69	67.62	176.71	300	300

Table 5.4: Maximum inlet velocity, strain and temperatures used for the counterflow diffusion flame calculations.

For comparison with the quasi-one-dimensional model, three pairs of inlet velocities are considered. They are shown in Table 5.4. Both streams enter at a temperature $\hat{T}^O = \hat{T}^F = 300\text{ K}$. The mass composition of the fuel inlet is assumed to be $Y_{\text{CH}_4}^F = 0.2$ and $Y_{\text{N}_2}^F = 0.8$, and the oxidizer inlet is air with $Y_{\text{O}_2}^O = 0.23$ and $Y_{\text{N}_2}^O = 0.77$.

Counterflow diffusion flames are usually characterized by the strain rate a . Many different definitions for it can be found in the literature (Fiala and Sattelmayer, 2014). In this work the definition of the strain rate based on the maximum axial velocity gradient is used.

The lengths described in Figure 5.34 are $\hat{D} = 2\text{ cm}$, $\hat{H} = 2\text{ cm}$ and $\hat{L} = 12\text{ cm}$. The variables are nondimensionalized using $\hat{L}_{\text{ref}} = 2\text{ cm}$, $\hat{T}_{\text{ref}} = 300\text{ K}$ and $\hat{p}_{\text{ref}} = 101\,325\text{ Pa}$. For each case, the reference velocity is set to $\hat{u}_{\text{ref}} = \hat{v}^O$. Again, all derived variables are nondimensionalized using the air stream as a reference condition, i.e. $\hat{\rho}_{\text{ref}} = 1.17\text{ kg m}^{-3}$, $\hat{\mu}_{\text{ref}} = 1.85 \times 10^{-5}\text{ kg m}^{-1}\text{ s}^{-1}$ and $\hat{W}_{\text{ref}} = 28.82\text{ kg kmol}^{-1}$. The reference heat capacity is $\hat{c}_{p,\text{ref}} = 1.3\text{ kJ kg}^{-1}\text{ K}^{-1}$.

Under this conditions, the Reynolds numbers are $\text{Re} = 156$, $\text{Re} = 390$ and $\text{Re} = 858$, for the low, medium and high inlet velocities respectively. The Prandtl number is assumed to be constant with $\text{Pr} = 0.75$. A nonunity but constant Lewis number formulation is used, with $\text{Le}_{\text{CH}_4} = 0.97$, $\text{Le}_{\text{O}_2} = 1.11$, $\text{Le}_{\text{H}_2\text{O}} = 0.83$ and $\text{Le}_{\text{CO}_2} = 1.39$ (Smooke and Giovangigli, 1991). The system is considered open, the thermodynamic pressure is constant and set to $p_0 = 1$.

The boundary condition of the inlets are

- Oxidizer inlet: $\{\forall(x, y) : y = 0 \wedge x \in [-D/2, D/2]\}$

$$u = 0, \quad v = v^O(y), \quad T = 1.0, \quad \mathbf{Y}' = (0, Y_{\text{O}_2}^O, 0, 0).$$

- Fuel Inlet: $\{\forall(x, y) : y = H \wedge x \in [-D/2, D/2]\}$

$$u = 0, \quad v = v^F(y), \quad T = 1.0, \quad \mathbf{Y}' = (Y_{\text{CH}_4}^F, 0, 0, 0).$$

The pressure outlet boundary condition is the same as Equation (2.38c). The pressure outlet boundaries are placed far away from the center of the domain, to decrease the effect on the centerline. Placing the boundary further away did not appreciably change the results. Finally the boundary conditions at the walls are defined as in Equation (2.38b), with $\mathbf{u}_D = (0, 0)$ and a constant temperature $T = 1.0$.

In Figure 5.35 the solution profiles for case (a) are shown. The used mesh was obtained by a process of mesh refinement. The base mesh is initially created with a larger concentration of elements in the center of the domain. The points of intersection from the velocity inlet and wall boundary conditions are also refined, which was observed to improve the robustness of the algorithm. Similarly to the coflowing flame (Section 5.3.1), during the solution algorithm of the flame sheet problem, the mesh is additionally refined around the flame sheet making use of a pseudo-time-stepping approach. As expected, a stagnation flow develops and a flame forms close to the stagnation streamline. For this strain rate, a maximum dimensionless temperature of $T = 6.05$ is obtained (1815 K). This large increase in the temperature is also reflected in a large decrease of the density. This change of density also causes the acceleration of fluid, as observed in Figure 5.35b.

In Figure 5.35k the reaction rate given by Equation (2.24) is plotted. It is interesting to see that the actual reacting zone is very small, which clearly demonstrates why adequate meshing is necessary to capture the steep gradients resulting from the strong and highly localized heat sources. Finally, and as expected, the fuel and oxidizers fields seem to only be found on either

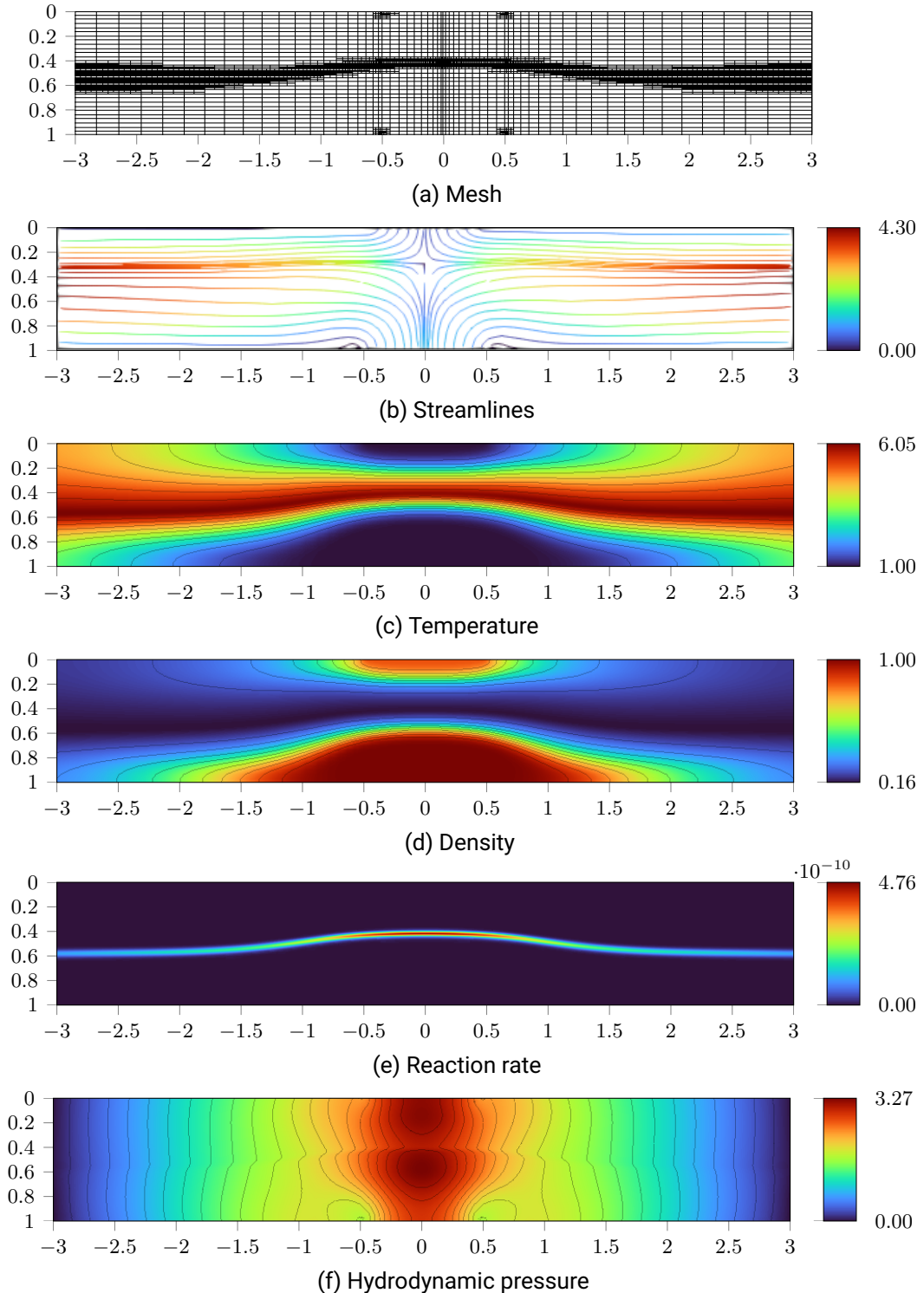


Figure 5.35: Nondimensional solution and derived fields of the counterflow flame configuration for case (a).

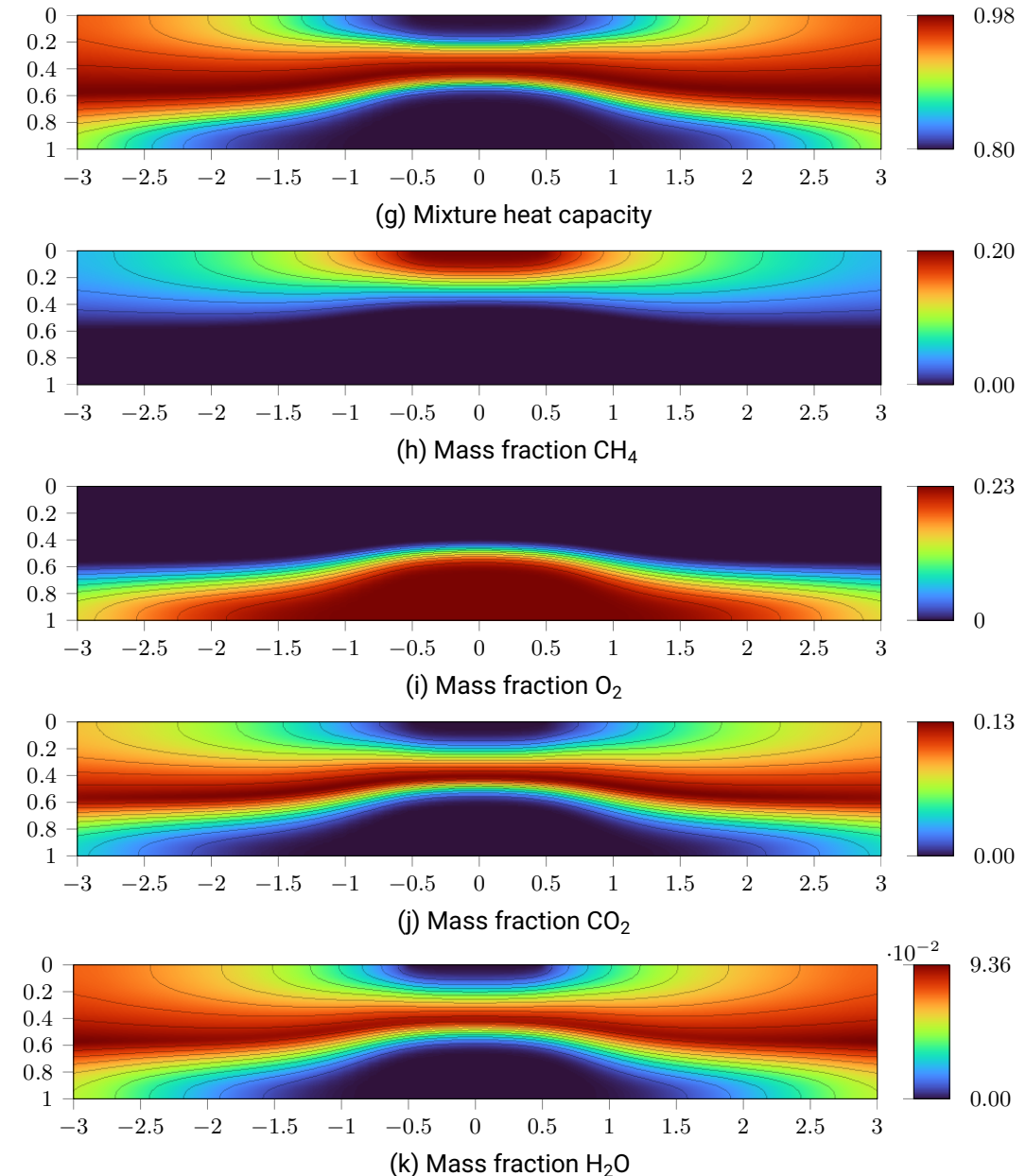


Figure 5.35: Nondimensional solution and derived fields of the counterflow flame configuration for case (a) (continued).

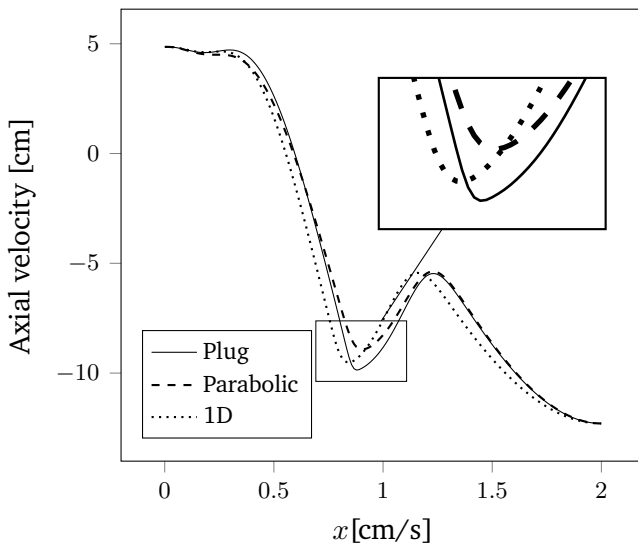


Figure 5.36: Velocity profiles of the counterflow diffusion flame for parabolic and plug inlet boundary conditions.

side of the flame. Although it cannot be seen here, some reactant leaking occurs, meaning that there exists a small zone where both species coexist. This point will be addressed later.

Comparison of two-dimensional and the quasi one-dimensional counterflow flames

In this section a comparison of the results obtained with the XNSEC solver for a two-dimensional counterflow diffusion flame, and the results obtained with the BVP4 solver for a quasi one-dimensional flame is made. This comparison is made along the centerline of the domain (see Figure 5.34). In this section, only dimensional variables will be considered. The transport parameters, chemical model and the equation of state are exactly the same for both formulations. For all calculations in this section done with the XNSEC solver, a polynomial degree of four is used for the velocity components, temperature and mass fractions. A polynomial degree of three is used for the pressure. This results in systems with approximately 439,000 degrees of freedom.

The choice of the type of velocity boundary conditions for the inlets requires some attention. Different possibilities exist to describe the velocity profiles. One possibility is to characterize the velocity boundary conditions by assuming a Hiemenz potential flow, where a single parameter defines the flow field. Other possibilities are also a constant velocity value (plug flow) or a parabolic profile, which allows defining different velocity values for each jet inlet. The effect of boundary conditions on the flame structure has been studied by Chelliah et al. (1991) and Johnson et al. (2015), where it is concluded that both plug and potential flow are able to adequately describe experimental data.

The question of whether a plug or parabolic flow profile allows a better representation of the quasi one-dimensional equations was treated in the work from Frouzakis et al. (1998). There it is stated that the one and two-dimensional formulations yield very similar results, provided that the inlets of the two-dimensional configurations are uniform. Furthermore, preliminary calculations with the XNSEC solver showed that the selection of a plug flow or parabolic have an influence on the solution, as shown in Figure 5.36. Based on these results, the plug flow

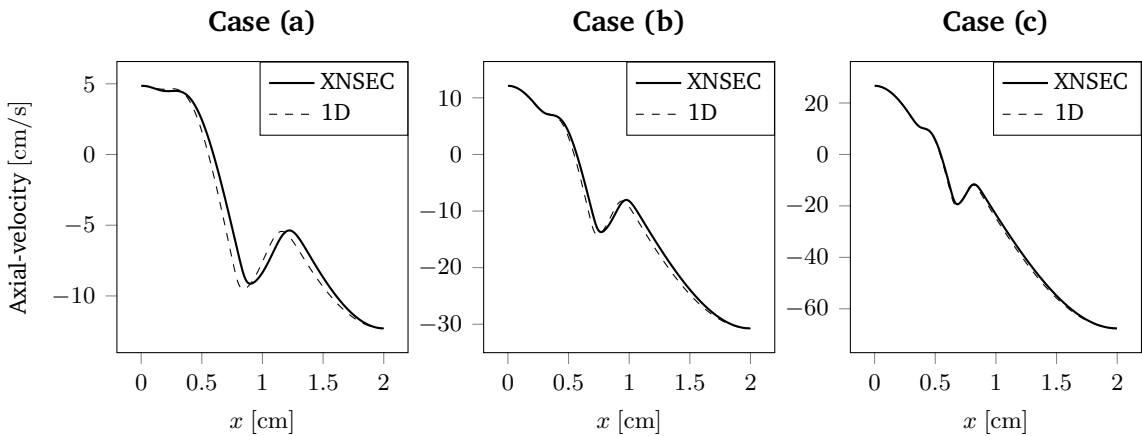


Figure 5.37: Comparison of the axial velocity calculated with the XNSEC solver and the one-dimensional approximation.

boundary condition is adopted for all following test cases.

In Figure 5.37 a comparison of the axial velocities calculated with the XNSEC solver and the one-dimensional solution is shown. While for the high strain case the results agree closely, for lower strains a discrepancy is observed. Recall that the derivation of the one-dimensional approximation assumes a constant velocity field incoming to the flame zone in order to obtain a self-similar solution. In the case of the two-dimensional configuration presented here, the border effects do have an influence on the centerline, which disrupts the self-similarity. This effect is more pronounced for low velocities, which explains the discrepancy between curves.

In Figure 5.38 the temperature and mass fraction fields are presented. Again, a discrepancy is observed for low strains, but results show a good agreement for higher inlet velocities. It can also be observed that, as expected, at higher strains a significant leakage of oxygen across the flame is present. This is a typical behavior of a flame that is getting closer to its extinction point (Fernandez-Tarrazo et al., 2006).

A drawback from the usual one-step models with constant activation temperature is that they tend to over predict fuel leakage. This behavior is not observed in the one-step model with variable activation temperature used here. In Figure 5.39 the comparison is shown for the configuration (c) between the mass fractions fields obtained using a chemical model with variable kinetic parameters given by Equations (2.19) and (2.20) and with constant kinetic parameters using $\hat{T}_a = \hat{T}_{a0}$ and $\hat{Q} = \hat{Q}_0$. The oxygen leakage obtained by using the chemical model with variable parameters is evident, demonstrating that the chemical model is capable of appropriately modeling the leakage phenomenon.

In Figure 5.40 the maximum temperature obtained at the centerline for different strain rates is plotted. Qualitatively speaking, the solution obtained with the XNSEC solver agrees with the expectations. As the strain rate increases the residence time decreases, the system moves away from equilibrium and the maximum temperature decreases (see Figure 2.1). On the other hand, the comparison of values obtained with the XNSEC solver and those of the quasi-one-dimensional approximation clearly shows a discrepancy in the results. For low strain rates, this discrepancy is small, being only 10 K for $a = 20 \text{ s}^{-1}$, approximately a difference of 0.5%. As the strain rate increases so does the discrepancy. For $a = 200 \text{ s}^{-1}$ the difference is almost 50K, which is a 9% disagreement. A similar behavior is also reported in Frouzakis et al. (1998), where a difference of 50K was obtained between the results of a two-dimensional

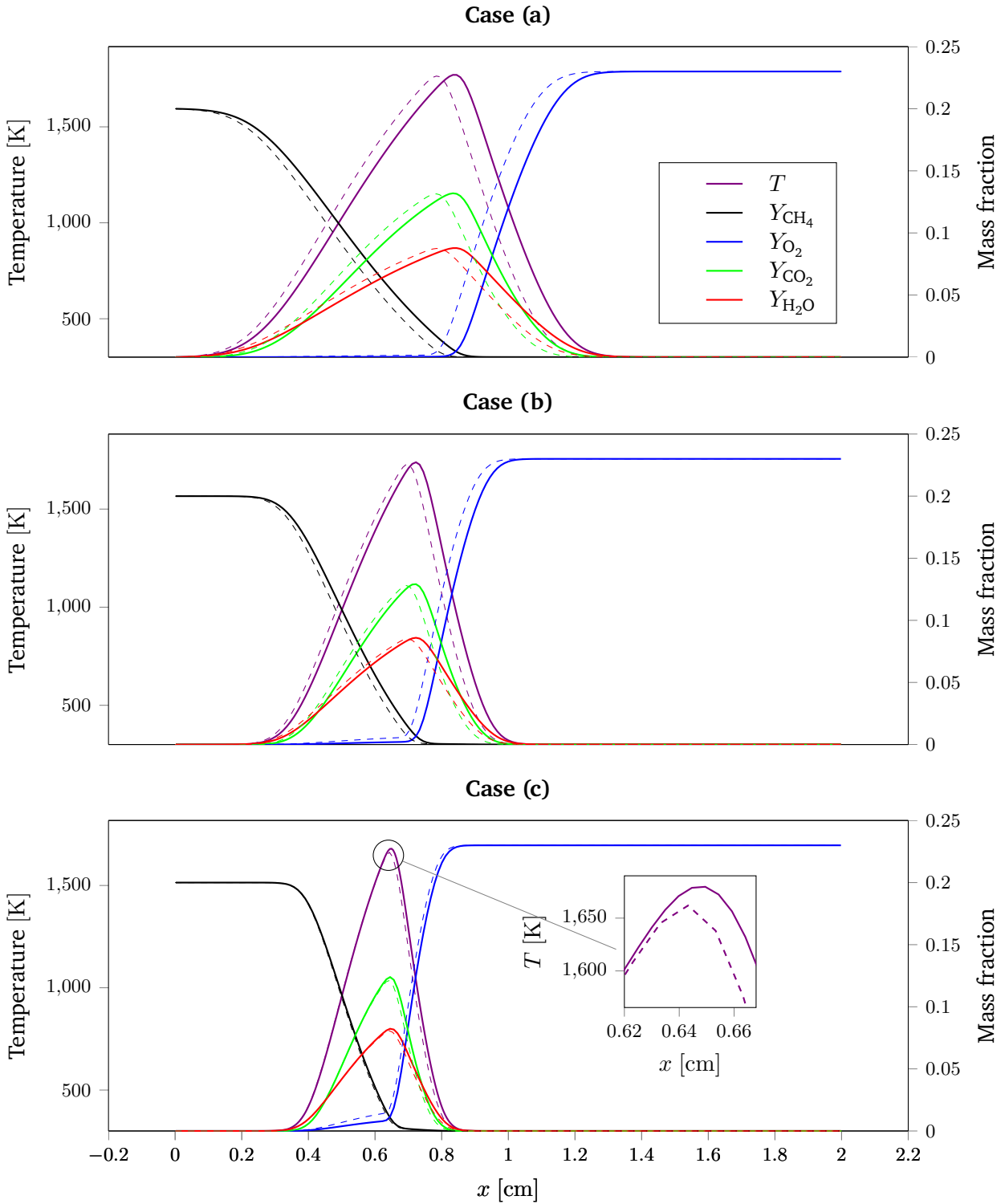


Figure 5.38: Comparison of temperature and mass fraction fields obtained with the XNSEC solver (solid lines) and the one-dimensional approximation (dashed lines).

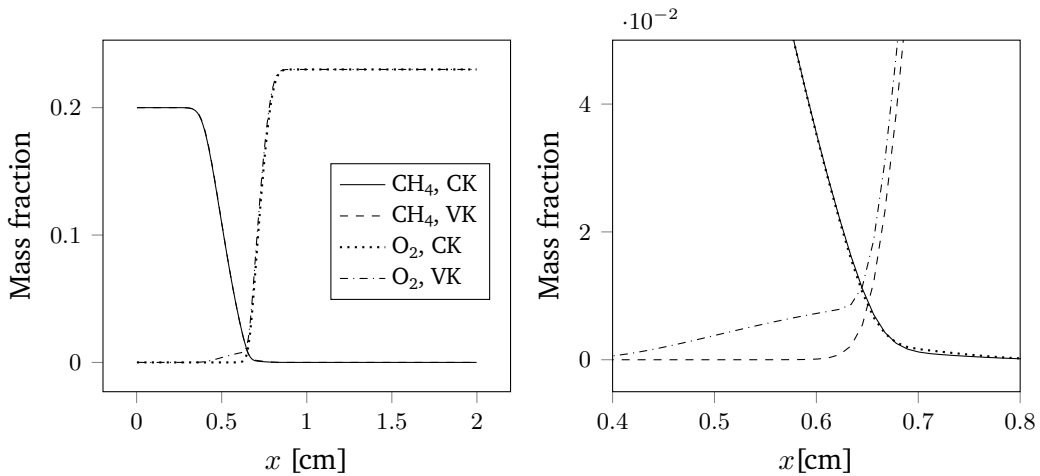


Figure 5.39: Oxygen leakage in the counterflow diffusion flame configuration. Fuel and oxidizer mass fraction profiles using variable kinetic parameters (VK) and constant kinetic parameters (CK) are shown. Right picture is zoomed in near the flame zone.

axisymmetric configuration and a quasi-one dimensional configuration.

It is worth noting that the XSEC solver was not able to find a converged solution for $a > 202 \text{ s}^{-1}$, and the Newton algorithm stagnates. This is most probably a sign of under-resolution of the mesh, and that the used refinement strategy did not help for such high strain rates. A better mesh refinement strategy is necessary for calculating the flame at conditions near the extinction point. Moreover, for high strain rates, the flame will be far from the thermochemical equilibrium, and it is likely that the solution obtained for the flame sheet will be far from the solution with finite reaction rates. A possibility would be to use one of the well-known continuation methods to progressively move in the direction of the extinction point (see, for example, Nishioka et al. (1996)). The homotopy methodology presented in Section 4.4.1 can be viewed as one of those methods and would be useful when looking for solutions of systems that are close to the extinction point, by gradually increasing the velocity of the inlets. A complexity that arises is how to create in a robust way a dynamical mesh that is suitable for obtaining the intermediate solutions while searching for the final result. This issue is beyond the scope of this thesis and may be the subject of future research.

The difference between the results obtained for the two-dimensional configuration and the quasi-one dimensional approximation could be explained by some condition within the 1D system assumptions being violated in the set-up of the 2D configuration. It is known that in addition to the boundary conditions, the ratio between the width of the slot and the separation between the two slots (here $D/H = 1.0$) also has an influence on the solution and that a high ratio is desirable (Frouzakis et al., 1998). Experiments with the XSEC solver showed that increasing the ratio to $D/H = 1.5$ or decreasing it to $D/H = 0.75$ did not change the results appreciably.

Another point that was not addressed here is whether the boundary conditions chosen for the cold walls have an effect on the solution along the centerline. Other possibilities could have been using outlet boundary conditions or an adiabatic wall. However, it is expected that its effect on the centerline would not be big.

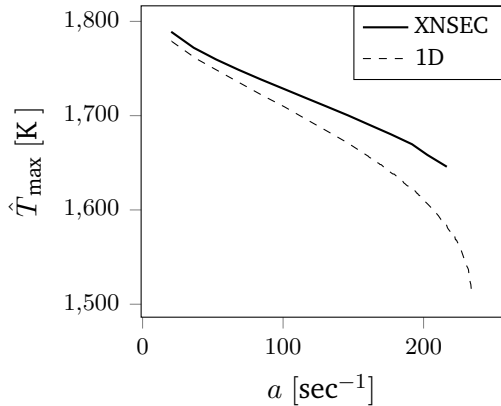


Figure 5.40: Maximum centerline temperature of a counterflow flame for different strains.

Temperature convergence study

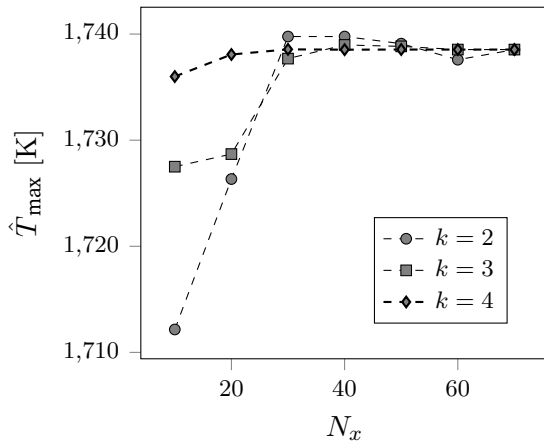


Figure 5.41: Convergence study of the maximum value of the temperature for the counterflow diffusion flame configuration.

Similarly to problems presented in earlier sections, the presence of singularities caused by non-consistent boundary conditions causes a degenerative effect on the global error values, making a global convergence study for this configuration problematic. However, it is still possible to study the behavior of some characteristic point value under different conditions to prove the mesh independence of the solution.

In Figure 5.41 it is shown how the maximum temperature along the centerline obtained for the case (b) behaves under different number of elements in the x direction (N_x) and polynomial degrees. The values for $k = 1$ are not shown, because for this range of cell elements, the maximum temperature value was of the order of 60K higher than the ones depicted here. The temperature tends to a limit value, and it is possible to observe how this value is reached already for coarse meshes when using a polynomial degree of three or four. For $k = 2$ the temperature also tends to a limit value, but at a slower rate compared to $k = 3$ or $k = 4$.

In the next section a simplified one-dimensional flame configuration will be used in order to be able to realize a global h -convergence study of the whole system operator.

5.3.3 Chambered diffusion flame

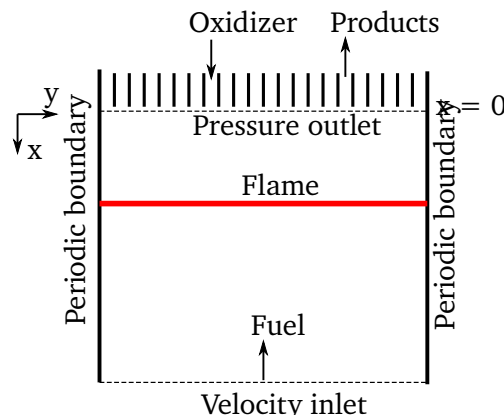


Figure 5.42: Schematic representation of the chambered diffusion flame configuration.

In this chapter an h -convergence study for a quasi-one-dimensional configuration is shown. This is done by using a planar unstrained diffusion flame in the so-called chambered diffusion flame. This configuration has served as a model for many theoretical studies related to diffusion flames (Matalon et al., 1980; Rameau and Schmidt-Lainé, 1985; Matalon and Metzener, 2010).

A sketch of the configuration can be seen in Figure 5.42. Fuel is injected at a constant rate into the bottom of a small insulated chamber, while oxidant diffuses into the system against the direction of the flow. Constant conditions at the outlet of the chamber are achieved in an experimental setting by a rapid renewal of the flow of the oxidant. Under these conditions, an unstrained planar flame is formed.

The fuel inlet into the chamber is modeled with a constant velocity inlet boundary condition Equation (2.38a), while the flow outlet at the top is considered an outlet as given by Equation (2.38d). Since the interest is in the flame far away from the container walls, it is sufficient to set the remaining boundary conditions as periodic boundaries. This effectively transforms the problem into a pseudo-two-dimensional configuration.

The inlet velocity of the fuel jet is set to 2.5 cm s^{-1} and its mass composition is $Y_{\text{CH}_4}^0 = 0.2$ and $Y_{\text{N}_2}^0 = 0.8$ while air has a composition $Y_{\text{O}_2}^0 = 0.23$ and $Y_{\text{N}_2}^0 = 0.77$. The temperature of the fuel and air feed streams is 300 K. The length of the system L is equal to 0.015 m. The Reynolds number is $\text{Re} = 2$.

For this configuration, an h -convergence study is conducted, where uniform Cartesian meshes with 5×2^6 , 5×2^7 , 5×2^8 , 5×2^9 and 5×2^{10} cells are used. The polynomial degrees are varied from one to four for velocity, temperature and mass fractions, and from zero to three for pressure. Errors are calculated using the finest mesh as a reference solution.

The results are shown in Figure 5.43 for variables u , T , Y_{CH_4} and p . The convergence results for other variables are similar and not shown here. The expected convergence rates characteristic for the DG method are observed. For low polynomial degrees the orders of convergence are very close to the theoretical values. However for higher polynomial degrees a slight deterioration of the convergence rate is observed.

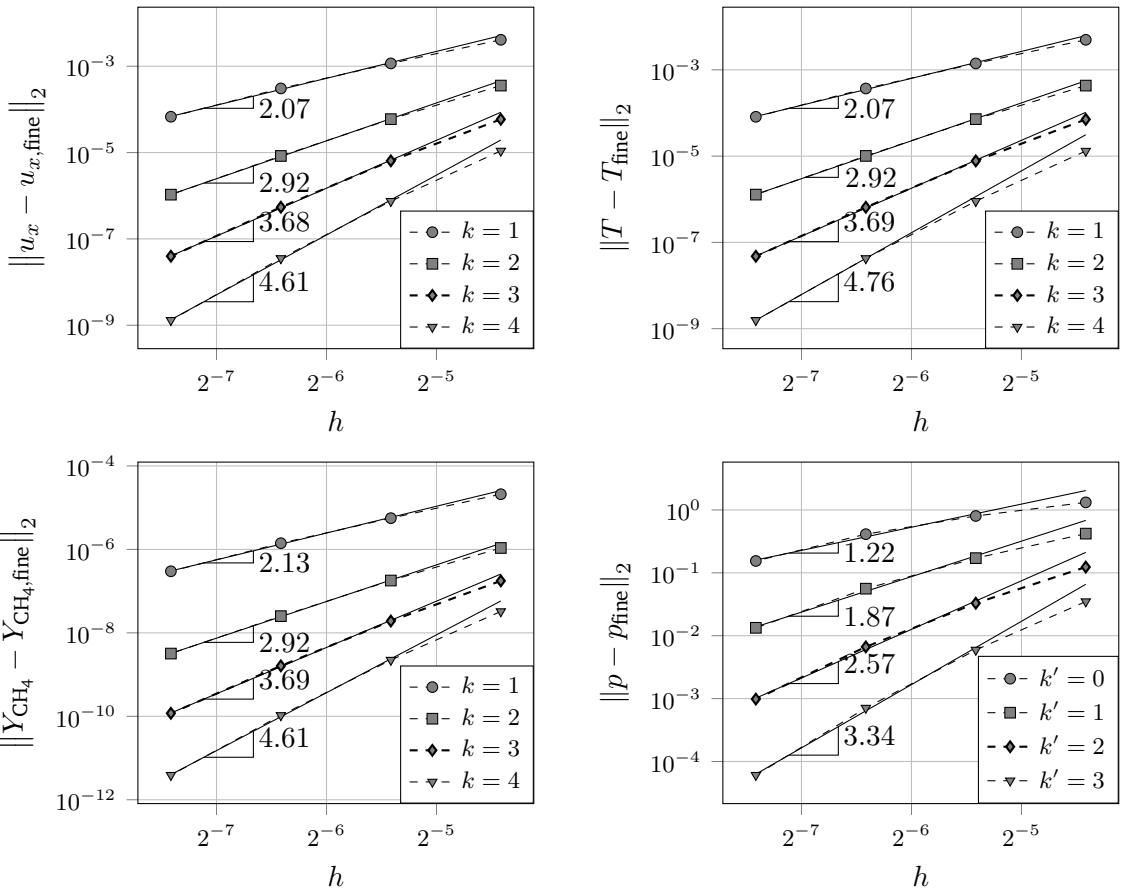


Figure 5.43: Convergence study for the chambered diffusion flame configuration.

5.3.4 Combustion over a square cylinder

As a last testcase of the XNSEC solver, a configuration very similar to the one previously shown for the flow over a cylinder was simulated, but now extending the case to a system where combustion is present. Unlike Section 5.2.4, for this test case the flow over a square cylinder is considered. The simulation is non-stationary and shall serve as a test of the time-stepping together with the AMR algorithms. As will be explained later, this was not possible with the current solver implementation, and only some simplified cases will be shown. First, results for a non-reactive steady state solution are shown. Later, an unsteady case with combustion present is analysed.

Flow over a heated square cylinder

In the work from Miao (2022) the XNSEC solver was used for calculating the flow around a heated square cylinder. The results were compared with the data published by Sharma and Eswaran (2004) for the recirculation lengths after the square cylinder. Simulations were performed with Reynolds numbers ranging from $Re = 5$ to $Re = 40$. The square cylinder is modeled by no-slip walls with $(u, v) = (0, 0)$ and the incoming flow field (air inlet in Figure 5.44) is $(u, v) = (1, 0)$. The fluid considered is air. In Figure 5.45 a comparison of the normalized recirculation length L_r/B obtained with the XNSEC solver and the reference is shown. The

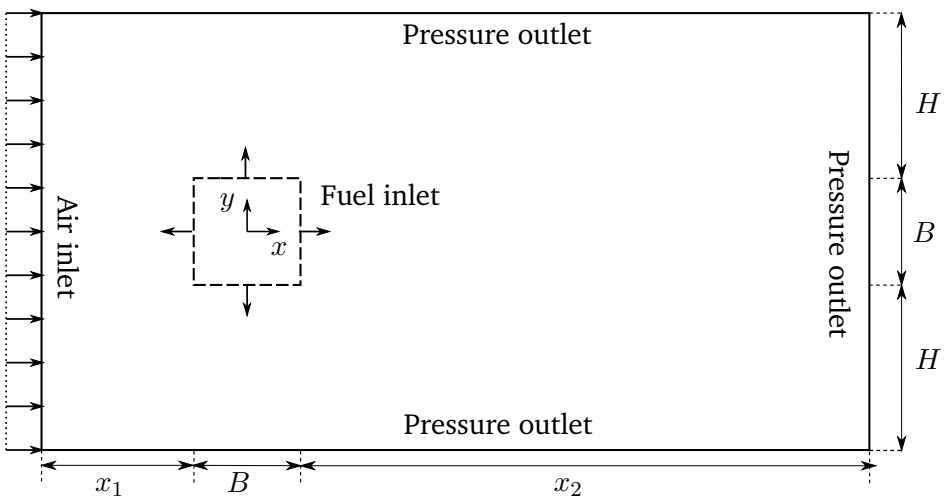


Figure 5.44: Temperature field and mesh of the unsteady combustion over a square cylinder.

results agree very well, deviating slightly at higher Reynolds numbers.

Unsteady combustion over a square cylinder

The last test of the XNSEC solver was done with the objective of calculating a non-stationary flame. It is well known that there is a critical Reynolds value (at least for non-reactive systems) from which the system becomes non-stationary. According to Sharma and Eswaran (2004), for $Re > 50$ the flow has a non-stationary periodic character. In this section results from two simulations are shown. For the first one, a constant density is assumed, and in the second one the equation of state is used. A sketch of the configuration is shown in Figure 5.44. Fuel is expelled at a constant rate and homogeneously through the cylinder. A constant flow of air in the horizontal direction comes in contact with the fuel, which eventually forms a flame.

The lengths depicted in Figure 5.44 are set to $B = 1$, $x_1 = 4$, $x_2 = 22$ and $H = 8$. The

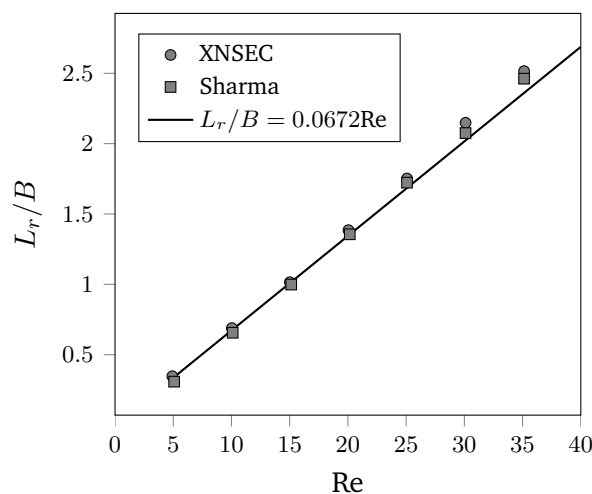


Figure 5.45: Recirculation lengths for different Reynolds numbers for the non-reactive case.

air enters with a uniform velocity to the system $(u, v) = (1, 0)$, and uniform temperature $T = 1$. Its composition is $Y_{O_2}^O = 0.23$ and $Y_{N_2}^O = 0.77$. The fuel inlet enters with a velocity field $(u, v) = (0.2x/B, 0.2y/B)$, has a uniform temperature $T = 1$ and composition $Y_{CH_4}^F = 0.2$ and $Y_{N_2}^F = 0.8$. A Reynolds number of $Re = 300$ is set, for which in the non-reactive case the vortex shedding phenomenon occurs. The Prandtl number is set to $Pr = 0.75$.

For this simulations only the infinite-reaction rate equations given by Equation (2.31) are calculated and advanced in time. The initial conditions used are similar to those of the circular cylinder in section Section 5.2.4. Again, an initial vortex is used to trigger the vortex shedding according to

$$u(t=0) = 1 + u^{\text{vortex}}, \quad (5.28a)$$

$$v(t=0) = 0 + v^{\text{vortex}}, \quad (5.28b)$$

$$Z(t=0) = 0, \quad (5.28c)$$

$$p(t=0) = 0. \quad (5.28d)$$

where the vortices u^{vortex} and v^{vortex} are given by Equation (5.18). The strength of the vortex is $a = 1$ and its center is initially located at $(x^o, y^o) = (-2.5, 0)$. A Cartesian base mesh with 54×32 elements is used, which is refined or coarsened as necessary during the simulation. The calculation time is set to $t = 100$, with constant time steps of $\Delta t = 0.05$. A BDF-2 scheme is used for the temporal discretization.

The time-dependent simulation of a combustion phenomenon proved to be very challenging and the temporal discretization described in Section 3.1.3 did not allow obtaining solutions of this problem. In particular, it is observed that the time derivative of the continuity equation $\partial\rho/\partial t$ is a source of numerical instabilities, particularly in systems with large density variations. This is a fact already reported in the literature. In the work of Nicoud (2000) difficulties are reported for obtaining solutions for density ratios greater than three. In this context density ratios refer to the ratio between maximum and minimum density appearing in the system. In the work of Rauwoens et al. (2009) and Cook and Riley (1996) a similar destabilization effect is also reported for high density ratios, reporting also better stability properties when using even-ordered schemes compared to odd-ordered schemes.

It must be mentioned that the non-isothermal unsteady flow configurations presented until this point didn't present any kind of particular problems for its solution. Those test cases presented however only moderate density ratios, the largest of them being 1.5. On the other hand, for a combustion process like the one presented here, the density ratios are much higher, even higher than six for typical combustion cases.

Nevertheless, simulations of this test case ignoring the $\partial\rho/\partial t$ term were performed. This is clearly a non-physical approximation, but is nonetheless used to showcase the capability of the solver for calculating unsteady reacting flow.

Constant density

First, the problem was calculated with the assumption of a constant density $\rho = 1$. By doing this, the term $\partial\rho/\partial t$ is automatically equal to zero, and the momentum equation is only slightly coupled to the mixture fraction equation, since the viscosity still depends on the temperature. In Figure 5.46 the temperature field is shown at different times. Obviously, since this is a simplified case, using the flame sheet circumvents the need to simulate the ignition of the system, and from the instant $t = 0$ onward the system already has areas where the temperature

reaches the adiabatic temperature. It can be seen that the vortex-shedding phenomenon appears, as expected for a number $Re = 300$. It is interesting to see that the vortex shedding separation point moves downwards (compared with a square cylinder without outflow) since the incoming air flow is pushed by the fuel exiting the cylinder. The mesh obtained from the mesh refinement process is also shown. The mesh is refined or coarsened after each time-step by using as a criterion the location of the flame sheet, meaning that cells where $z = z_{st}$ are refined. The calculations were performed using eight cores. The algorithm performs well for this configuration, needing at most 5 Newton iterations to reach convergence.

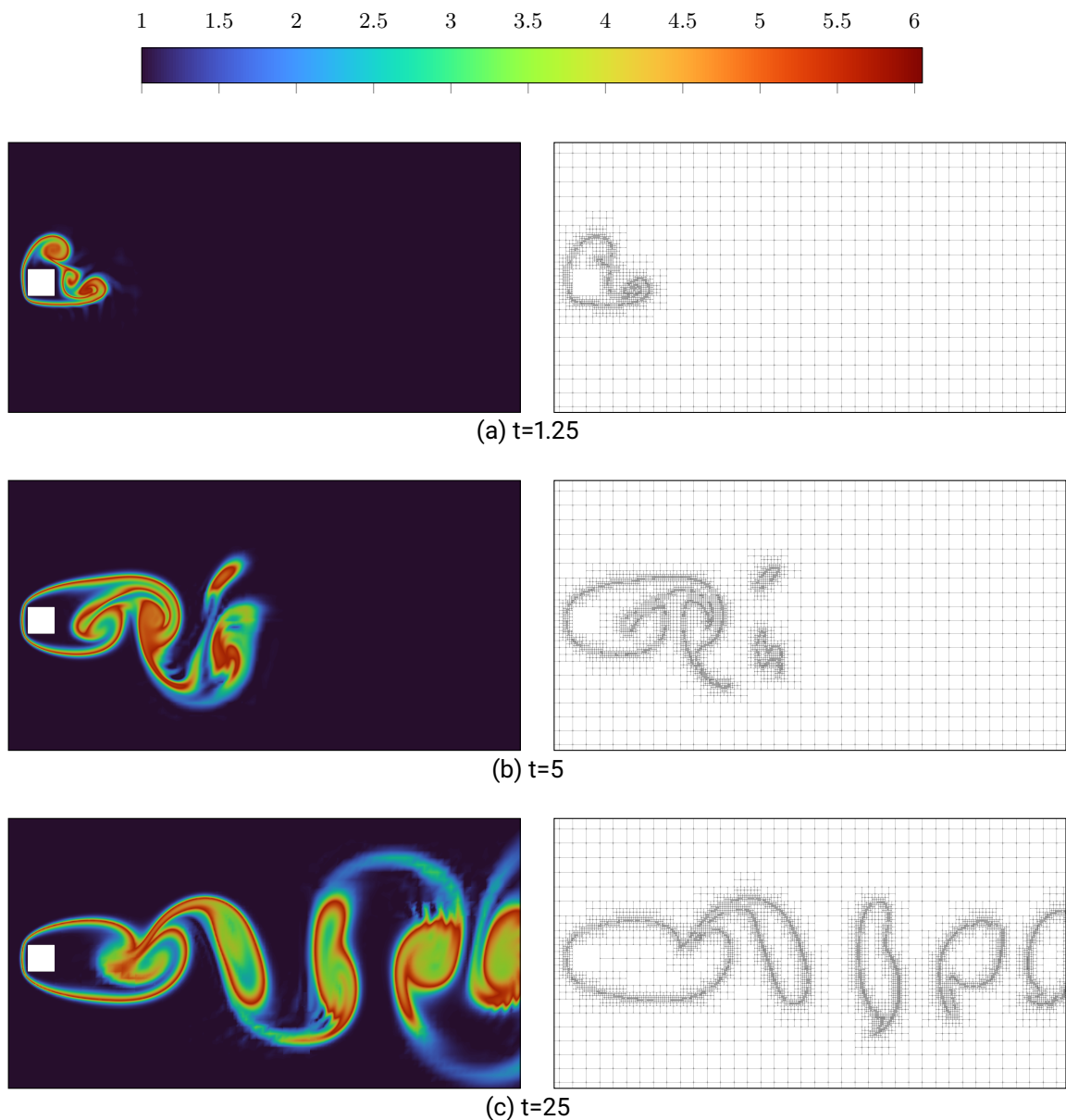


Figure 5.46: Temperature field and mesh calculated with the Burke-Schumann solution at different times, assuming a constant density.

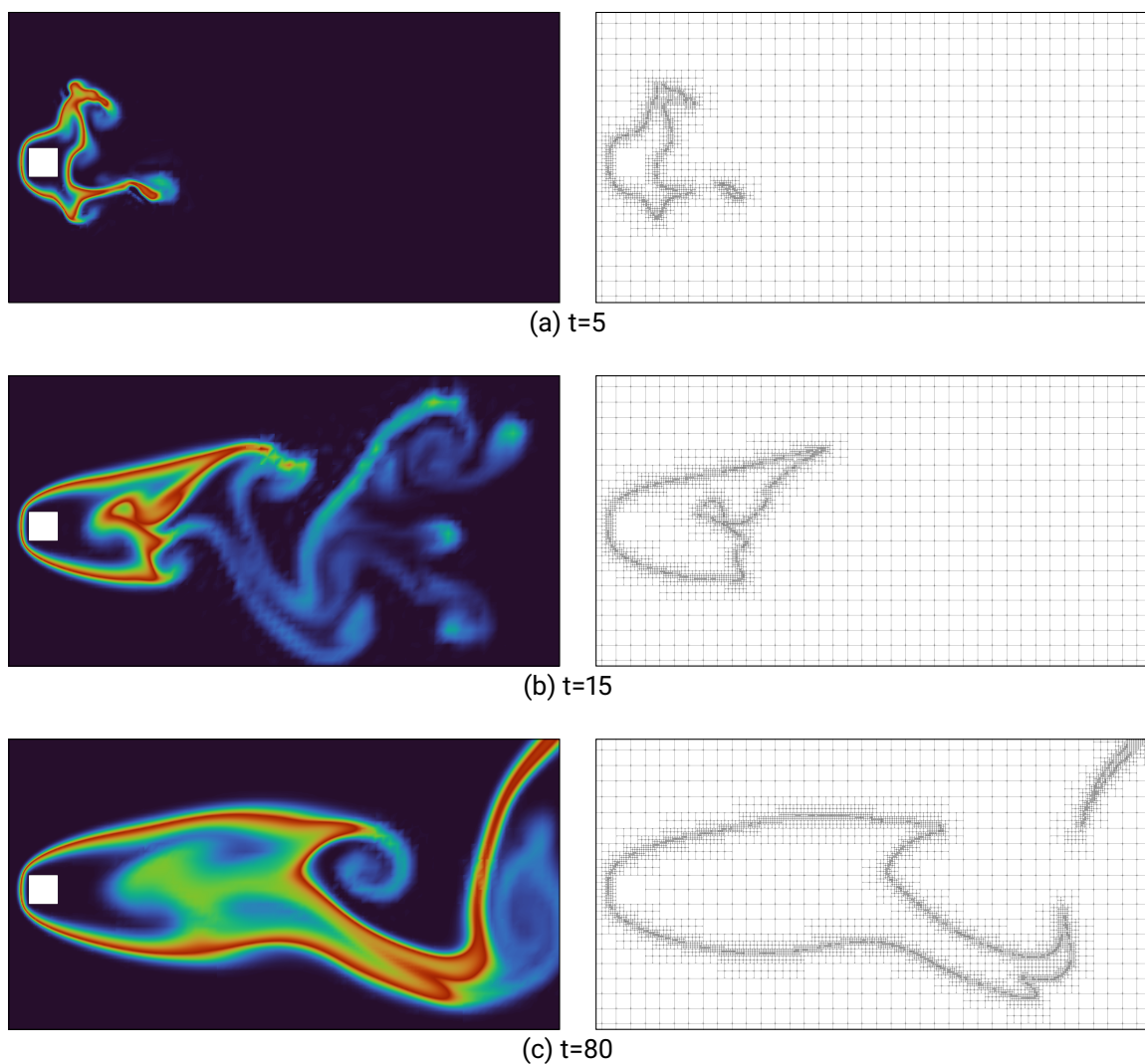
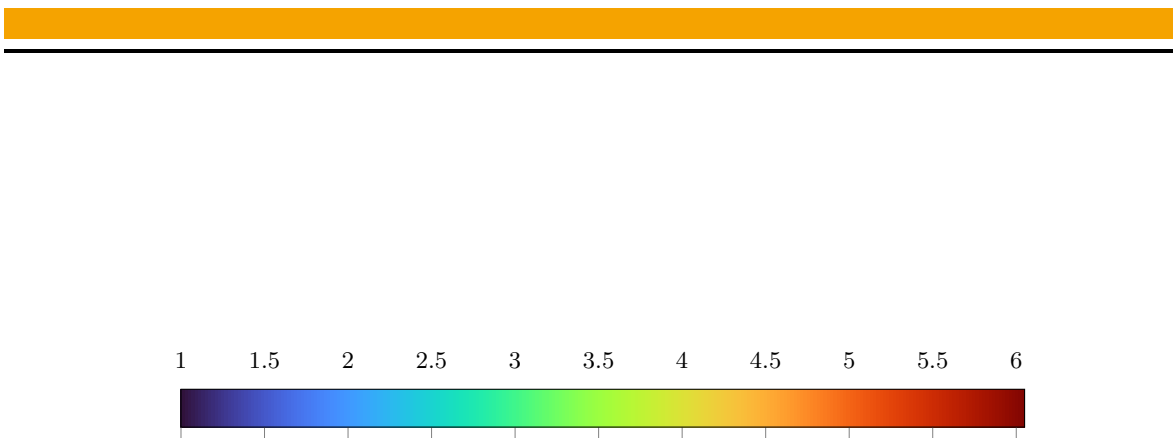


Figure 5.47: Temperature field calculated with the Burke-Schumann solution at different times.

Variable density

Finally, the configuration using a variable density was calculated. The temperature fields and meshes are shown in Figure 5.47. It is interesting to observe the great effect that the big density variations caused by the combustion have on the flow structure. The zones near the flame sheet are greatly accelerated because of the big reduction in the density. The refinement strategy mentioned before was used, and was observed to be critical for finding converged solutions of the system. Interestingly, the zone of the domain where the vortex shedding commences in this configuration, is shifted even further to the right compared with the case mentioned above. This is clearly attributable to the flow acceleration due to the high density variations in the zones where chemical reaction takes place.

The number of DoFs for the simulation range between 62064 for the initial mesh, and 224280 for the mesh corresponding to the last iteration. The relatively low number of DoFs allowed to use the direct solver *PARDISO* during the whole course of the simulation. The calculation time of each timestep ranges between two minutes for the coarse initial mesh and 20 minutes for the finest mesh obtained at the end of the simulation. This relatively high calculation time could be a big drawback of the presented algorithm. The fully coupled solution of the system leads to very big matrices which have to be solved with efficient linear solvers. Although the linear solvers used in this work are very efficient, other specialized solvers could be used in order to reduce the calculation times, particularly for transient simulations. This is a point which should be addressed in future work.

The infinite reaction rate equations were used in this test mainly to reduce the calculation time of the transient system. The finite reaction rate equations could have been solved by using a similar strategy as the one used for steady state calculations, meaning that the system Equation (2.31) can be solved for an initial time interval, after which the finite reaction rate equations are initialized and advanced in time. Due to the long calculation times for this kind of simulations, this aspect was not explored in the present work.

5.4 Conclusion

In this chapter a very detailed verification of the solver by means of several benchmark configurations is done. They also allow to highlight some of the benefits of the algorithms presented in this work.

First, two classical incompressible benchmark cases are selected: the lid-driven cavity flow and the backward-facing step. These cases are simulated and compared with reference solutions, obtaining very good agreement of the results. The recirculation lengths of the backward facing step agree very well with the lengths reported in other publications. Interestingly the XNSEC solver encounters a secondary recirculation zone for $Re = 200$, which is not reported in the benchmark solutions.

Subsequently, several test cases in which temperature plays a significant role are analyzed. A heated backward-facing step is calculated and compared with the benchmark results, again obtaining very good result agreements. Later, a Couette flow configuration with a vertical temperature gradient is used for determining the experimental order of convergence of the solver for single-component nonisothermal systems, where the expected rates of the DG method are observed. The capability of the XNSEC solver for simulating buoyancy driven flows is tested by means of the heated square cavity problem. This test case also serves to prove the ability to solve flows in a closed system. A very thorough comparison with benchmark

results is performed, obtaining very satisfactory results. The Newton-Dogleg method proved to be adequate for systems up to a Rayleigh number of $\text{Ra} = 10^5$. Larger Rayleigh number values required the use of the homotopy algorithm in order to find a converged solution. The convergence properties for the non-isothermal closed-system flow are also calculated, and the expected DG convergence rates are obtained; only for $k = 4$ a slight deterioration of the rates is observed.

Later, an unsteady nonisothermal test case is shown, namely the flow over a heated circular cylinder. The unsteady behavior of the solution obtained agrees very well with the benchmark results, and the expected Kármán vortex street is observed. The behavior of the solver with respect to perturbations is studied by means of the Rayleigh-Bénard convection problem. The critical value obtained for the Rayleigh number at which the system exhibits convective fluid motion is calculated with precision of 0.009% compared to theoretical values.

Finally, the XNSEC solver is used to solve several classical diffusion flame configurations. First, a coflowing flame is simulated, which served to highlight the benefits of the strategy of using flame-sheet estimates, and also for showing the behavior of the nonlinear solver. Later, a verification of the spatial discretization for the reactive case is performed by means of the counterflow diffusion flame configuration. The results obtained using the XNSEC solver for this configuration at varying strain rates are compared with results obtained by solving the equations for a quasi-one-dimensional flame using the BVP4 Matlab solver. Comparison of the results showed that for high strain rates the results agree very closely, while for low strain rates they differ slightly. This can be explained by the influence of the border effects on the centerline results for a two-dimensional configuration. Additionally, the influence of different types of input boundary conditions is studied, concluding that a plug flow is the most adequate for comparison with the one-dimensional equations. Finally, a comparison of the maximum temperatures obtained for different strain rates showed discrepancies of up to 10% for high strain values. Later, a pseudo-one-dimensional flame configuration is used to study the convergence rates of the method in cases where combustion is present and again the expected convergence rates are obtained, only observing a slight deterioration for higher polynomial orders k . Finally, an unsteady test case with combustion is shown. It is observed that the temporal term of the continuity equation is a source of instability in cases with high temperature variations and causes the algorithm to not converge. Nevertheless, simulations ignoring the term are performed, which shows that the mesh refinement algorithm in a timestepping framework works as expected.

6 Conclusion

In the present work, the discretization and implementation of a fully coupled implicit method for simulating steady-state diffusion flames using the DG method are shown. The governing equations in the low-Mach limit are used, which allows to account for expansion and compression effects for large variations in temperature, and removes restriction to models such as the Boussinesq approximation. The chemical model used corresponds to a one-step model with variable parameters that captures fundamental characteristics of diffusion flames, while also demanding far less computational power compared to complex chemical models. Furthermore, temperature-dependent expressions for the transport parameters according to Sutherland's law and variable heat capacities according to NASA polynomials are used. The presented formulation of the equations allows the simulation of open and closed systems.

The discretization using DG-methods allows for a high-order formulation which offers high accuracy with low computational costs. A mixed-order formulation is used for stability reasons, where the velocity, temperature, and mass fractions are represented by polynomials of degree k , and pressure by polynomials of degree $k - 1$. The system obtained from the discretization is solved in a fully coupled manner by means of a Newton-Dogleg type method, which proved to be a very robust algorithm for the test cases presented, even for cases where an adequate initial estimate is not available. In addition, an efficient method for the calculation of the Jacobian matrix as part of Newton's algorithm is presented. Systems of linear equations are solved in two ways: Systems with up to approximately 500,000 DOF are solved using the direct solver PARDISO and larger systems are solved using a multi-grid method.

The algorithms presented here form a solid foundation for the solution using a fully coupled approach. The presented solver is used for the simulation of a wide range of test cases, which proves to be very efficient in the search for solutions and, most importantly, with little need of intervention from the user in terms of configuration.

The fully coupled method proved to be adequate and very time-efficient in finding solutions of all the test cases presented in this thesis. Tests were performed to compare the fully implicit approach presented in this work with the SIMPLE-DG algorithm-based solver that is already present in the BoSSS framework. A clear and very large difference in the runtimes is observed, where the XSEC solver presents computation times up to 20 times shorter than the SIMPLE-DG solver. It is important to note that this is not an indicator that the SIMPLE-DG method is generally less efficient in terms of computational time than the approach presented in this work, since the low performance of the SIMPLE-DG method could be explained by a poor choice of under-relaxation factors. However, the fully coupled approach presented in this work requires less user input, which also makes it more robust.

Additionally, as a convergence supporting strategy, an homotopy method is included in the structure of the nonlinear solver, which allows for solving highly nonlinear systems in a fully automatic manner. This type of algorithm is useful to solve steady state systems where some parameter makes the solution of the system difficult, as is, for example, the simulation of the square heated cavity problem for high Rayleigh numbers. The homotopy algorithm shown here is shown to be a robust and automatic strategy that allows finding solutions to such problems

without the need for user intervention.

For reactive test cases, the concept of the flame sheet estimate is demonstrated to be a useful and computationally inexpensive way to initialize steady-state calculation of combustion systems with finite reaction rate. Using this strategy avoids the need for ignition simulation, usually performed by means of timestepping or pseudo-timestepping techniques, which can be very time consuming.

6.1 Future work

Although the algorithms presented in this paper are useful for a large number of cases, there are aspects that still require further investigation. They are mentioned below.

Theoretically all the methods presented are capable of simulating three-dimensional flows. In the present work only two-dimensional systems are treated, due to performance reasons. The systems of equations to be solved in the three-dimensional case are too large for the linear-solvers that are part of the BoSSS-code. Nonetheless, the development of iterative solvers that allow the solution of such problems is ongoing work in the BoSSS developing group, and the simulation of systems with three-dimensional combustion could be part of future investigations.

The governing equations treated in this work are based on a set of assumptions. The diffusion model used is simplified, and it is expected that in certain combustion related problems, it may lead to large errors, particularly in systems that are not significantly diluted. Implementing a more complex diffusion model, such as the Hirschfelder and Curtiss approximation, would be a simple and efficient way to solve this problem. Another important point is that the simulations dealt mainly with very dilute fuels. Simulation of pure fuel combustion would in theory require much finer meshing (which greatly increases the number of DOF to be solved), or similarly, a more specialized refinement strategy. Future work could address these points, and the development of specialized linear solvers could help with computation times for systems with large numbers of DOF.

This work mainly dealt with steady-state combustion systems. The use of the flame sheet solution as an initial estimate proved to be an efficient way to find the burning solution. With this strategy, the need to simulate the flame initiation process is circumvented, since only the steady-state solution is of interest. Simulation of the ignition process is an open topic that should be addressed in future work.

Although the work showed that the fully coupled approach performed very well for a wide variety of problems, for more complex systems, such as non-stationary combustion processes, the computational times could be quite prohibitive.

Further computational parallelization, in particular of linear-solvers, could speed up the calculations.

In future work, the implemented solver is intended to be used in conjunction with a extended-DG solver (Kummer, 2017; Kummer et al., 2021; Krause and Kummer, 2017) in order to study multiphase reactive systems such as burning droplets. Some preliminary results have already been obtained and will be part of a future publication.

Bibliography

- Armaly, B. F., Durst, F., Pereira, J. C. F., and Schönung, B. (1983). "Experimental and Theoretical Investigation of Backward-Facing Step Flow." In: *Journal of Fluid Mechanics* 127.-1, p. 473. doi: 10.1017/S0022112083002839.
- Babuška, I. (1973). "The Finite Element Method with Lagrangian Multipliers." In: *Numerische Mathematik* 20.3, pp. 179–192. doi: 10.1007/BF01436561.
- Barkley, D., Gomes, G., and Henderson, R. (2000). "Three-Dimensional Instability in Flow over a Backward-Facing Step." In: *Journal of Fluid Mechanics* 473. doi: 10.1017/S002211200200232X.
- Bassi, F. and Rebay, S. (1997). "A High-Order Accurate Discontinuous Finite Element Method for the Numerical Solution of the Compressible Navier–Stokes Equations." In: *Journal of Computational Physics* 131.2, pp. 267–279. doi: 10.1006/jcph.1996.5572.
- Bird, R. B., Stewart, W. E., and Lightfoot, E. N. (1960). *Transport Phenomena*. New York: Wiley.
- Biswas, G., Breuer, M., and Durst, F. (2004). "Backward-Facing Step Flows for Various Expansion Ratios at Low and Moderate Reynolds Numbers." In: *Journal of Fluids Engineering* 126.3, pp. 362–374. doi: 10.1115/1.1760532.
- Botella, O. and Peyret, R. (1998). "Benchmark Spectral Results on the Lid-Driven Cavity Flow." In: *Computers & Fluids* 27, pp. 421–433. doi: 10.1016/S0045-7930(98)00002-4.
- Braack, M., Becker, R., Rannacher, R., and Warnatz, J. (1997). "An Adaptive Finite Element Method for Combustion Problems." In: *Proceedings of the Third Summer Conference, Numerical Modelling in Continuum Mechanics, Charles Universirt*.
- Bramble, J. H. and Hilbert, S. R. (1970). "Estimation of Linear Functionals on Sobolev Spaces with Application to Fourier Transforms and Spline Interpolation." In: *SIAM Journal on Numerical Analysis* 7.1, pp. 112–124. JSTOR: 2949585.
- Burke, S. P. and Schumann, T. E. W. (1928). "Diffusion Flames." In: *Industrial & Engineering Chemistry* 20.10, pp. 998–1004. doi: 10.1021/ie50226a005.
- Chandrasekhar, S. (1961). *Hydrodynamic and Hydromagnetic Stability*. Oxford: Oxford University Press.
- Chelliah, H. K., Law, C. K., Ueda, T., Smooke, M. D., and Williams, F. A. (1991). "An Experimental and Theoretical Investigation of the Dilution, Pressure and Flow-Field Effects on the Extinction Condition of Methane-Air-Nitrogen Diffusion Flames." In: *Symposium (International) on Combustion*. Twenty-Third Symposium (International) on Combustion 23.1, pp. 503–511. doi: 10.1016/S0082-0784(06)80297-3.
- Chorin, A. J. (1967). "The Numerical Solution of the Navier-Stokes Equations for an Incompressible Fluid." In: *Bulletin of the American Mathematical Society* 73.6, pp. 928–931. doi: 10.1090/S0002-9904-1967-11853-6.

- Cockburn, B., Karniadakis, G. E., and Shu, C.-W. (2000). “The Development of Discontinuous Galerkin Methods.” In: *Discontinuous Galerkin Methods*. Ed. by B. Cockburn, G. E. Karniadakis, and C.-W. Shu. Lecture Notes in Computational Science and Engineering. Berlin, Heidelberg: Springer, pp. 3–50. doi: 10.1007/978-3-642-59721-3_1.
- Colombo, A., Bortoli, A., Conti, P., Crivellini, A., Ghidoni, A., Nigro, A., and Noventa, G. (2021). “Assessment of a Discontinuous Galerkin Method for the Simulation of the Turbulent Flow around the DrivAer Car Model.” In: *Applied Sciences* 11.21, p. 10202. doi: 10.3390/app112110202.
- Cook, A. and Riley, J. (1996). “Direct Numerical Simulation of a Turbulent Reactive Plume on a Parallel Computer.” In: *Journal of Computational Physics* 129, pp. 263–283. doi: 10.1006/jcph.1996.0249.
- Dahlquist, G. G. (1963). “A Special Stability Problem for Linear Multistep Methods.” In: *BIT Numerical Mathematics* 3.1, pp. 27–43. doi: 10.1007/BF01963532.
- Deuflhard, P. (2011). *Newton Methods for Nonlinear Problems*. Springer Series in Computational Mathematics. Berlin, Heidelberg: Springer Berlin Heidelberg. doi: 10.1007/978-3-642-23899-4.
- Di Pietro, D. A. and Ern, A. (2012). *Mathematical Aspects of Discontinuous Galerkin Methods*. Mathématiques et Applications 69. Berlin New York: Springer.
- Dobbins, R. R. and Smooke, M. D. (2010). “A Fully Implicit, Compact Finite Difference Method for the Numerical Solution of Unsteady Laminar Flames.” In: *Flow, Turbulence and Combustion* 85.3-4, pp. 763–799. doi: 10.1007/s10494-010-9278-z.
- Fehn, N., Wall, W. A., and Kronbichler, M. (2019). “Modern Discontinuous Galerkin Methods for the Simulation of Transitional and Turbulent Flows in Biomedical Engineering: A Comprehensive LES Study of the FDA Benchmark Nozzle Model.” In: *International Journal for Numerical Methods in Biomedical Engineering* 35.12, e3228. doi: 10.1002/cnm.3228.
- Fernandez-Tarrazo, E., Sanchez, A., Linan, A., and Williams, F. (2006). “A Simple One-Step Chemistry Model for Partially Premixed Hydrocarbon Combustion.” In: *Combustion and Flame* 147.1-2, pp. 32–38. doi: 10.1016/j.combustflame.2006.08.001.
- Ferziger, J. H. and Perić, M. (2002). *Computational Methods for Fluid Dynamics*. Berlin, Heidelberg: Springer Berlin Heidelberg. doi: 10.1007/978-3-642-56026-2.
- Fiala, T. and Sattelmayer, T. (2014). “Nonpremixed Counterflow Flames: Scaling Rules for Batch Simulations.” In: *Journal of Combustion* 2014. Ed. by C. D. Rakopoulos, p. 484372. doi: 10.1155/2014/484372.
- Frouzakis, C. E., Lee, J., Tomboulides, A. G., and Boulouchos, K. (1998). “Two-Dimensional Direct Numerical Simulation of Opposed-Jet Hydrogen-Air Diffusion Flame.” In: *Symposium (International) on Combustion*. Twenty-Seventh Sysposium (International) on Combustion Volume One 27.1, pp. 571–577. doi: 10.1016/S0082-0784(98)80448-7.
- Gassner, G., Lörcher, F., and Munz, C.-D. (2007). “A Contribution to the Construction of Diffusion Fluxes for Finite Volume and Discontinuous Galerkin Schemes.” In: *Journal of Computational Physics* 224.2, pp. 1049–1063. doi: 10.1016/j.jcp.2006.11.004.
- Geisenhofer, M., Kummer, F., and Müller, B. (2019). “A Discontinuous Galerkin Immersed Boundary Solver for Compressible Flows: Adaptive Local Time Stepping for Artificial Viscos-

- ity-Based Shock-Capturing on Cut Cells.” In: *International Journal for Numerical Methods in Fluids* 91.9, pp. 448–472. doi: 10.1002/fld.4761.
- Girault, V., Rivière, B., and Wheeler, M. F. (2004). “A Discontinuous Galerkin Method with Nonoverlapping Domain Decomposition for the Stokes and Navier-Stokes Problems.” In: *Mathematics of Computation* 74.249, pp. 53–85. doi: 10.1090/S0025-5718-04-01652-7.
- Goey, P., Somers, L., BOSCH, W., and Mallens, R. (1995). “Modeling of the Small Scale Structure of Flat Burner-Stabilized Flames.” In: *Combustion Science and Technology - COMBUST SCI TECHNOL* 104, pp. 387–400. doi: 10.1080/00102209508907729.
- Gutiérrez-Jorquera, J. and Kummer, F. (2022a). “A Fully Coupled High-Order Discontinuous Galerkin Method for Diffusion Flames in a Low-Mach Number Framework.” In: *International Journal for Numerical Methods in Fluids* 94.4, pp. 316–345. doi: 10.1002/fld.5056.
- Gutiérrez-Jorquera, J. and Kummer, F. (2022b). “A Fully Coupled High-order Discontinuous Galerkin Method for Diffusion Flames in a low-Mach Number Framework.” In: *International Journal for Numerical Methods in Fluids* 94.4, pp. 316–345. doi: 10.1002/fld.5056.
- Haroutunian, V., Engelman, M. S., and Hasbani, I. (1993). “Segregated Finite Element Algorithms for the Numerical Solution of Large-Scale Incompressible Flow Problems.” In: *International Journal for Numerical Methods in Fluids* 17.4, pp. 323–348. doi: 10.1002/fld.1650170405.
- Hennink, A. (2022). “Low-Mach Number Flow and the Discontinuous Galerkin Method.” In: doi: 10.4233/uuid:9b35b35a-0789-4883-a471-f8df0d7939ad.
- Hennink, A., Tiberga, M., and Lathouwers, D. (2021). “A Pressure-Based Solver for Low-Mach Number Flow Using a Discontinuous Galerkin Method.” In: *Journal of Computational Physics* 425, p. 109877. doi: 10.1016/j.jcp.2020.109877.
- Hesthaven, J. S. and Warburton, T. (2008). *Nodal Discontinuous Galerkin Methods: Algorithms, Analysis, and Applications*. Texts in Applied Mathematics 54. New York: Springer.
- Hillewaert, K. (2013). *Development of the Discontinuous Galerkin Method for High-resolution, Large Scale CFD and Acoustics in Industrial Geometries*. Presses univ. de Louvain.
- Johnson, R. F., VanDine, A. C., Esposito, G. L., and Chelliah, H. K. (2015). “On the Axisymmetric Counterflow Flame Simulations: Is There an Optimal Nozzle Diameter and Separation Distance to Apply Quasi One-Dimensional Theory?” In: *Combustion Science and Technology* 187.1-2, pp. 37–59. doi: 10.1080/00102202.2014.972503.
- Johnson, R. F. and Kercher, A. D. (2020). “A Conservative Discontinuous Galerkin Discretization for the Chemically Reacting Navier-Stokes Equations.” In: *Journal of Computational Physics* 423, p. 109826. doi: 10.1016/j.jcp.2020.109826.
- Kao, P.-H. and Yang, R.-J. (2007). “Simulating Oscillatory Flows in Rayleigh–Bénard Convection Using the Lattice Boltzmann Method.” In: *International Journal of Heat and Mass Transfer* 50.17-18, pp. 3315–3328. doi: 10.1016/j.ijheatmasstransfer.2007.01.035.
- Karaa, S., Zhang, J., and Douglas, C. C. (2003). “Preconditioned Multigrid Simulation of an Axisymmetric Laminar Diffusion Flame.” In: *Mathematical and Computer Modelling* 38.3, pp. 269–279. doi: 10.1016/S0895-7177(03)90086-0.

- Kee, R. J., Coltrin, M. E., and Glarborg, P. (2003). *Chemically Reacting Flow: Theory and Practice*. Hoboken, N.J: Wiley-Interscience.
- Kelley, C. T. (1995). *Iterative Methods for Linear and Nonlinear Equations*. Frontiers in Applied Mathematics 16. Philadelphia: Society for Industrial and Applied Mathematics.
- Keshtiban, I., Belblidia, F., and Webster, M. (2003). “Compressible Flow Solvers for Low Mach Number Flows—a Review.” In: 23.
- Keyes, D. and Smooke, M. (1987). “Flame Sheet Starting Estimates for Counterflow Diffusion Flame Problems.” In: *Journal of Computational Physics* 73.2, pp. 267–288. doi: [10.1016/0021-9991\(87\)90137-9](https://doi.org/10.1016/0021-9991(87)90137-9).
- Kierzenka, J. and Shampine, L. F. (2001). “A BVP Solver Based on Residual Control and the Maltab PSE.” In: *ACM Transactions on Mathematical Software* 27.3, pp. 299–316. doi: [10.1145/502800.502801](https://doi.org/10.1145/502800.502801).
- Kikker, A. (2020). “A High-Order (EXtended) Discontinuous Galerkin Solver for the Simulation of Viscoelastic Droplet.” PhD thesis. Darmstadt: Technische Universität. doi: [10.25534/tuprints-00012308](https://doi.org/10.25534/tuprints-00012308).
- Kikker, A., Kummer, F., and Oberlack, M. (2020). “A Fully Coupled High-Order Discontinuous Galerkin Solver for Viscoelastic Fluid Flow.” In: *International Journal for Numerical Methods in Fluids* (). doi: [10.1002/fld.4950](https://doi.org/10.1002/fld.4950).
- Klein, B., Kummer, F., Keil, M., and Oberlack, M. (2015). “An Extension of the SIMPLE Based Discontinuous Galerkin Solver to Unsteady Incompressible Flows.” In: *International Journal for Numerical Methods in Fluids* 77.10, pp. 571–589. doi: [10.1002/fld.3994](https://doi.org/10.1002/fld.3994).
- Klein, B., Müller, B., Kummer, F., and Oberlack, M. (2016). “A High-Order Discontinuous Galerkin Solver for Low Mach Number Flows.” In: *International Journal for Numerical Methods in Fluids* 81.8, pp. 489–520. doi: [10.1002/fld.4193](https://doi.org/10.1002/fld.4193).
- Klein, B. (2015). “A high-order Discontinuous Galerkin solver for incompressible and low-Mach number flows.” PhD thesis. Darmstadt: Technische Universität.
- Klein, B., Kummer, F., and Oberlack, M. (2013). “A SIMPLE Based Discontinuous Galerkin Solver for Steady Incompressible Flows.” In: *Journal of Computational Physics* 237, pp. 235–250. doi: [10.1016/j.jcp.2012.11.051](https://doi.org/10.1016/j.jcp.2012.11.051).
- Klingenberg, D. (2022). “Development of Novel Reynolds-averaged Navier-Stokes Turbulence Models Based on Lie Symmetry Constraints.” In: doi: [10.26083/TUPRINTS-00022400](https://doi.org/10.26083/TUPRINTS-00022400).
- Knikker, R. (2011). “A Comparative Study of High-Order Variable-Property Segregated Algorithms for Unsteady Low Mach Number Flows.” In: *International Journal for Numerical Methods in Fluids* 66.4, pp. 403–427. doi: [10.1002/fld.2261](https://doi.org/10.1002/fld.2261).
- Krause, D. and Kummer, F. (2017). “An Incompressible Immersed Boundary Solver for Moving Body Flows Using a Cut Cell Discontinuous Galerkin Method.” In: *Computers & Fluids* 153. doi: [10.1016/j.compfluid.2017.05.008](https://doi.org/10.1016/j.compfluid.2017.05.008).
- Kummer, F., Müller, B., Geisenhofer, M., Kahle, J., Krause, D., Smuda, M., Utz, T., Krämer-Eis, S., Dierkes, D., Kikker, A., and Keil, M. (2020). *BoSSS-Handbook.Pdf*.
- Kummer, F. (2012). “The BoSSS Discontinuous Galerkin Solver for Incompressible Fluid Dynamics and an Extension to Singular Equations.” PhD thesis. Darmstadt: Technische Universität.

- Kummer, F. (2017). “Extended Discontinuous Galerkin Methods for Two-Phase Flows: The Spatial Discretization.” In: *International Journal for Numerical Methods in Engineering* 109.2, pp. 259–289. doi: [10.1002/nme.5288](https://doi.org/10.1002/nme.5288).
- Kummer, F., Müller, B., and Utz, T. (2018). “Time Integration for Extended Discontinuous Galerkin Methods with Moving Domains.” In: *International Journal for Numerical Methods in Engineering* 113.5, pp. 767–788. doi: [10.1002/nme.5634](https://doi.org/10.1002/nme.5634).
- Kummer, F., Weber, J., and Smuda, M. (2021). “BoSSS: A Package for Multigrid Extended Discontinuous Galerkin Methods.” In: *Computers & Mathematics with Applications*. Development and Application of Open-source Software for Problems with Numerical PDEs 81, pp. 237–257. doi: [10.1016/j.camwa.2020.05.001](https://doi.org/10.1016/j.camwa.2020.05.001).
- Lee, J., Frouzakis, C. E., and Boulochous, K. (2000). “Two-Dimensional Direct Numerical Simulation of Opposed-Jet Hydrogen/Air Flames: Transition from a Diffusion to an Edge Flame.” In: *Proceedings of the Combustion Institute* 28.1, pp. 801–806. doi: [10.1016/S0082-0784\(00\)80283-0](https://doi.org/10.1016/S0082-0784(00)80283-0).
- LeVeque, R. J. (2002). *Finite Volume Methods for Hyperbolic Problems*. Cambridge Texts in Applied Mathematics. Cambridge ; New York: Cambridge University Press.
- Liñán, A., Orlandi, P., Verzicco, R., and Higuera, F. J. (1994). “Effects of Non-Unity Lewis Numbers in Diffusion Flames.” In.
- Lv, Y. and Ihme, M. (2017). “High-Order Discontinuous Galerkin Method for Applications to Multicomponent and Chemically Reacting Flows.” In: *Acta Mechanica Sinica* 33, pp. 1–14. doi: [10.1007/s10409-017-0664-9](https://doi.org/10.1007/s10409-017-0664-9).
- Majda, A. and Sethian, J. (1985). “The Derivation and Numerical Solution of the Equations for Zero Mach Number Combustion.” In: *Combustion Science and Technology* 42.3-4, pp. 185–205. doi: [10.1080/00102208508960376](https://doi.org/10.1080/00102208508960376).
- Matalon, M., Ludford, G. S. S., and Buckmaster, J. (1980). “Diffusion Flames in a Chamber.” In: *Gasdynamics of Explosions and Reactive Systems*. Ed. by A. K. Oppenheim. Pergamon, pp. 943–959.
- Matalon, M. and Metzner, P. (2010). “The Effect of Thermal Expansion on Diffusion Flame Instabilities.” In: *Journal of Fluid Mechanics* 647, pp. 453–472. doi: [10.1017/S0022112009993016](https://doi.org/10.1017/S0022112009993016).
- Mavriplis, D., Nastase, C., Shahbazi, K., Wang, L., and Burgess, N. (2009). “Progress in High-Order Discontinuous Galerkin Methods for Aerospace Applications.” In: *47th AIAA Aerospace Sciences Meeting including the New Horizons Forum and Aerospace Exposition*. doi: [10.2514/6.2009-601](https://doi.org/10.2514/6.2009-601).
- McBride, B., Gordon, S., and Reno, M. (1993). *NASA Thermodynamic Data Base*. NASA Technical Memorandum 4513.
- Miao, C. (2022). “High-Order Simulation of Low-Mach-Flows.” MA thesis. Technische Universität Darmstadt.
- Müller, B. (1998). “Low-Mach-Number Asymptotics of the Navier-Stokes Equations.” In: *Journal of Engineering Mathematics* 34.1, pp. 97–109. doi: [10.1023/A:1004349817404](https://doi.org/10.1023/A:1004349817404).
- Nicoud, F. (2000). “Conservative High-Order Finite-Difference Schemes for Low-Mach Number Flows.” In: *Journal of Computational Physics* 158.1, pp. 71–97. doi: [10.1006/jcph.1999.6408](https://doi.org/10.1006/jcph.1999.6408).

- Nishioka, M., Law, C. K., and Takeno, T. (1996). “A Flame-Controlling Continuation Method for Generating S-curve Responses with Detailed Chemistry.” In: *Combustion and Flame* 104.3, pp. 328–342. doi: [10.1016/0010-2180\(95\)00132-8](https://doi.org/10.1016/0010-2180(95)00132-8).
- Nonaka, A., Day, M. S., and Bell, J. B. (2018). “A Conservative, Thermodynamically Consistent Numerical Approach for Low Mach Number Combustion. Part I: Single-level Integration.” In: *Combustion Theory and Modelling* 22.1, pp. 156–184. doi: [10.1080/13647830.2017.1390610](https://doi.org/10.1080/13647830.2017.1390610).
- Pailiere, H., Viozat, C., Kumbaro, A., and Toumi, I. (2000). “Comparison of Low Mach Number Models for Natural Convection Problems.” In: *Heat and Mass Transfer* 36.6, pp. 567–573. doi: [10.1007/s002310000116](https://doi.org/10.1007/s002310000116).
- Pandya, T. P. and Weinberg, F. J. (1964). “The Structure of Flat, Counter-Flow Diffusion Flames.” In: *Proceedings of the Royal Society of London. Series A, Mathematical and Physical Sciences* 279.1379, pp. 544–561. JSTOR: 2414698.
- Patankar, S. V. (1980). *Numerical Heat Transfer and Fluid Flow*. Series in Computational Methods in Mechanics and Thermal Sciences. New York: Hemisphere Publ. Co.
- Pawlowski, R. P., Shadid, J. N., Simonis, J. P., and Walker, H. F. (2006). “Globalization Techniques for Newton–Krylov Methods and Applications to the Fully Coupled Solution of the Navier–Stokes Equations.” In: *SIAM Review* 48.4, pp. 700–721. doi: [10.1137/S0036144504443511](https://doi.org/10.1137/S0036144504443511).
- Pawlowski, R. P., Simonis, J. P., Walker, H. F., and Shadid, J. N. (2008). “Inexact Newton Dogleg Methods.” In: *SIAM Journal on Numerical Analysis* 46.4, pp. 2112–2132. JSTOR: 40233295.
- Paxion, S., Baron, R., Gordner, A., Neuss, N., Bastian, P., Thévenin, D., and Wittum, G. (2001). “Development of a Parallel Unstructured Multigrid Solver for Laminar Flame Simulations with Detailed Chemistry and Transport.” In: *Numerical Flow Simulation II*. Ed. by E. H. Hirschel. Notes on Numerical Fluid Mechanics (NNFM). Berlin, Heidelberg: Springer, pp. 181–198. doi: [10.1007/978-3-540-44567-8_11](https://doi.org/10.1007/978-3-540-44567-8_11).
- Peters, N. (1985). “Numerical and Asymptotic Analysis of Systematically Reduced Reaction Schemes for Hydrocarbon Flames.” In: *Numerical Simulation of Combustion Phenomena*. Ed. by R. Glowinski, B. Larroutrou, and R. Temam. Lecture Notes in Physics. Berlin, Heidelberg: Springer, pp. 90–109. doi: [10.1007/BFb0008654](https://doi.org/10.1007/BFb0008654).
- Peters, N. and Williams, F. A. (1987). “The Asymptotic Structure of Stoichiometric Methane-Air Flames.” In: *Combustion and Flame* 68.2, pp. 185–207. doi: [10.1016/0010-2180\(87\)90057-5](https://doi.org/10.1016/0010-2180(87)90057-5).
- Pietro, D. A. D. and Ern, A. (2012). *Mathematical Aspects of Discontinuous Galerkin Methods*. Mathématiques et Applications. Berlin Heidelberg: Springer-Verlag.
- Poinson, T. and Veynante, D. (2011). *Theoretical and Numerical Combustion*. 3. ed. Toulouse: CNRS.
- Rameau, J. F. and Schmidt-Lainé, C. (1985). “Numerical Bifurcation in Chambered Diffusion Flames.” In: *Numerical Simulation of Combustion Phenomena*. Lecture Notes in Physics. Berlin, Heidelberg: Springer, pp. 335–349. doi: [10.1007/BFb0008671](https://doi.org/10.1007/BFb0008671).
- Rauwoens, P., Vierendeels, J., Dick, E., and Merci, B. (2009). “A Conservative Discrete Compatibility-Constraint Low-Mach Pressure-Correction Algorithm for Time-Accurate Simulations of Vari-

- able Density Flows.” In: *Journal of Computational Physics* 228.13, pp. 4714–4744. doi: 10.1016/j.jcp.2009.03.036.
- Rehm, R. and Baum, H. (1978). “The Equations of Motion for Thermally Driven, Buoyant Flows.” In: *Journal of Research of the National Bureau of Standards* 83.3, p. 297. doi: 10.6028/jres.083.019.
- Schenk, O., Gärtner, K., and Fichtner, W. (2000). “Efficient Sparse LU Factorization with Left-Right Looking Strategy on Shared Memory Multiprocessors.” In: *BIT Numerical Mathematics* 40.1, pp. 158–176. doi: 10.1023/A:1022326604210.
- Schenk, O. and Gärtner, K. (2002). “Two-Level Dynamic Scheduling in PARDISO: Improved Scalability on Shared Memory Multiprocessing Systems.” In: *Parallel Computing* 28.2, pp. 187–197. doi: 10.1016/S0167-8191(01)00135-1.
- Schenk, O. and Gärtner, K. (2004). “Solving Unsymmetric Sparse Systems of Linear Equations with PARDISO.” In: *Future Generation Computer Systems. Selected Numerical Algorithms* 20.3, pp. 475–487. doi: 10.1016/j.future.2003.07.011.
- Shahbazi, K. (2005). “An Explicit Expression for the Penalty Parameter of the Interior Penalty Method.” In: *Journal of Computational Physics* 205.2, pp. 401–407. doi: 10.1016/j.jcp.2004.11.017.
- Shahbazi, K., Fischer, P. F., and Ethier, C. R. (2007). “A High-Order Discontinuous Galerkin Method for the Unsteady Incompressible Navier–Stokes Equations.” In: *Journal of Computational Physics* 222.1, pp. 391–407. doi: 10.1016/j.jcp.2006.07.029.
- Sharma, A. and Eswaran, V. (2004). “HEAT AND FLUID FLOW ACROSS A SQUARE CYLINDER IN THE TWO-DIMENSIONAL LAMINAR FLOW REGIME.” In: *Numerical Heat Transfer, Part A: Applications* 45.3, pp. 247–269. doi: 10.1080/10407780490278562.
- Shen, W., Zhang, J., and Yang, F. (2006). “Newton’s Method for Steady and Unsteady Reacting Flows.” In: *ACM-SE* 44. doi: 10.1145/1185448.1185621.
- Shi, J.-M., Gerlach, D., Breuer, M., Biswas, G., and Durst, F. (2004). “Heating Effect on Steady and Unsteady Horizontal Laminar Flow of Air Past a Circular Cylinder.” In: *Physics of Fluids* 16.12, pp. 4331–4345. doi: 10.1063/1.1804547.
- Shishkina, O. (2021). “Rayleigh-Bénard Convection: The Container Shape Matters.” In: *Physical Review Fluids* 6.9, p. 090502. doi: 10.1103/PhysRevFluids.6.090502.
- Smooke, M. D. and Giovangigli, V. (1991). “Formulation of the Premixed and Nonpremixed Test Problems.” In: *Reduced Kinetic Mechanisms and Asymptotic Approximations for Methane-Air Flames: A Topical Volume*. Ed. by M. D. Smooke. Lecture Notes in Physics. Berlin, Heidelberg: Springer, pp. 1–28. doi: 10.1007/BFb0035363.
- Smooke, M. D. and Giovangigli, V. (1992). “Numerical Modeling of Axisymmetric Laminar Diffusion Flames.” In: *IMPACT of Computing in Science and Engineering* 4.1, pp. 46–79. doi: 10.1016/0899-8248(92)90016-2.
- Smooke, M. D., Mitchell, R. E., and Keyes, D. E. (1986a). “Numerical Solution of Two-Dimensional Axisymmetric Laminar Diffusion Flames.” In: *Combustion Science and Technology* 67.4-6, pp. 85–122. doi: 10.1080/00102208908924063.

- Smooke, M. D., Mitchell, R. E., and Keyes, D. E. (1986b). "Numerical Solution of Two-Dimensional Axisymmetric Laminar Diffusion Flames." In: *Combustion Science and Technology* 67.4-6, pp. 85–122. doi: 10.1080/00102208908924063.
- Smooke, M. D. and Giovangigli, V. (1991). "Premixed and Nonpremixed Test Problem Results." In: *Reduced Kinetic Mechanisms and Asymptotic Approximations for Methane-Air Flames*. Ed. by M. D. Smooke. Vol. 384. Berlin/Heidelberg: Springer-Verlag, pp. 29–47. doi: 10.1007/BFb0035364.
- Smuda, M. (2021). "Direct Numerical Simulation of Multi-Phase Flows Using Extended Discontinuous Galerkin Methods." In: doi: 10.26083/TUPRINTS-00017376.
- Spalding, D. B. (1961). "Theory of Mixing and Chemical Reaction in the Opposed-Jet Diffusion Flame." In: doi: 10.2514/8.5626.
- Stauch, R., Lipp, S., and Maas, U. (2006). "Detailed Numerical Simulation of the Auto-Ignition of Liquid Fuel Droplets." In: *Advances in High Performance Computing and Computational Sciences*. Ed. by Y. Shokin, M. Resch, N. Shokina, N. Danaev, and M. Orunkhanov. Berlin, Heidelberg: Springer, pp. 127–137. doi: 10.1007/978-3-540-33844-4_11.
- Sutherland, W. (1893). "LII. The Viscosity of Gases and Molecular Force." In: *The London, Edinburgh, and Dublin Philosophical Magazine and Journal of Science* 36.223, pp. 507–531. doi: 10.1080/14786449308620508.
- Tyliszczak, A. (2014). "Projection Method for High-Order Compact Schemes for Low Mach Number Flows in Enclosures." In: *International Journal of Numerical Methods for Heat & Fluid Flow* 24.5, pp. 1141–1174. doi: 10.1108/HFF-07-2012-0167.
- Vierendeels, J., Merci, B., and Dick, E. (2003). "Benchmark Solutions for the Natural Convective Heat Transfer Problem in a Square Cavity with Large Horizontal Temperature Differences." In: *International Journal of Numerical Methods for Heat & Fluid Flow* 13.8, pp. 1057–1078. doi: 10.1108/09615530310501957.
- Wang, A.-B., Trávníček, Z., and Chia, K.-C. (2000). "On the Relationship of Effective Reynolds Number and Strouhal Number for the Laminar Vortex Shedding of a Heated Circular Cylinder." In: *Physics of Fluids* 12.6, pp. 1401–1410. doi: 10.1063/1.870391.
- Westbrook, C. K. and Dryer, F. L. (1981). "Simplified Reaction Mechanisms for the Oxidation of Hydrocarbon Fuels in Flames." In: *Combustion Science and Technology* 27.1-2, pp. 31–43. doi: 10.1080/00102208108946970.
- Williams, F. A. (2000). *Combustion Theory: The Fundamental Theory of Chemically Reacting Flow Systems*. 2. ed., [Nachdr.] Combustion Science and Engineering Series. Cambridge, Mass: Perseus Books.
- Xie, W. and Xi, G. (2016). "Fluid Flow and Heat Transfer Characteristics of Separation and Reattachment Flow over a Backward-Facing Step." In: *International Journal of Refrigeration* 74. doi: 10.1016/j.ijrefrig.2016.10.006.
- Xu, Y. and Smooke, M. D. (1993). "Application of a Primitive Variable Newton's Method for the Calculation of an Axisymmetric Laminar Diffusion Flame." In: *Journal of Computational Physics* 104.1, pp. 99–109. doi: 10.1006/jcph.1993.1012.